PRODUCTION AND USE OF RADIOACTIVE ION BEAMS FOR MEASUREMENTS OF NUCLEAR REACTIONS

Wenzhong Liu

Doctor of Philosophy
The University of Michigan - 1990

PRODUCTION AND USE OF RADIOACTIVE ION BEAMS FOR MEASUREMENTS OF NUCLEAR REACTIONS

by

Wenzhong Liu

A dissertation submitted in partial fulfillment
of the requirements for the degree of
Doctor of Philosophy
(Physics)
in The University of Michigan
1990

Doctoral Committee:

Professor Frederick Becchetti, Chairman
Professor Michael Bretz
Professor Joseph Ullman
Professor John Ward
Professor Edward Yao

ACKNOWLEDGEMENTS

I would like to thank:

Fred Becchetti, my thesis advisor, for his guidance and tolerance throughout the past four years;

Joachim Jänecke, Don Roberts, Jim Kolata, Abdel Mosad, Xiangjing Kong, and Bob Warner, my collaborators, for their invaluable help in all phases of the project;

Bob Kryger, Rich Tighe, Sunil Dixit, Ed Berners, Robin Stern, Dave Hotz, Wanhui Zheng, Mike Dueweke, Karim Ashktorab, and Jim Brown, for their assistance in the experimental runs;

Alain Young, for her aid with program LISA.

I would also like to thank the National Science Foundation (Grant PHY8605907) and the University of Michigan for financial support.

TABLE OF CONTENTS

LIST OF TABLES

Table

LIST OF FIGURES

Figure

LIST OF APPENDICES

Appendix

CHAPTER 1

INTRODUCTION

1.1 Objectives of Studies with Radioactive Nuclei

A nucleus is called radioactive if it spontaneously decays by the emission of an alpha particle, a nucleon, a beta particle, or a gamma quantum. In the past decade, it has become clear that there are pressing needs for data on the properties of radioactive nuclei in both basic and applied research (Fowler, 1985) and that experiments with Radioactive Ion Beams (RIBs) are important.

A. RIBs in Basic Nuclear Research

In basic nuclear physics, studies of nuclear reactions have been mostly limited to the few hundreds of stable isotopes because stable ion beams or targets are more readily available. On the other hand, there are more than one thousand unstable isotopes whose nuclear properties have not yet been measured. Extrapolations of reaction rates for radioactive nuclei from rates observed with stable nuclei, as Becchetti (Becchetti, 1989) has pointed out, may well be in error because of very positive Q-values (difference between the initial and final masses) of reactions involving radioactive nuclei and low binding energies, high ground-state spins and isospins, and large deformations of radioactive nuclei. Indeed, reaction rates involving radioactive nuclei computed by nuclear models sometimes have uncertainties of a few orders of magnitude (Arnold, 1988a). A better understanding of the nuclear

nuclei will depend on *direct* measurements with radioactive ion beams or radioactive targets. Tanihata (Tanihata, 1988) has observed that the very neutron-rich nucleus ^{11}Li has very large rms radius, small momentum fluctuations of fragmentation products and small binding energy of the last two neutrons. This is just an example of the anomalous behavior of radioactive isotopes.

B. The Missing Mass Problem

Far from being just a valuable tool for nuclear structure studies, RIBs have many applications in other areas. An important application of low energy RIBs is to the study of contemporary nuclear astrophysical problems, since radioactive nuclei are involved in nuclear reactions occurring in a large variety of astrophysical environments.

One of the outstanding problems in astrophysics is the missing mass problem, which concerns the amount of baryons in our universe. The baryon density is used in determining the ratio of the mass density, ρ, of the universe to the critical mass density, ρ_c:

$$\rho_c = (3Ho^2/8\pi G) \simeq 5 \times 10^{-30} g\ cm^{-1},$$

where $Ho = v/d = 50 kms^{-1} Mpc^{-1}$ is the Hubble's constant, and G is the Newton's constant of gravity (Rolfs, 1988). The universe is closed if $\rho/\rho_c > 1$, and it is open if $\rho/\rho_c < 1$.

The standard big bang model (Wagoner, 1967; Schramm, 1977) assumes that the density of the universe is uniform during the period of nucleosynthesis, which occurs at around $10^9\ K$ and at times between $10^{-3}\ s$ and few minutes after the big bang. In this model, only four isotopes, ^{2}H, ^{3}He, ^{4}He and ^{7}Li can be synthesized in amounts comparable with their observed abundances. The probability of producing isotopes of $A > 7$ is very small. Reactions involving ^{2}H like ^{8}Li (^{2}H, n) ^{9}Be are not

important, primarily because of the small abundance of ^{2}H (Boyd, 1988). Fig. 1.1 (Rolfs, 1988) shows the mass fraction of light elements produced in the standard big bang model as a function of the present baryon density, ρ_B. Based on the curves in this figure, the baryon density is determined if the abundance of certain isotope, say ^{7}Li, is experimentally measured (Spite, 1982). A concordant value for ρ_B has been found $\rho_B \simeq 5 \times 10^{-31} g cm^{-3}$ (Rolfs, 1988). If this baryon density represents the total density of matter in the universe, we have $\rho/\rho_c = 0.10$ and the universe is open and will continue to expand forever. So it seems that a large amount of baryons needed to close the universe is missing.

Since there are strong arguments that $\rho/\rho_c = 1$ (Austin, 1989), some physicists are investigating the possibility that a nonstandard big bang model will allow $\rho/\rho_c = 1$ and still yield nucleosynthesis results consistent with observations.

In the nonstandard big bang model, it is assumed that the universe at the time of nucleosynthesis consists of high density proton-rich regions coupled with low density neutron-rich regions as a consequence of a quark/gluon-to-hadron phase transition (Witten, 1984; Applegate, 1985). In such an inhomogeneous universe, ^{2}H can be produced in large amounts (Austin, 1989) and heavy elements ($A > 7$) can be synthesized (Applegate, 1988) in the neutron-rich regions. Thus this model may yield a $\rho/\rho_c = 1$ universe without non-baryonic black matter. Malaney and Fowler (Malaney, 1988) have identified the main reaction chain by which isotopes of $A > 12$ can be produced in this model:

$$^1\mathrm{H}(n,\gamma)^2\mathrm{H}(n,\gamma)^3\mathrm{H}(d,n)^4\mathrm{He}(t,\gamma)^7\mathrm{Li}(n,\gamma)^8\mathrm{Li}$$

$$^8\mathrm{Li}(\alpha,n)^{11}\mathrm{B}(n,\gamma)^{12}\mathrm{B}(\beta)^{12}\mathrm{C}(n,\gamma)^{13}\mathrm{C}(n,\gamma)^{14}\mathrm{C}.$$

The critical point in this chain is at ^{8}Li. The reaction ^{8}Li(^{4}He, n)^{11}B must proceed rapidly enough for the heavy element in the chain to be effectively synthesized, since

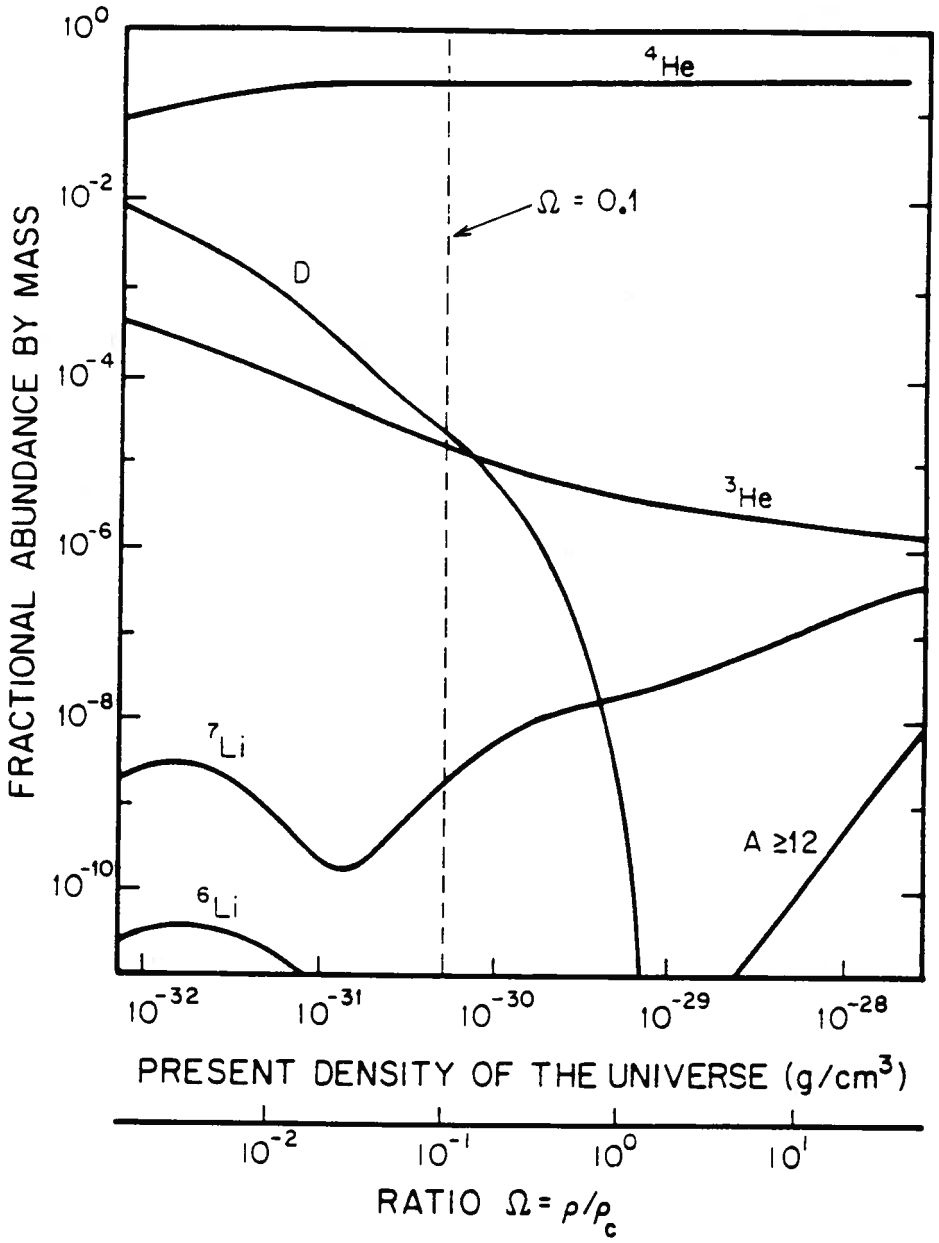

Fig. 1.1 Mass fraction of the light elements synthesized in the standard big bang model as a function of the present baryon density of the universe, or, equivalently, as a function of the present density in terms of the critical density ρ_c (Rolfs, 1988).

^{8}Li can also take part in other reactions. Some competing processes involving ^{8}Li are:

$$^8\mathrm{Li}(n,\gamma)^9\mathrm{Li}(\beta)^9\mathrm{Be}(\gamma,n)^8\mathrm{Be}(^4\mathrm{He})^4\mathrm{He}$$

$$^8\mathrm{Li}(d,n)^9\mathrm{Be}(\gamma,n)^8\mathrm{Be}(^4\mathrm{He})^4\mathrm{He}$$

$$^8\mathrm{Li}(\mathrm{H},\gamma)^9\mathrm{Be}(\gamma,n)^8\mathrm{Be}(^4\mathrm{He})^4\mathrm{He}$$

$$^8\mathrm{Li}(\mathrm{H},^2\mathrm{H})^7\mathrm{Li},^8\mathrm{Li}(\mathrm{H},^3\mathrm{H})^6\mathrm{Li}$$

$$^8\mathrm{Li}(^2\mathrm{H},^3\mathrm{H})^7\mathrm{Li}.$$

^{8}Li has a half-life of 838 ms as it β-decays: $^8\mathrm{Li}(\beta)^8\mathrm{Be}(^4\mathrm{He})^4\mathrm{He}$. All these competing reactions can deplete the ^{8}Li abundance. Therefore, experimental data on ^{8}Li reaction rates are needed to predict the amount of heavy element synthesized in the nonstandard big bang model.

C. The $p-p$ Chain and the Solar Neutrino Problem

Also related to research with RIBs are the $p-p$ chain and the missing solar neutrino problem.

The p–p chain is a sequence of nuclear reactions in which four hydrogen nuclei are converted into a ^{4}He nucleus, accompanied by two positrons, two electron neutrinos and a large amount of energy (26.73 MeV). Hydrogen is the most abundant element in the sun (Rolfs, 1988) and this chain is the mechanism which operates in the solar interior (Fowler, 1989) at the temperature of 2×10^7 K (Mathews, 1984). It is mainly responsible for the generation of solar energy. The $p-p$ chain proceeds as follows:

$$p(p,e^+\nu)d(p,\gamma)^3\mathrm{He}(^4\mathrm{He},\gamma)^7\mathrm{Be}$$

$$^7\mathrm{Be}(p,\gamma)^8\mathrm{B}(e^+\nu)^8\mathrm{Be}(^4\mathrm{He})^4\mathrm{He}$$

^{7}Be is radioactive with a half-life 53.29d and its nuclear reaction properties are poorly known. Direct measurement of the $^7\mathrm{Be}(p,\gamma)$ ^{8}B reaction rate is thus required for the calculation of energy production via this chain. Included in the p–p chain are

two different reactions that produce electron neutrinos. The energy of the neutrino from the reaction $p(p, e^+\nu)d$ is no more than 1 MeV. But the neutrino from the reactions,

$$^7\mathrm{Be}(p,\gamma)^8\mathrm{B}(e^+\nu)^8\mathrm{Be}$$

can have energy up to 17 MeV, and should be energetic enough to be detectable through interaction with the nuclei ^{37}Cl to form ^{37}Ar (Fowler, 1984). (These neutrinos from the sun are the only direct indicator we have of the hydrogen burning.) But the observed number of neutrinos appears to be only one-third of the number expected (Mathews, 1984). Since the neutrino production reaction ^{8}B $(e^+\nu)^4$Be follows $^7\mathrm{Be}(p,\gamma)^8\mathrm{B}$, a direct measurement of the reaction rate of the latter will determine the ^{8}B formation rate and hence the related neutrino production rate. If the rate of proton capture by ^{7}Be turns out to be lower than presently believed, the discrepancy between the expected and the observed neutrino numbers may be explained.

D. The CNO Cycles

Radioactive-ion-induced reactions also find their places in the normal and the hot CNO cycles.

In main sequence stars which are somewhat more massive than the sun and already contain C, N and O at their birth, the predominant hydrogen-burning cycle is the normal CNO cycle (Fowler, 1984; Arnold, 1988).

$$^{12}\mathrm{C}(p,\gamma)^{13}\mathrm{N}(e^+\nu)^{13}\mathrm{C}(p,\gamma)^{14}\mathrm{N}(p,\gamma)^{15}\mathrm{O}(e^+\nu)^{15}\mathrm{N}(p,\alpha)^{12}\mathrm{C}$$

which operate at temperatures of 2×10^7 K to 10^8 K. As in the p–p chain, the net result of this cycle is the conversion of four hydrogen nuclei into a helium nucleus: $4\mathrm{H} \rightarrow^4 \mathrm{He} + 2e^+ + 2\nu$, with $Q = 26.73$ MeV (Rolfs, 1988).

In a variety of environments, such as supermassive stars heavier than 10^5 sun masses, X-ray and γ-ray bursters, accreting neutron stars, and in some dense, inhomogeneous cosmologies, the attainable temperatures (2×10^8 K to 10^9 K) may be high enough for the unstable nucleus ^{13}N ($T\frac{1}{2} = 9.965$m) to capture a proton before its positron decay (Wallace, 1981; Arnould, 1988). When the ^{13}N (p,γ) ^{14}O reaction is faster than the ^{13}N positron decay, the normal CNO cycle is converted to the hot-CNO cycle (Truran, 1988; Parker, 1989):

$$^{12}\mathrm{C}(p,\gamma)^{13}\mathrm{N}(p,\gamma)^{14}\mathrm{O}(\beta^{+}\nu)^{14}\mathrm{N}(p,\gamma)^{15}\mathrm{O}(\beta^{+}\nu)^{15}\mathrm{N}(p,\alpha)^{12}\mathrm{C}.$$

The energy generation rate in the hot CNO cycle is at least ten times greater than the normal CNO cycle. The transition can significantly alter the dynamics of the environment (Mathews, 1984). Experimental determination of ^{13}N$(p,\gamma)^{14}$O reaction rate will help to determine when the transition takes place.

E. Other Applications of RIBs

A practical application of RIBs exists in medicine. When heavy charged particles are penetrating, they cause little ionization along their path except at the end of their range. Near their stopping point, there is a great increase in ionization. Cancer therapy requires that the end point coincide with the cancer tumor. Stable ion beams will be employed to deposit sufficiently strong dose because they can be produced in large quantity, but the beams' energies will be determined through the use of their isotopic radioactive ions such as ^{19}Ne and ^{11}C (Chatterjee, 1984). Ions like ^{19}Ne and ^{11}C can emit positrons, which then annihilate with the medium electrons to produce a pair of gamma rays in opposite direction. The origin of annihilation, approximately the end point of the ions deposited, is then located by detecting the gamma rays in coincidence. The energy of the radioactive ions can be adjusted until the origin matches the site of cancer tumor. The energy of the stable

ion beam, that is the therapy beam, is then scaled according to the mass ratio. For example, if ^{19}Ne is found to stop at the desired point with energy E, then the stable ^{20}Ne must have energy equal to (20/19)E to stop at the same point.

RIBs also have many applications in material science (Sawicki, 1985). These include nondestructive inspections of chemical erosion, mechanical wear, etc.

In summary, experiments with RIBs are important to the astrophysical studies of energy generation, nucleosynthesis and the solar neutrino problem. Applications of RIBs in medicine and material science are also interesting and even more applications of RIBs exist in other fields.

1.2 Radioactive Ion Beams Versus Radioactive Ion Targets.

Direct measurement of nuclear reactions involving radioactive nuclei requires the availability of either a Radioactive Ion Beam (RIB) or a Radioactive Ion Target (RIT). Because the conversion factor of stable to radioactive ions is of the order of 10^{-6}, the production rate of radioactive ions is very low. A question than must be asked which approach is more advantageous —– RIB or RIT? Suppose we want to study the nuclear reaction: $A + B \rightarrow X + Y$, where A is a radioactive nucleus and B is a stable one, and $X + Y$ represents the reaction products.

In the RIB technique, projectile A bombards target B directly while in the RIT approach ions of A type are collected to form a target and a stable ion beam of B type from an accelerator is used to bombard it (Figure 1.2). The choice can be made according to which approach leads to more nuclear reaction counts. In the RIT method, the collection of short lived ions to form a target and the bombardment have to take place simultaneously. If they start at the same time, then the total number of reactions during a bombardment period T is (Hagberg, 1985)

$$N_t = N_B \cdot \frac{N_A}{S \cdot \lambda} \cdot \sigma[T + \frac{1}{\lambda}(e^{-\lambda T} - 1)]. \qquad (1-1)$$

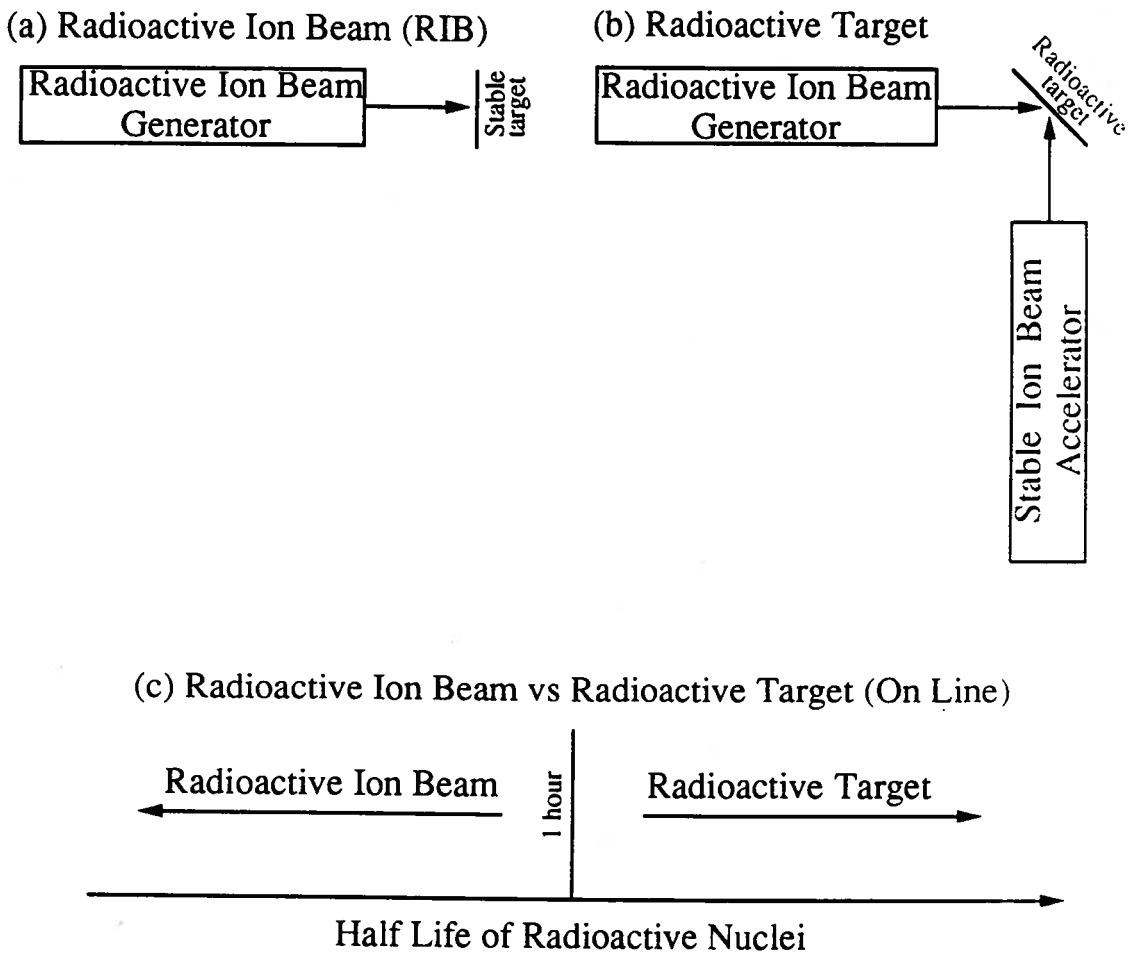

Fig. 1.2 Radioactive beam experiment (a) versus radioactive target (b). The dividing line in terms of half-life of the radioactive nuclei is about one hour (c).

If we assume $T \gg \frac{1}{\lambda} = T\frac{1}{2}/ln2$, as is the case since usually the bombarding time T is much longer than the half-life $T\frac{1}{2}$, N_t is then simplified to

$$N_t = N_B \cdot \frac{N_A}{S \cdot \lambda} \cdot \sigma T. \qquad (1-2)$$

In the RIB case, the number of reactions in time T is

$$N_b = N_A \cdot X_B \cdot \sigma T. \qquad (1-3)$$

In Eqs. (1-1) through (1-3), N_A and N_B are the production rates of radioactive and stable ions, respectively. S is the area of the radioactive target, σ is the total reaction cross section and X_B represents the number of atoms per unit area in the stable target. From Eqs. (1-2) and (1-3), we can determine the ratio

$$N_b/N_t = S\lambda X_B/n_B = SX_B ln2/N_B T\frac{1}{2} \qquad (1-4)$$

Assuming typical values $X_B = 10^{13}$ atoms/cm^2 (equivalent to 200 ug/cm^2 of ^{12}C), S = 0.05 cm^2 and $N_B = 10^{14}$ ions/s, we have

$$N_b/N_t = 3654s/T\frac{1}{2}. \qquad (1-5)$$

Therefore, the critical half-life is $3465s$ or approximately one hour. If the half-life is shorter than one hour, then $N_b/N_t > 1$, and RIB leads to more reaction events. Otherwise, RIT is more productive. Note this conclusion is independent of the primary radioactive beam intensity.

The above conclusion has been drawn without regard to any technical difficulties. It is important to note that RIT requires an additional accelerator to provide the stable ion beam (Fig. 1.2). So RIT is more complicated. Another drawback of

RIT is the strong radiation background from the target (Buchmann, 1987). This might shift the dividing line between RIB and RIT to longer half-lives. Most reactions of astrophysical interest involve nuclei of $T_{\frac{1}{2}} < 1$ hr, so RIB is preferred, if event rates alone are concerned.

In diverse astrophysical environments, nuclear reactions take place at low energies, and another advantage of RIB is the low center-of-mass energy and good energy resolution, due to the inverse kinematics involved. In the reaction $A + B \rightarrow X + Y$, the center-of-mass energy $E_{c.m.} = E_{lab} \cdot M_B/(M_B + M_A)$ and $M_B \ll M_A$ means $E_{c.m.} \ll E_{lab}$. The benefit from using a higher energy secondary beam is its good relative energy resolution, i.e., small ratio of energy spread to average energy, because of less energy losses of more energetic ions.

In summary, the RIB approach has the advantages of simplicity, low $E_{c.m.}$ energy, good energy resolution, and high event rates. This approach has been adopted for our experiments.

1.3 Solenoids Versus Quadrupoles and Dipoles

The RIB approach for nuclear reaction studies requires the production, isolation, and focusing of short-lived radioactive ions.

Radioactive ions are produced through the bombardment of a stable target by a high intensity stable ion beam. In this process, only a very small fraction (10^{-6}) of the stable ions in the beam are converted to radioactive ions, and the secondary radioactive beam usually suffers from poor energy resolution. Also, other types of secondary particles can be produced simultaneously.

Therefore, a good RIB facility (Haight, 1983) should have the ability to

1. Efficiently collect the radioactive beam.

2. Select the radioactive beam and focus it to the desired point.

3. Effectively stop the primary beam and remove scattered residuals.

Conventional devices employing magnetic dipoles (Bimbot, 1985) and quadrupoles (Haight, 1983) usually suffer from low collection efficiency and/or background of unwanted particles (Becchetti, 1988). Quadrupoles have to be used in doublets or triplets to achieve double focusing and usually result in a poor bore/focal length ratio. Apertures necessary to remove undesired ions may be hard to design due to the complicated ion orbits in quadrupoles (Becchetti, 1988).

A device which appears to meet the above requirement 1. to 3. is a solenoid. And one UM superconducting solenoid (20 cm core, 40 cm long, 3.5 Tesla) has been employed to construct a RIB facility. Due to its large bore hence large solid angle, the solenoid allows high-efficiency collection of the secondary ions. When combined with properly installed blocking apertures, its high selectivity ensures effective elimination of background.

A radioactive ion beam with good energy resolution, and relatively free of unwanted particles can therefore be produced.

1.4 Goals of the Thesis Project

The purposes of the project are to 1) construct a RIB facility based on one of the existing superconducting solenoids of the University of Michigan; 2) verify this facility to be the optimal apparatus to produce and focus usable RIBs; 3) achieve best conditions for producing various RIBS and 4) measure differential cross sections for various nuclear reactions induced by these RIBs.

The facility has been constructed in the Nuclear Physics Laboratory at the University of Notre Dame and attached to a dedicated beam line from the university's Van de Graaff accelerator. All data have been collected with Notre Dame's acquisition system, but analyzed with program LISA (Kuhn, 1982) on the DEC Micro-VAX

computer of the Nuclear Physics Group at University of Michigan. Finite Range Distorted Wave Born Approximation (FRDWBA) calculations have been performed with program FRUCK2 (Kunz, 1983).

This thesis is arranged such that details of different parts of the facility are given in Chapter 2; setups for producing ^{8}Li, ^{6}He and ^{7}Be radioactive beams are described in Chapter 3; measured differential cross sections are presented in Chapter 4 and the FRDWBA calculations for comparison with the measured distributions are shown in Chapter 5; conclusions are presented in Chapter 6; and details of kinematic shift, lab to cm conversions, computer ray tracing, preparation of thin target foils and spectra of the production reactions are presented in the Appendices.

CHAPTER 2

INSTRUMENTATION

2.1 Outline of the UM Radioactive Ion Beam Facility

The optimal study of radioactive-ion induced nuclear reactions requires a device which can produce high-intensity energy- and angle-resolved radioactive ion beams (Kolata, 1989a). A facility for this purpose is the University of Michigan Radioactive Ion Beam (RIB) Facility (Fig. 2.1) which is attached to a dedicated beam line from the three-stage Van de Graaff accelerator at the University of Notre Dame. Shown in Table 3.1 is a list of characteristics and specifications of the facility. The front chamber, the solenoid, the mid chamber, and the back chamber are all attached to the aluminum frame by adjustable bolts to allow easy alignment and reconfiguration. All components are non-magnetic and the nearby environment is kept clear of magnetic materials to minimize perturbations of the solenoid's magnetic field. The front chamber contains a piece of quartz for beam alignment, a solid state detector (MON1) for primary beam monitoring, a primary target ladder, and a Faraday cup attached to the bottom of it. In the mid chamber is a movable solid state detector to detect and block the unwanted scattered beam. In the back chamber are an entrance collimator, a second-target ladder capable of holding four targets, a rotatable $\Delta E - t - E_R - xy$ (Fig. 2.6) position sensitive detection system, a monitor detector for coincidence measurements, and also a Faraday cup for beam normalization. A Hall probe is affixed to one edge of the solenoid to measure the

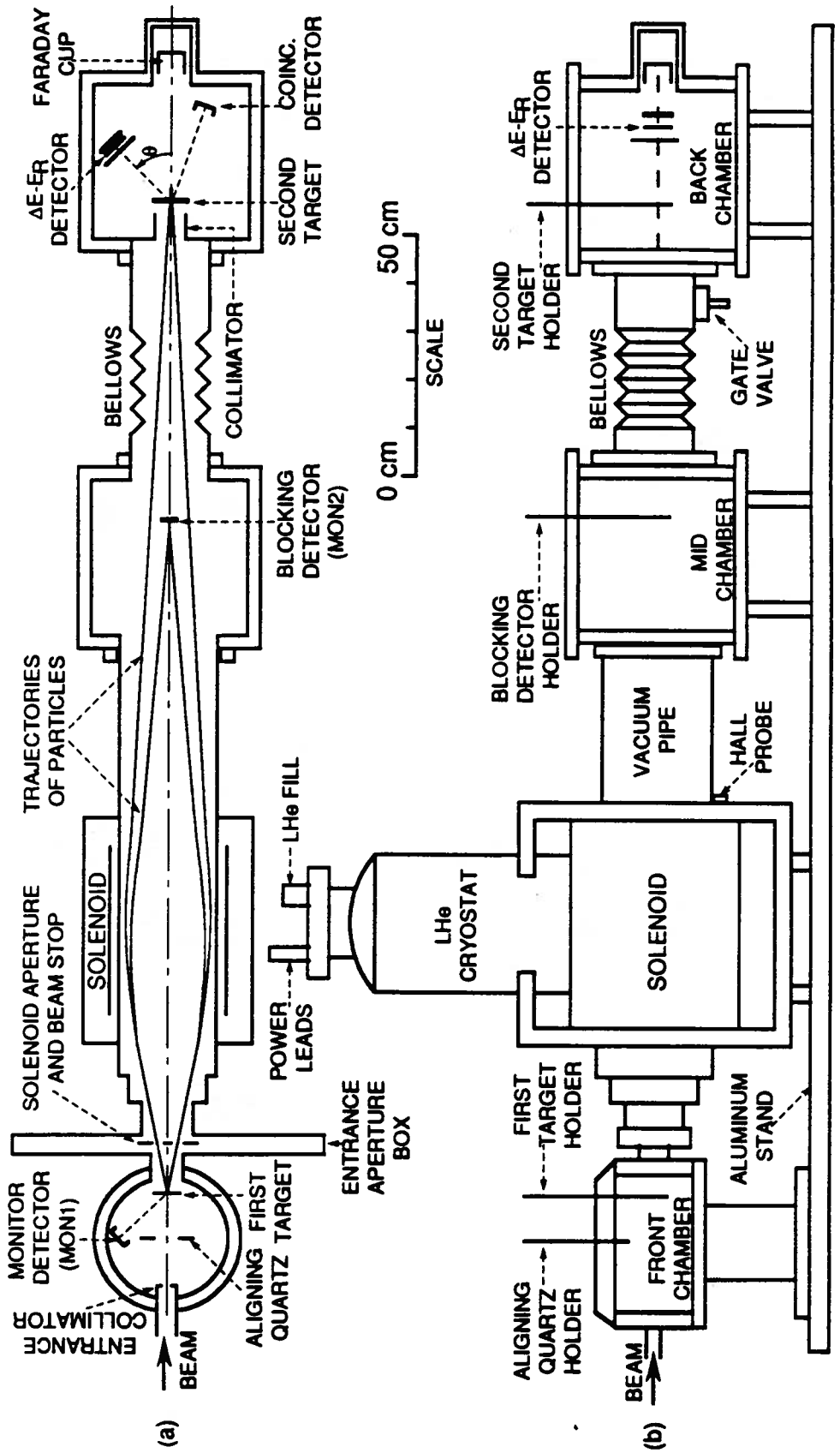

Fig. 2.1 Top view (a) and side view (b) of the UM Radioactive Ion Beam Facility (schematic).

magnetic field strength.

The primary beam (e.g. ^{7}Li) from the University of Notre Dame accelerator impinges on the primary target (e.g. ^{9}Be). The reaction products (e.g. ^{8}Li) are focused with the magnetic solenoid to form a secondary beam that impinges on the secondary target. Secondary reaction products are then detected by the $\Delta E - t - E_R - xy$ detector. The refinement of the secondary beam is accomplished with the combination of the front solenoid aperture, the blocking detector, the back collimator, and the particle selectivity of the solenoid. The specifications and functions of key components are described below.

Table 2.1 Specifications of the UM RIB Facility

1st target to center of solenoid, d_{obj}	52.3 cm
2nd target to center of solenoid, d_{ima}	157.2 cm
Flight path	209.5 cm
Max. particle energy focusable ($I = 125$ A)	17.5 $\frac{q^2}{M}$ MeV
Maximum solid angle ($\theta = 0°$ to 10.2°)	99 msr
Typical solid angle ($\theta = 5°$to10°)	72 msr
Angular magnification M_θ	1/3
Transverse magnification M_T	3
Secondary beam size at focal point	1 cm dia.

2.2 The University of Michigan Superconducting Solenoid

The heart of the UM RIB facility is the superconducting solenoid. Its superiority over other conventional focusing devices is manifested by its high collection and transmission efficiencies. The key dimensions of the solenoid are shown in Fig. 2.2. When operated in an asymmetric mode with object distance $d_{obj} = 52.3$ cm and image distance $d_{ima} = 157.2$ cm, as indicated in Fig. 2.3, the solenoid has an acceptance angle of 10.2° corresponding to a solid angle of 99 msr (milli-steradian). This unusually large solid angle is to be compared with typical solid angles of a few msr in other RIB devices (Bimbot, 1985; Haight, 1983). The importance of a large solid angle lies in the fact that secondary, radioactive ion are rare and must be

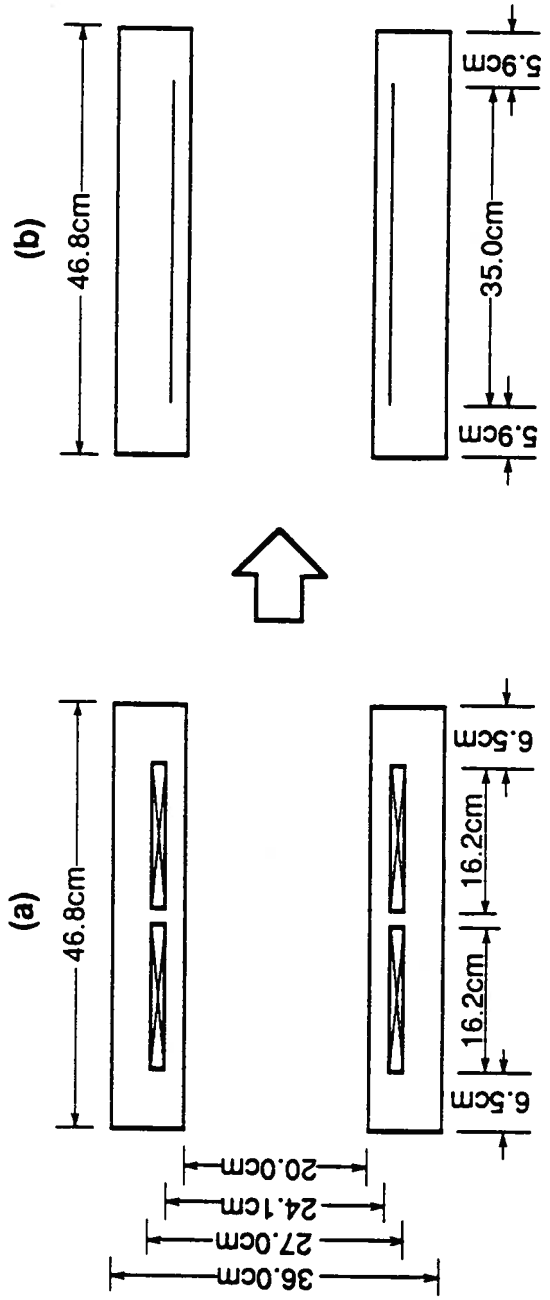

Fig. 2.2 Dimensions of the solenoid coils (a) and their infinitely thin coil equivalence (b). The wire is NbTi + Cu superconductor.

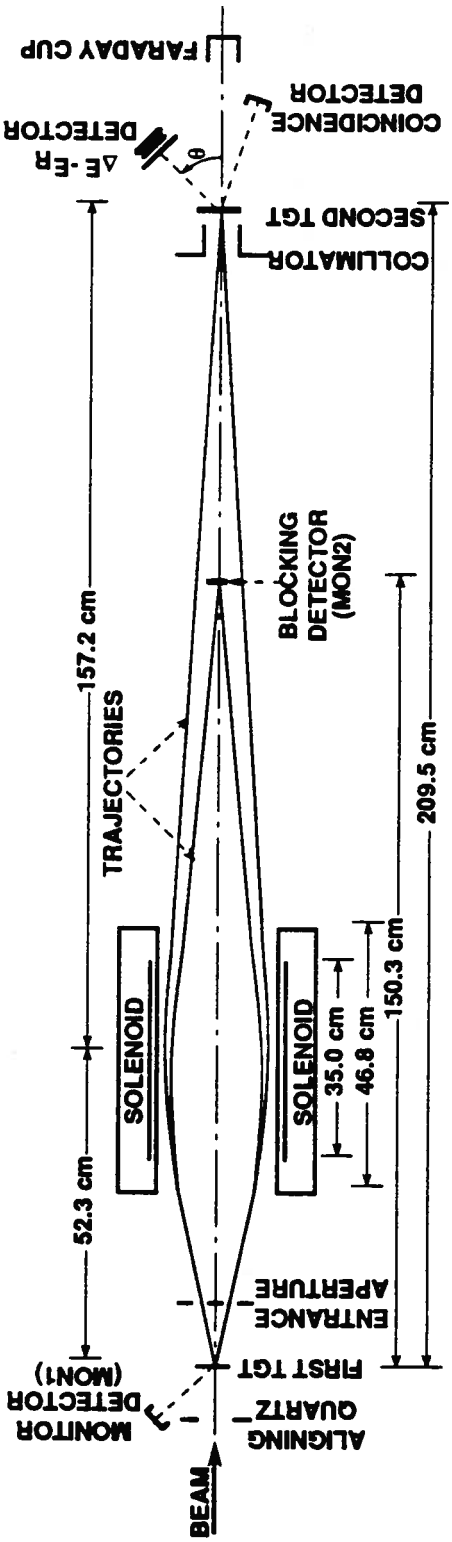

Fig. 2.3 Configuration of the solenoid lens (top view).

collected as efficiently as possible to form a usable secondary beam. Another advantage of the solenoid is its short focal length (due to its strong magnetic field) relative to its bore, i.e., a large ratio of bore/focal length. Consequently, particle decay during flight is minimal and loss of ions due to geometrical limitations is negligible. This results in a high transmission efficiency.

Table 2.2 Properties of the Solenoid

Solenoid coil length	32.4 cm
Solenoid coil inner diameter	24.1 cm
Solenoid coil outer diameter	27.0 cm
Effective thin coil diameter	24.1 cm
Effective thin coil length	35.0 cm
Solenoid inductance	$\sim$ 12.5 Henry
Max. field (at 125 amp)	3.5 Tesla
Stored energy (at 125 amp)	$\sim$ 98 KJ
Cryostat bore diameter	20.0 cm
Cryostat bore length	46.8 cm

The solenoid[1] itself consists of two identical cylindrical coils closely spaced and encased in a liquid helium cryostat which keeps the coils superconductive by maintaining the temperature at 4.2 K. As long as the magnetic field alone is concerned, the pair of thick coils can be replaced by a single infinitely thin cylindrical current sheet, as shown in Fig. 2.2. If the origin of the z-axis coincides with the solenoid center, then the magnetic induction on the z-axis B_{z0} can be written as

$$B_{z0} = k_1 \cdot I \left\{ \frac{z + l_m/2}{[r_m^2 + (z + l_m/2)^2]^{\frac{1}{2}}} - \frac{z - l_m/2}{[r_m^2 + (z - l_m/2)^2]^{\frac{1}{2}}} \right\}, \qquad (2-1)$$

where r_m is the radius of the current sheet and l_m is its length, I is the solenoid current and k_1 is a proportion constant. For the UM superconducting solenoid, $r_m = 12.05$ cm, $l_m = 35.0$ cm (Stern, 1987), and $k_1 = 1.70 \times 10^{-2} \frac{Tesla}{Amp}$. So that at the center of the solenoid and at $I = 125$ amp

$$B_{z0\max} \equiv B_z(r = 0, z = 0) = 3.5 \text{ Tesla}. \qquad (2-2)$$

An important quantity that can be derived from Eq. (2-1) is the integral

$$(\overline{B_z^2 L}) \equiv \int_{-\infty}^{\infty} B_{z0}^2 dz.$$

If $I = 125$ Amp and r_m, l_m and k_1 take the values given above, then

$$(\overline{B_z^2 L})_{max} = 3.685 T^2 \cdot m. \qquad (2-3)$$

In terms of electric current I, $(\overline{B_z^2 L})$ can be written

$$(\overline{B_z^2 L}) = k_2 \cdot I^2 = (2.358 \times 10^{-4} \frac{T^2 \cdot m}{Amp^2}) I^2, \qquad (2-4)$$

where $k_2 = 2.358 \times 10^{-4}$ is a result of Eq. (2-3).

Related to the quantity $(\overline{B_z^2 L})$ is the focal length (Cosslett, 1950)

$$f = \frac{4(B\rho)^2}{(B_z^2 L)}, \qquad (2-5)$$

where $B\rho = p/q = Mv/q$ is the magnetic rigidity of the ion. Alternatively, f can be expressed as

$$f = \frac{351.53}{I^2} \frac{ME}{q^2}, \qquad (2-6)$$

where Eq. (2-4) has been employed; and I is the electric current in Amp, M is the mass of the ion in amu, E is the ion energy in MeV and q is the charge state of the ion, f is the focal length in meter.

Three statements can be made based on Eq. (2-6) and the relation between object and image distances d_{obj} and d_{ima}

$$\frac{1}{d_{obj}} + \frac{1}{d_{ima}} = \frac{1}{f} \qquad (2-7)$$

First, there is a limit on the focusable energy. In the asymmetric mode $d_{obj} =$

52.3 cm and d_{ima} = 157.24 cm, as indicated in Fig. 2.3 or Table 2.3,

$$f = \frac{d_{obj} \cdot d_{ima}}{d_{obj} + d_{ima}} = 0.392\ m \qquad (2-8)$$

This means, when combined with Eq. (2-6) that

$$E = 1.115 \times 10^{-3} \frac{q^2}{M} \cdot I^2, \qquad (2-9)$$

where the units of E, q, M and I are the same as before. At I = 125 Amp (maximum current),

$$E_{max} = 17.45 \frac{q^2}{M}\ (\text{MeV}) \qquad (2-10)$$

This is the maximum focusable energy. As an example, $M(^8\text{Li})$ = 8.022 amu, E_{max} (^{8}Li) = 19.6 MeV. Particles with higher energies can be focused if d_{obj} and/or d_{ima} are increased.

Table 2.3 Separation of $^7Li^{+3}$ and $^8Li^{+3}$

Particle	$\bar{E}$ (MeV)	M (amu)	$B\rho\ (T \cdot m)$	f(m)	$d_{obj} + d_{ima}$ (cm)
$^7Li^{+3}$	14.2	7.016	0.479	0.341	150.3
$^8Li^{+3}$	14.4	8.022	0.514	0.382	209.5

Second, isotopes of similar energies can be well separated in the solenoid's field. For example, a primary ^{7}Li beam impinges on a 12.7 μm-thick ^{9}Be target, some of the ^{7}Li ions are converted to ^{8}Li ions of $\bar{E}$ = 14.4 MeV but most ^{7}Li ions are just elastically scattered with energy $\bar{E}$ = 14.2 MeV. Fortunately, these ^{7}Li and ^{8}Li ions can be separated because of their different masses. Table 2.3 shows their different properties and resulting image distances. The focal lengths and the image distances have been calculated through Eqs. (2-6) and (2-7). According to Table 2.3, the focal points for ^{7}Li and ^{8}Li are separated by (209.5 - 150.3) cm = 59.2 cm. Thus a block can be installed to stop the unwanted ^{7}Li ions (Fig. 2.1).

Third, particles of different species but the same rigidity will be focused to the same point simultaneously. This statement results from Eq. (2-9), which is rewritten as

$$\frac{ME}{q^2} = 1.115 \times 10^{-3} I^2 \qquad (2-11)$$

All species of particles with the same combination $\frac{ME}{q^2}$ will be focused, resulting in impurity of the secondary beam. This problem can be solved by introducing electric fields into the solenoid's magnetic field (Liu, 1987), because different types of particle of the same magnetic rigidity usually have different electric rigidities.

In summary, the solenoid can collect and transmit the radioactive ion with high efficiencies. It can separate isotopes of similar energy but cannot separate different types of particles of the same magnetic rigidity. Electric fields may have to be invoked for the latter if required.

2.3 The Solenoid Entrance Apertures

Four solenoid entrance apertures of different openings, placed side by side, are housed in a long, rectangular, vacuum tight aperture holder located between the first target and the solenoid. The apertures are all movable from outside through a long shaft of one quarter inch diameter, which extends to the inside of the holder through a CAJON[2] fitting and can slide in and out. One can put the desired aperture into position without opening up the vacuum system. Fig. 2.4 shows the apertures geometry and Table 2.4 lists their sizes. The apertures are made of brass with thin carbon disks to stop the primary beam.

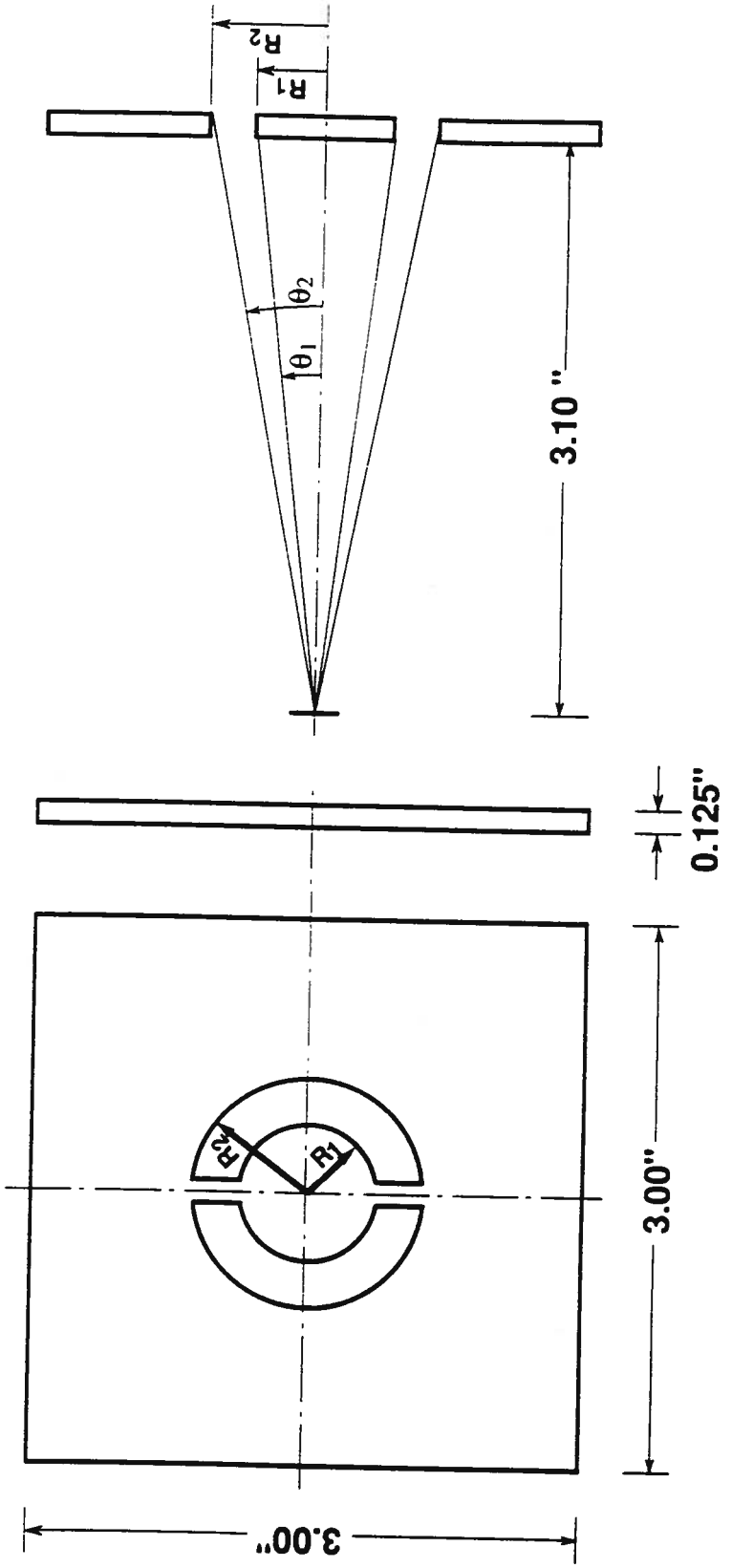

Fig. 2.4 Geometry of the solenoid entrance aperture.

Table 2.4 Specifications of Apertures

Aperture	θ_1 (deg)	θ_2 (deg)	R_1 (mm)	R_2 (mm)	$\Delta\Omega$ (msr)
1	3	11	4.14	16.92	107
2	5	11	6.91	16.92	92
3	4	8	5.51	12.24	46

The primary function of the aperture is to stop unwanted particles. When the primary beam impinges on the first target, most ions will be elastically scattered into the small angle region (i.e. the near-axis region) since usually elastic scattering has a large cross section and is very forward-peaked. So it is very desirable to block the near zero-area in order to stop the scattered ions. Also, the residual beam, which is part of the primary beam that penetrates the target, must be stopped. This is done by the central carbon disk of the aperture. The solid angle $\Delta\Omega$ is related to θ_1 and θ_2 through

$$\Delta\Omega = 2\pi \int_{\theta_1}^{\theta_2} sin\theta d\theta, \qquad (2-12)$$

where θ_1 and θ_2 are the lower and upper limits of angle, respectively. It can be seen that $d\theta$ at small θ makes little contribution to $\Delta\Omega$. Therefore, the central disk does not cause much reduction of solid angle.

The second function of the aperture is to define the solenoid's acceptance solid angle and the energy spread of the secondary ions. In the nuclear reaction $A+B \rightarrow X+Y$, as schematically shown in Fig. 2.5, the energy $E(\theta_3)$ of the ejectile nucleus is a function of θ_3 which decreases with increasing θ_3. As a consequence, a large angular range of the aperture opening results in a large energy spread, i.e. poor energy resolution of the secondary ion beam. On the other hand, a solid angle as large as possible is required for good ion collection. A compromise must therefore be made: the solid angle must be large enough to allow a high collection efficiency but must be small enough to allow a good energy resolution. This can be accomplished

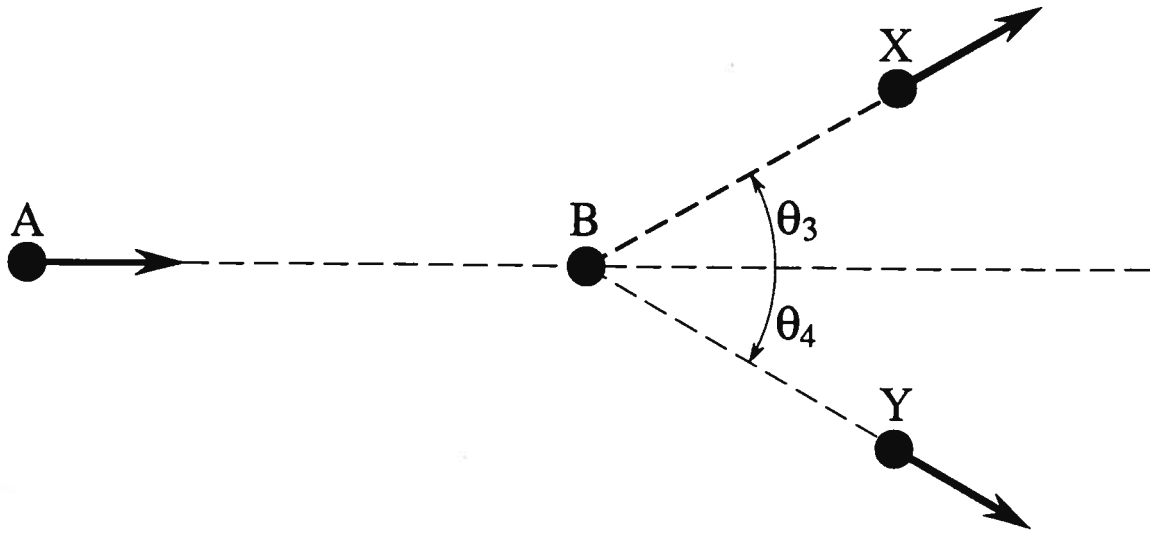

Fig. 2.5 Schematic of two-body nuclear reactions $A + B \rightarrow X + Y$.

by choosing the proper aperture out of the several available in the aperture holder. Most nuclear reaction studies of astrophysical interest do not require high energy resolutions. Thus, large solid angles were used in our experiments to favor the high secondary beam intensities.

2.4 The Blocking Detector and the Back Collimator

The blocking detector and the back collimator both serve to purify the radioactive beam. First, although the residual primary beam and the primary ions scattered into the small angle region are stopped by the central disk of the entrance aperture, many ions of the same origin still go through the ring-shape opening of the aperture to enter the solenoid and will be focused to a point on the beam axis. The blocking detector is centered at this point to stop them. The detector is one inch in diameter and has a front aperture with a 1/8 inch aligning hole at its center. It can be moved until it detects the maximum current, which signifies that it has been aligned with the beam to be stopped. The elastically scattered primary ions are usually separable from the radioactive ions since the latter are heavier by one or more neutron masses. For example, if the primary beam is ^{7}Li, the radioactive beam is ^{8}Li. The focal points of ^{7}Li and ^{8}Li are apart by 59.2 cm, as calculated in Section 2.1.

Since for a fixed configuration the rate of the elastically scattered ions collected by the blocking detector is proportional to the production rate of any type of ions involved, the detector can also be calibrated to measure the intensities of the primary and the secondary beams.

Second, particles other than the desired radioactive ions are also produced. As an example, when a ^{7}Li beam is directed to a ^{9}Be target, particles such as ^{2}H, ^{4}He, ^{6}He are produced besides ^{8}Li (Appendix D). Different particles will be brought into

rings of different diameters on the focal plane at the second target position while the desired radioactive ions are focused into a small spot ($\sim$ 1 cm diameter). The back collimator has a diameter of 2 cm and a length of 4.4 cm, so only well focused ions can go through it and reach the second target to initiate secondary nuclear reactions.

2.5 Normalizations of Primary and Secondary Beams

In the experimental set-up shown in Fig. 2.1(a), all types of ions involved are produced in fixed proportions, for fixed geometries. For the secondary beam normalization, the second target is removed. The $\Delta E - E_R$ detector, if positioned at zero degree, will then collect all radioactive ions passing through the back collimator. Meanwhile, the monitor in the front chamber (MON 1) will collect back scattered primary beam ions. The monitor output can then be used to calculate the number of radioactive ions since the former is proportional to the latter.

For the primary beam normalization, the beam, after penetrating the first target, is allowed to travel all the way downstream without meeting any obstacles until it reaches the back Faraday cup at the end of the beam line. The number of ions collected by the Faraday cup is then proportional to the front monitor output.

Now that intensities of both primary and secondary beams can be determined through the monitor output, the conversion efficiency can also be determined. For example, a conversion rate of (6.2×10^6 ions of ^{7}Li/per ion of ^{8}Li) was obtained with a 12.7 μm-thick ^{9}Be target, a front aperture of $5° - 11°$ and a back collimator of 2 cm diameter.

2.6 The $\Delta E - t - E_R - xy$ Detector Telescope

The $\Delta E - t - E_R - xy$ detector telescope consists of a thin planar Si surface barrier detector[2] and a thick boron-implanted Si detector[3] with a two dimensional

resistive cathode and up/down, right/left electrodes. Table 2.5 contains the specifications of the detector system and Fig. 2.6 shows the geometries. The detector is mounted on an arm which is movable around the rotation axis of the second target and which is such that the center of the ΔE detector is 121 mm away from the axis. The 17.4 μm ΔE detector is a fully depleted transmission detector to measure the energy loss when a particle passes through it. The rest of the particle energy is deposited in the 200 μm thick position-sensitive $E_R - xy$ detector. The ΔE and E signals then combine to give the particle's total energy E_T and the product MZ^2:

$$E_T = \Delta E + E_R, \qquad (2-13)$$

$$\Delta E \cdot E_T \approx kMZ^2 \qquad (2-14)$$

where M and Z stand for the mass and atomic number of the particle, respectively; k is a constant to be determined by a known particle and its known ΔE and E_R. Eq. (2-14) is used for particle identification because it gives the quantity MZ^2.

Table 2.5 Specification of the $\Delta E - t - E_R - xy$ detector telescope.

ΔE detector:	
Active area	200 mm^2
Thickness	17.4 μm @ 10 v
$E_R - xy$ detector:	
Size	25mm $\times$ 25 mm
Thickness	200 μm @ 200 v
$\Delta E - t - E_R - xy$ detector	
Energy resolution (8.78 MeV α)	$\sim$ 120 keV FWHM
Position resolution	$<$ 1 mm FWHM
Time resolution	$<$ 1 n sec FWHM

The $E_R - xy$ position sensitive detector also provides information on the particle's incidence position. On the back side of the detector is a high-resistance cathode of square shape with an electrode on each side (Fig. 2.6). The electric charge

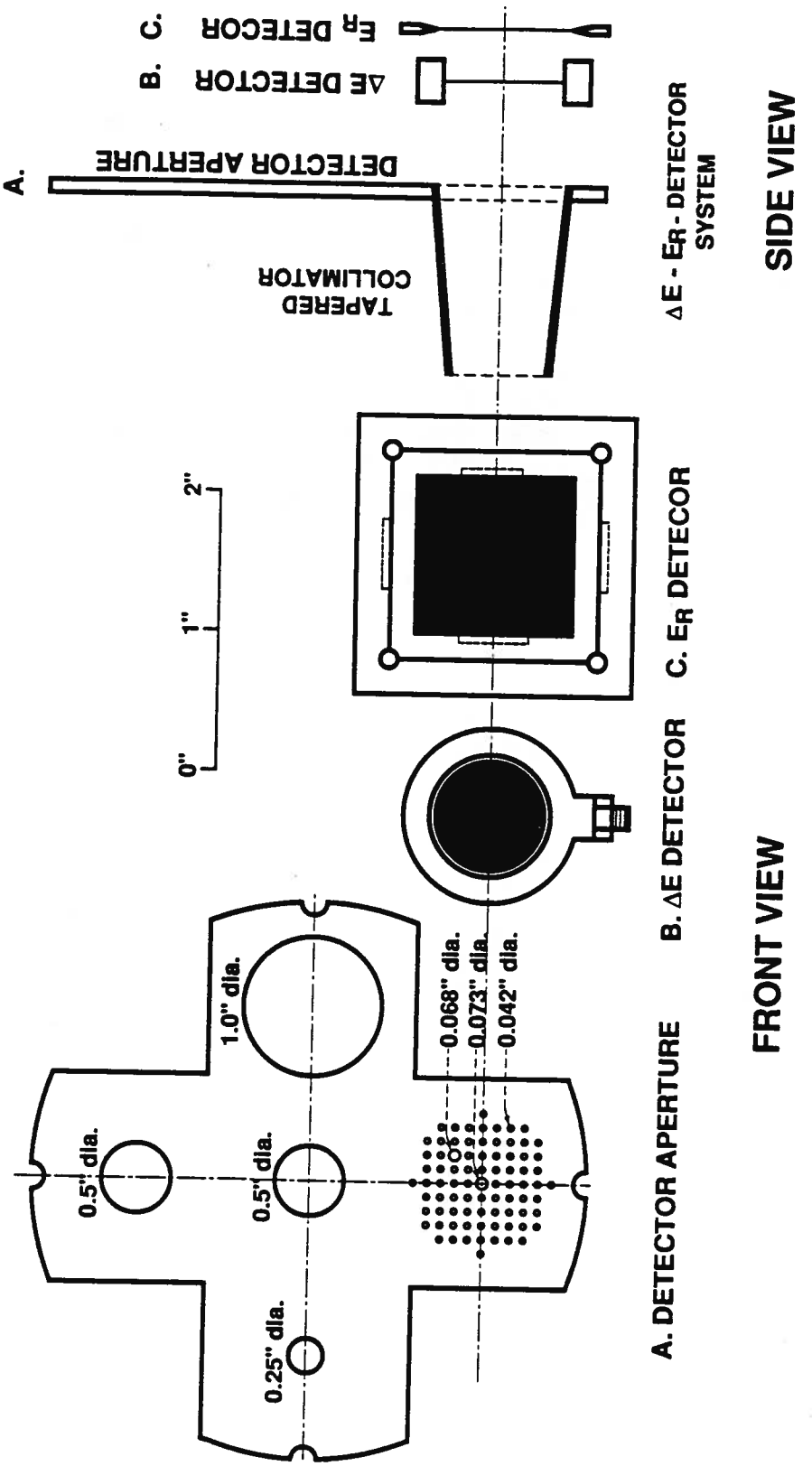

Fig. 2.6 Components of the $\Delta E - t - E_R - xy$ detector and their configuration.

(which is proportional to energy loss) resulting from the particle's ionization is divided among the four electrodes, according to the relative distances of the electrodes from the point of incidence. Each incidence point results in a unique pair of $[E(x), E(y)]$ if the latter are formed as follows,

$$E(x) = f\left[\frac{E(right) - E(left)}{E(right) + E(left)}\right], \qquad (2-15)$$

$$E(y) = f\left[\frac{E(up) - E(down)}{E(up) + E(down)}\right], \qquad (2-16)$$

where f is a linear function and E is the appropriate energy signal. The mapping $(x, y) \leftrightarrow [E(x), E(y)]$ is one-to-one, so each pair of $[E(x), E(y)]$ determines a unique position. The position information is necessary for angle information and kinematic calculations. Combined with the movability of the detector support arm, this position sensitivity allows the optium beam focusing to be determined empirically.

In front of the detector system is a rotatable set of apertures to define the detector's solid angle and a grid for $x - y$ positron calibration. The tapered tube in front of the aperture limits the acceptance of the detector so that only products from the second target are detected. This reduces the interference of any background ions.

The beauty of the $\Delta E - t - E_R - xy$ detector system is that it provides energy and position signals simultaneously for a large solid angle (13 msr to 30 msr). Its function is equivalent to a large array of small detectors but it requires only simple electronic circuits.

2.7 The Coincidence Detector

The coincidence detector (E_{coinc}) has an active area of 600 mm^2 and a thickness of 300 μm. Its center is 21.0 cm away from the second target rotation axis so it

subtends a solid angle of 13.6 msr. Its position is shown in Figs. 2.1 and 2.3. It can record recoil ions coincident with ejectile ions collected by the $\Delta E - t - E_R - xy$ detector to eliminate false events. The output of the detector is proportional to the secondary beam intensity, with a fixed scaling factor for a fixed second target, so it can also be used to facilitate normalizations between runs with the same target.

2.8 The Electronic Circuits

The electronic circuits up to the point of the analog-to-digital converter (ADC) used in our experiments are shown in Figs. 2.7 and 2.8.

In the figures, inputs "E" and "T" mean the energy and timing signals, respectively, from the Si detector preamplifiers. The symbols in the parenthesis are the names of the detectors or electrodes. For example, $E(\Delta E)$ and $T(\Delta E)$ stand for the energy and timing signals from the preamplifier of the ΔE detector; $E(left)$ stands for the energy signal from the preamplifier of the left electrode of the $E_R - xy$ detector, etc.

For each event, the energy pulses are recorded from the $\Delta E, E_R, E_{coinc}$ detectors and the up/down, right/left electrodes (Fig. 2.7). They can later be scaled and combined on a computer to generate quantities of interest such as total energy E_T and $[E(x), E(y)]$. The energy signal from the monitor (MON1) is also recorded for beam normalizations.

In Fig. 2.8, the timing signals are used for coincidence measurements. When $T(\Delta E)$ and $T(E_R)$ are in coincidence, only events of particles with energies sufficient to penetrate the ΔE detector will be registered. This presorts the data to be recorded. If desired, $T(E_{coinc})$ can also be set in coincidence with $[T(\Delta E)$ and $T(E_R)]$, so an event will be recorded only when the E_{coinc} detector detects a recoil ion and the $\Delta E - E_R$ detector detects an ejectile ion simultaneously. This can be

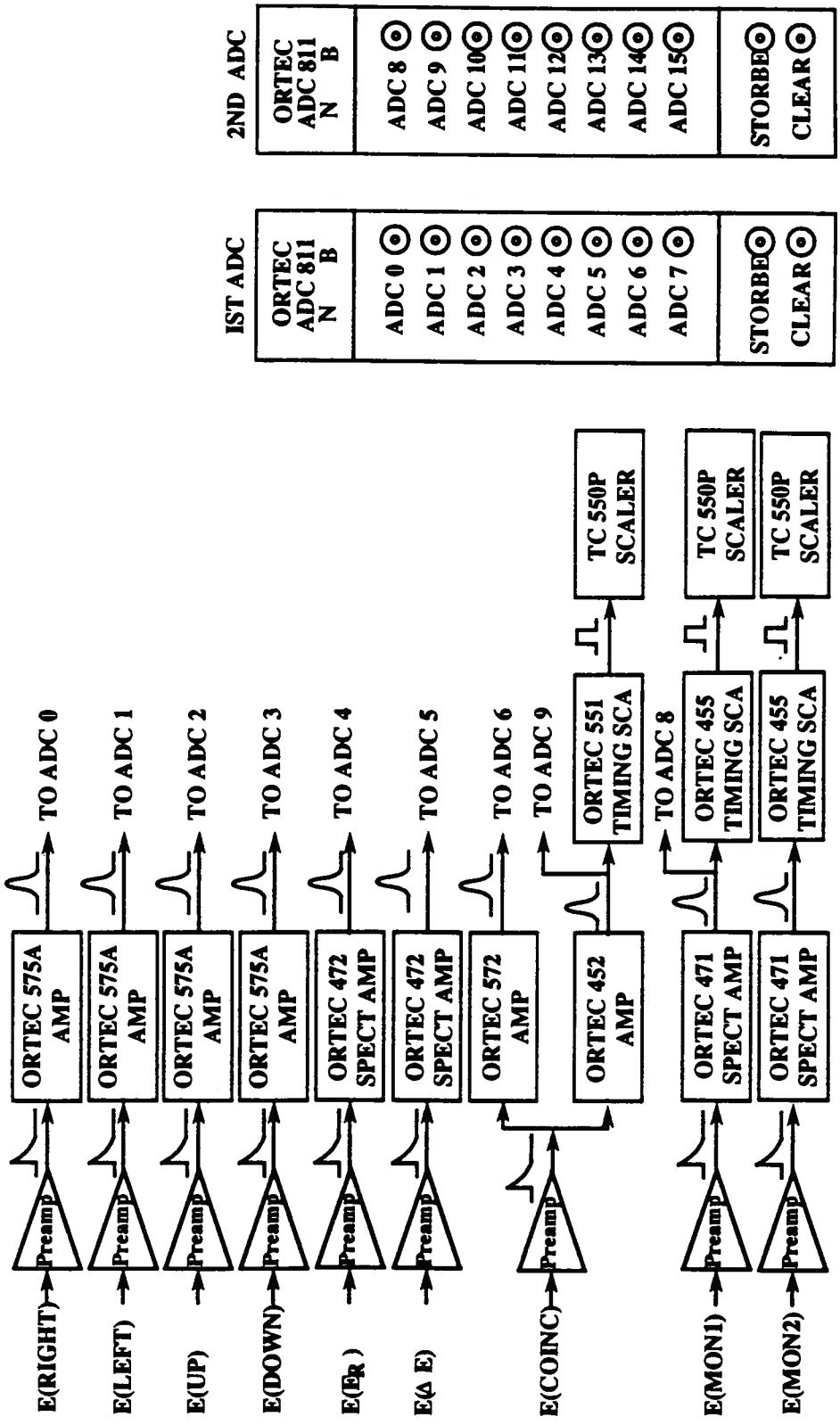

Fig. 2.7 Energy signals and associated circuitry.

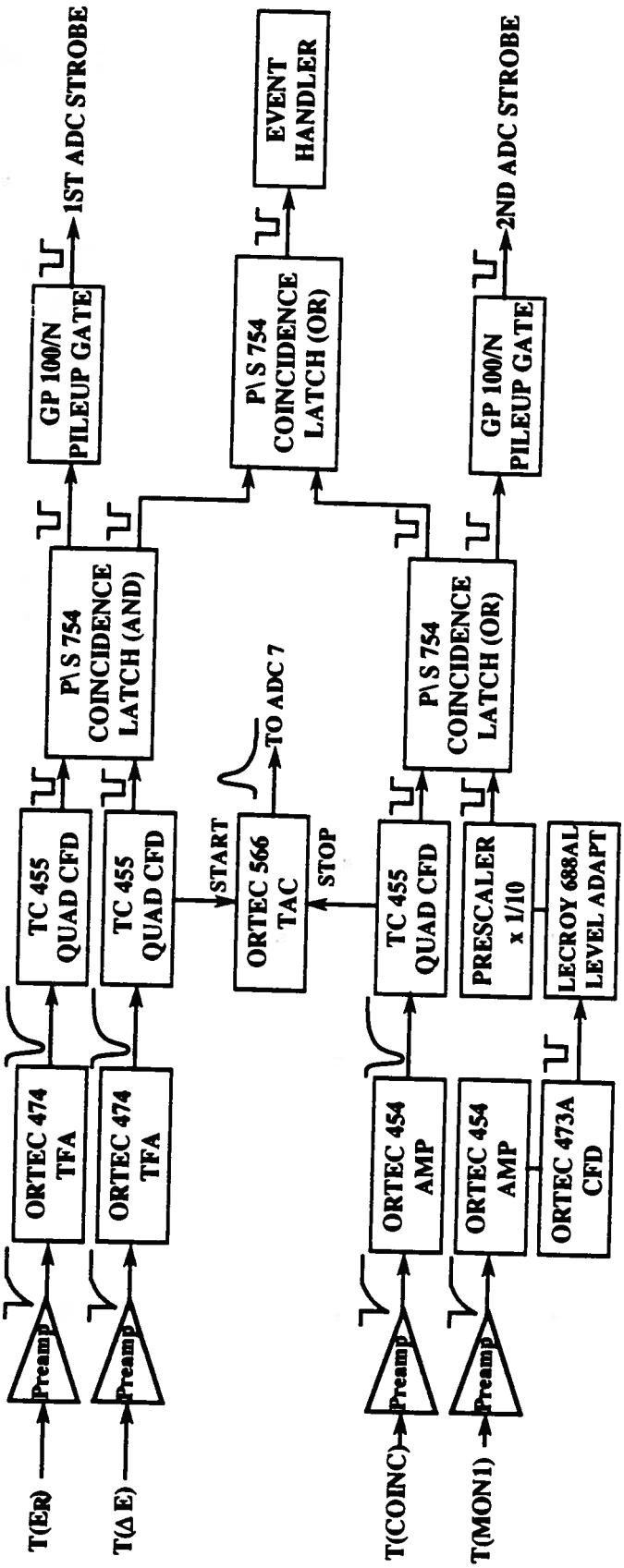

Fig. 2.8 Coincidence circuits.

important for rare-event experiments like ours to exclude false events.

2.9 Energy Calibrations

Calibrations of the low energy range (5.34 MeV to 8.78 MeV) were done with a ^{228}Th α-source[4], while for the high energy range (around 14 MeV) ion beams from the Notre Dame accelerator were used. A $^{228}_{90}$Th nucleus decays through the following decay chain:

$^{228}_{90}$Th $\longrightarrow$	$^{224}_{88}$Ra $\longrightarrow$	$^{220}_{86}$Rn $\longrightarrow$	$^{216}_{84}$Po $\longrightarrow$
	+	+	+
	5.42/5.34 MeV α	5.69 MeV α	6.29 MeV α
		$^{212}_{84}$Po $\longrightarrow$	$^{208}_{82}$Pb (stable)
$^{212}_{82}$Pb $\longrightarrow$	$^{212}_{83}$Bi	+	+
+	+	2.251 MeV β-	8.78 MeV α
6.78 MeV α	0.331 MeV β-	+	+
		$^{208}_{81}$Tl $\longrightarrow$	$^{208}_{82}$Pb (stable)
		+	+
		8.78 MeV α	1.7986 MeV β-

In this decay chain, α-particles are produced mainly at five distinctive energies, corresponding to the five main peaks in the energy spectrum (Fig. 2.9). In each of our experiments, the $\Delta E - t - E_R - xy$ detector telescope was exposed to a 0.1 μ Ci ^{228}Th source located at the second target position and an energy spectrum was taken. A ^{7}Li beam was then used to bombard a 0.85 mg/cm^2 Au target. The beam energy was 14.63 MeV, and the scattered ^{7}Li ions had an energy of 14.13 MeV at 30°, the angle of the telescope.

The ΔE detector is a large Si detector of 17.4 μm thickness, with a 40 μg/cm^2 Au front window and a 40 μg/cm^2 Al back window. Since the window and Si thicknesses and total energies are known, the particle's energy loss in the detector can be calculated through energy loss tables (Ziegler, 1980). Since the α and ^{7}Li particles are stopped, the residual energy deposited in the 200 μm thick $E_R - xy$ detector is simply $E_R = E_T - \Delta E$. Table 2.6 shows several $\Delta E, E_R$ values so determined and their corresponding raw channel number (channel numbers as

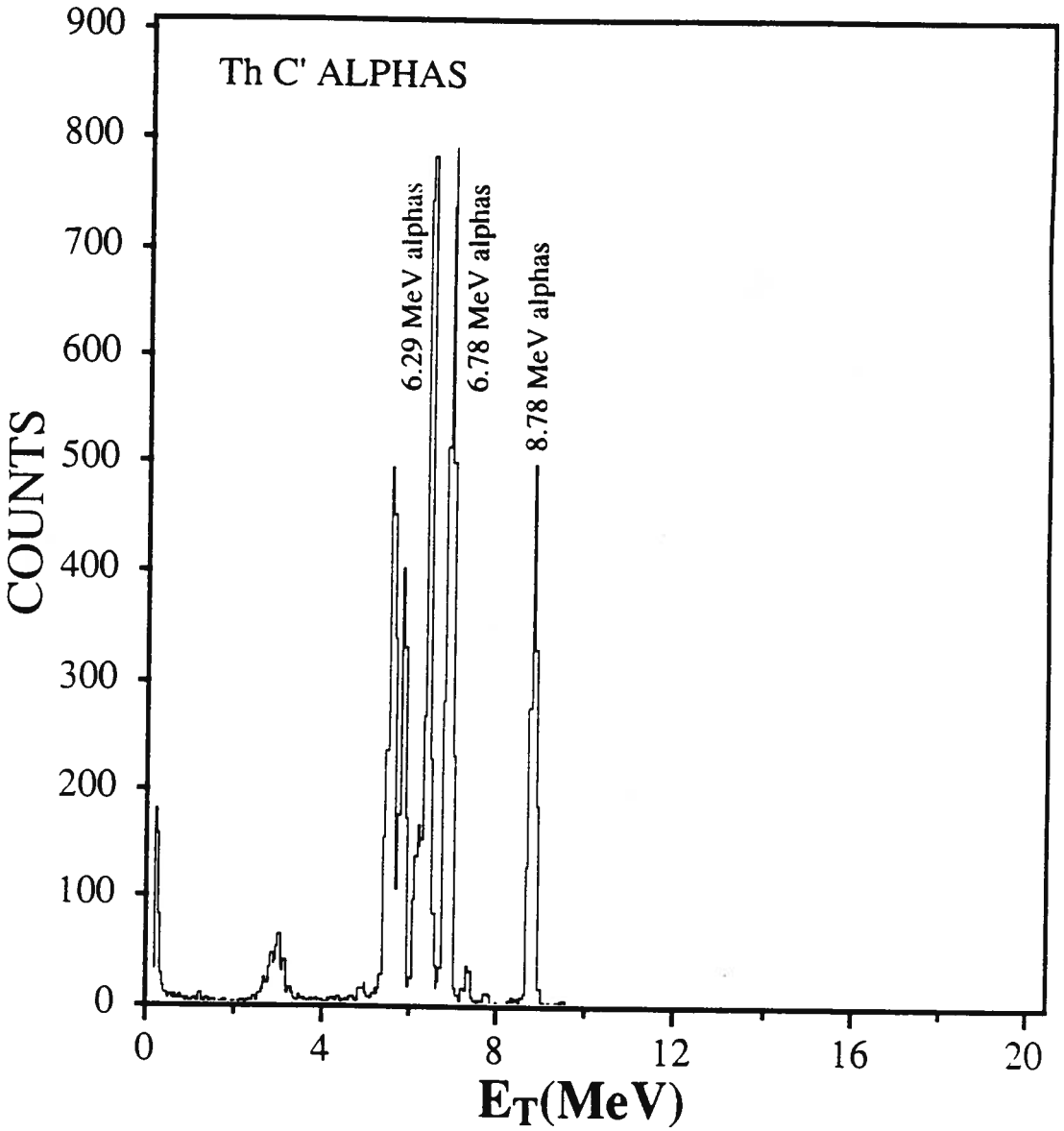

Fig. 2.9 Energy spectrum of α-particles from the ^{228}Th source.

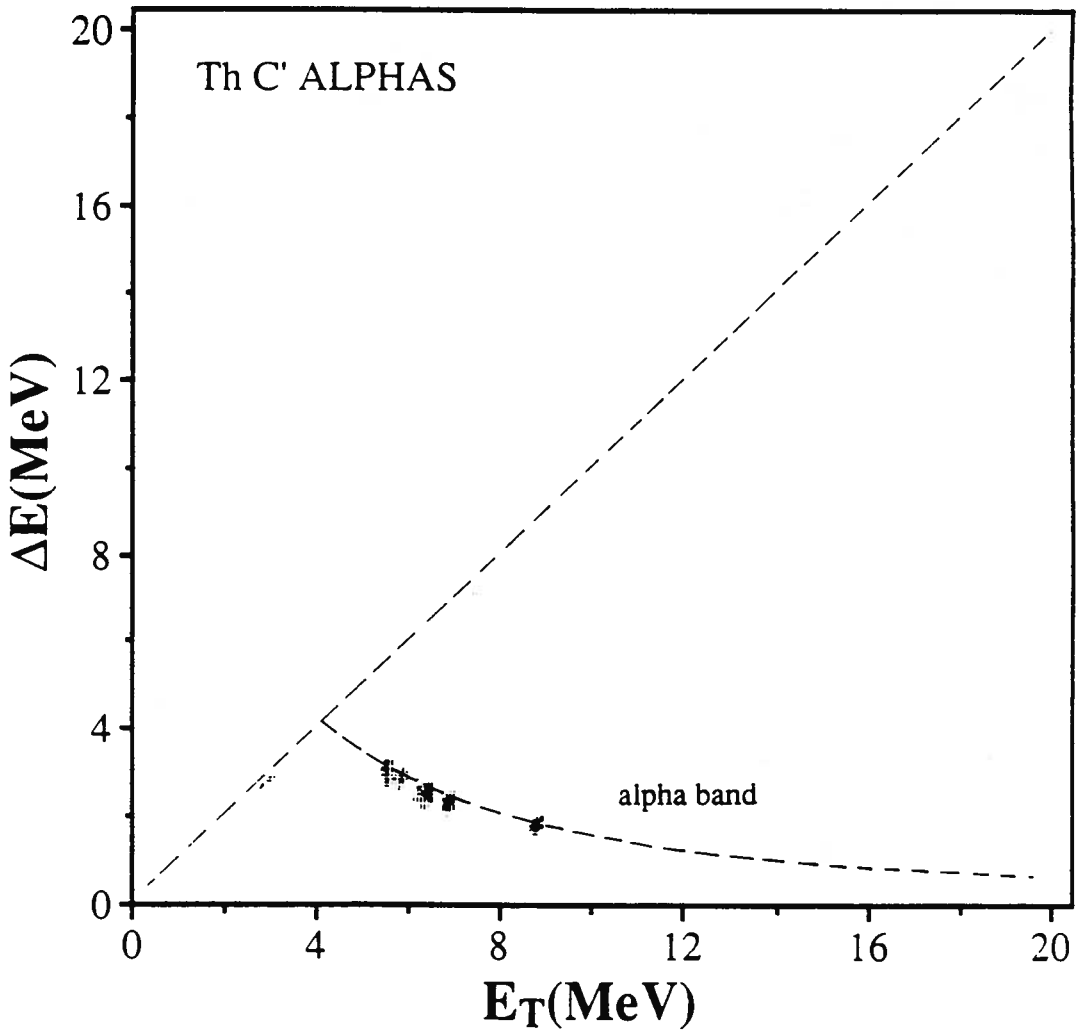

Fig. 2.10 $\Delta E - E_T$ spectrum of α-particles from the ^{228}Th source.

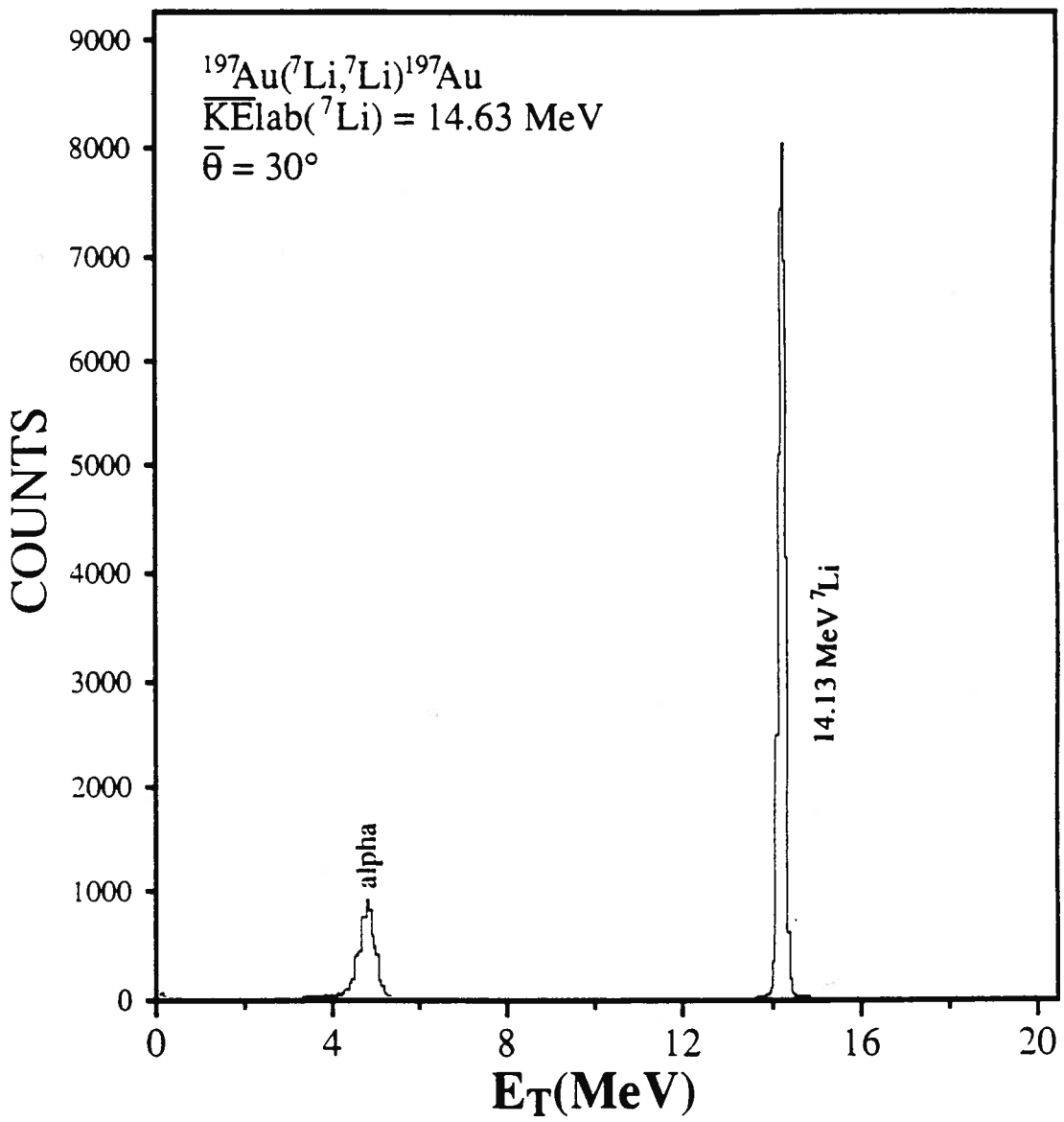

Fig. 2.11 Energy spectrum of the 14.63 MeV ^{7}Li beam scattered by the 0.85 mg/cm^2 Au target at $\bar{\theta}_{lab} = 30°$.

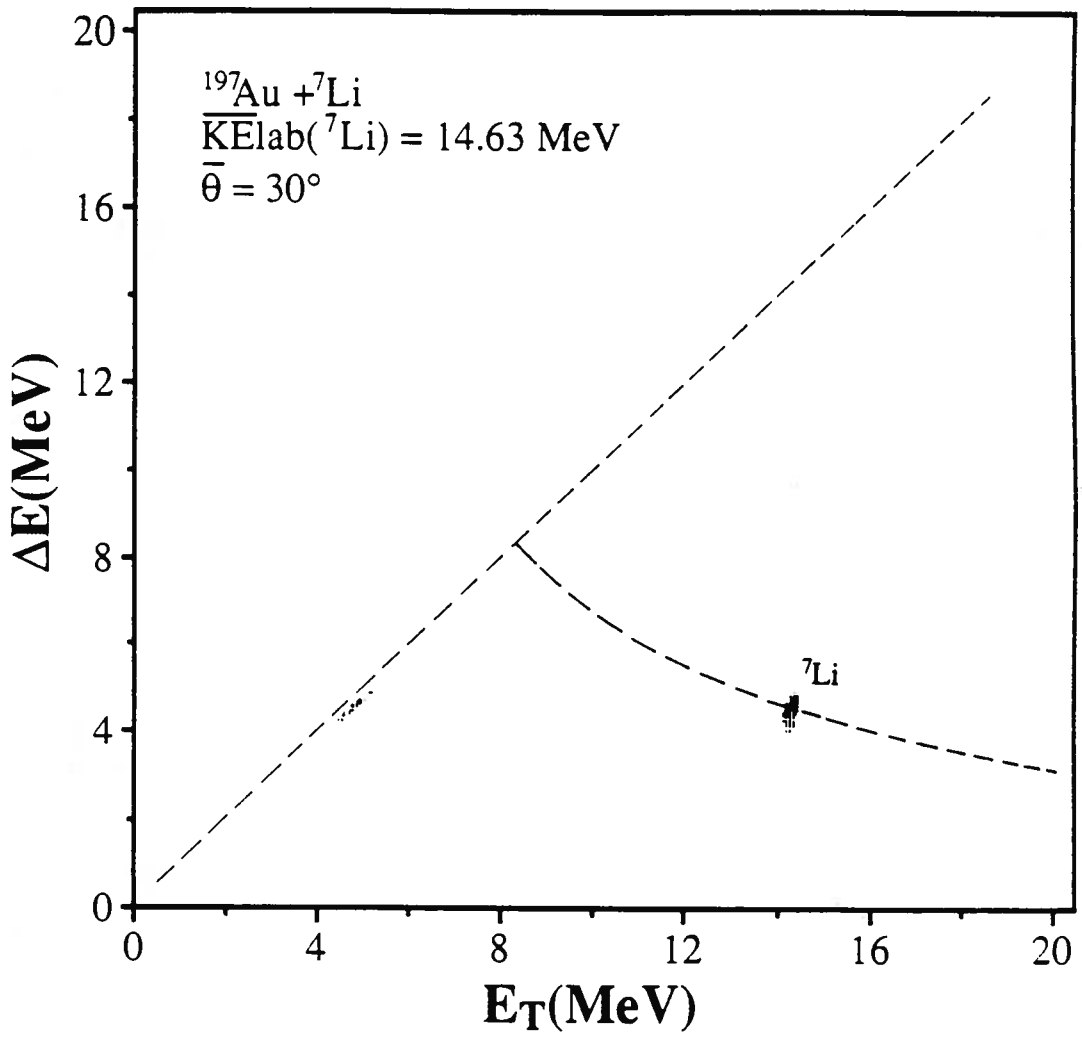

Fig. 2.12 $\Delta E - E_T$ spectrum of a 14.63 MeV ^{7}Li beam scattered by the 0.85 mg/cm^2 Au target at $\bar{\theta}_{lab} = 30°$.

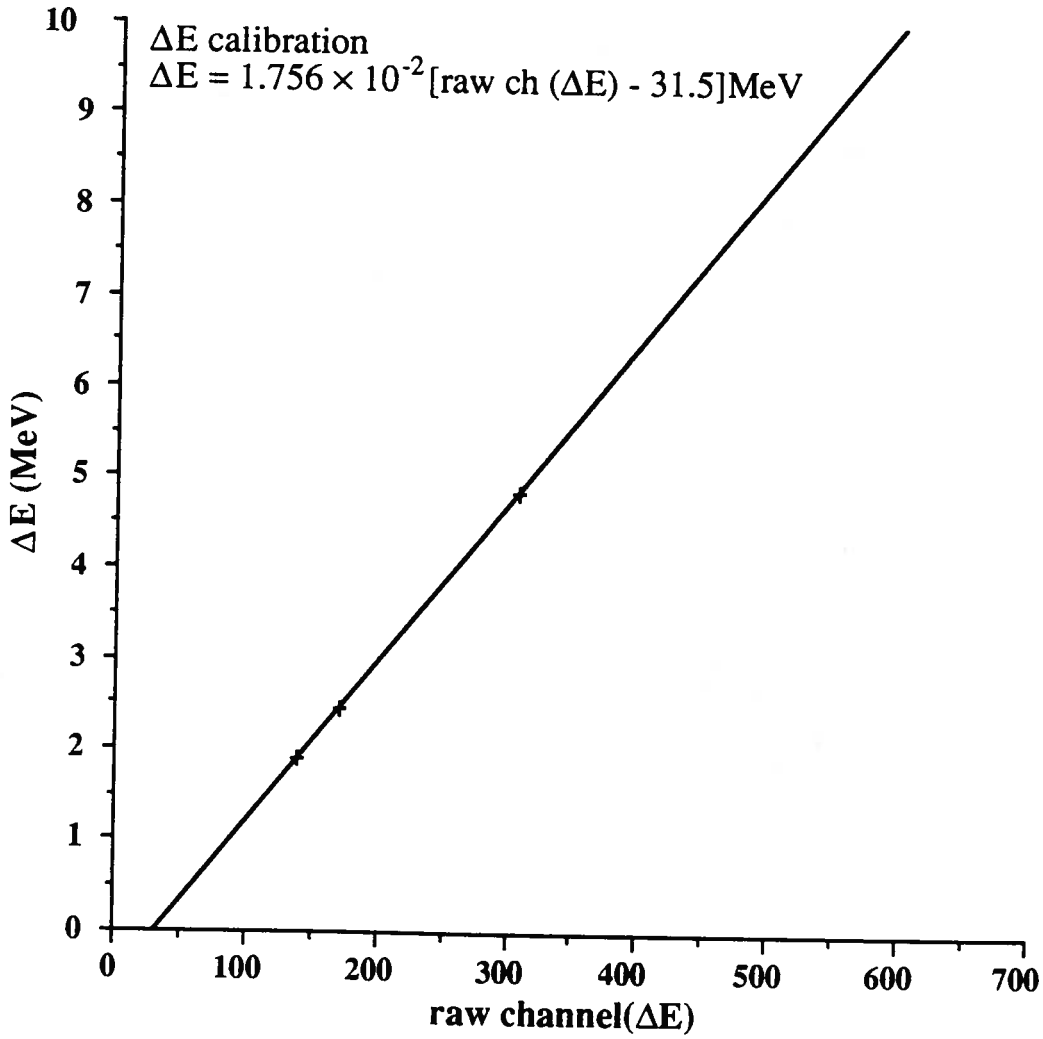

Fig. 2.13 $\Delta E - raw\ ch\ (\Delta E)$ calibration curve for the ΔE detector.

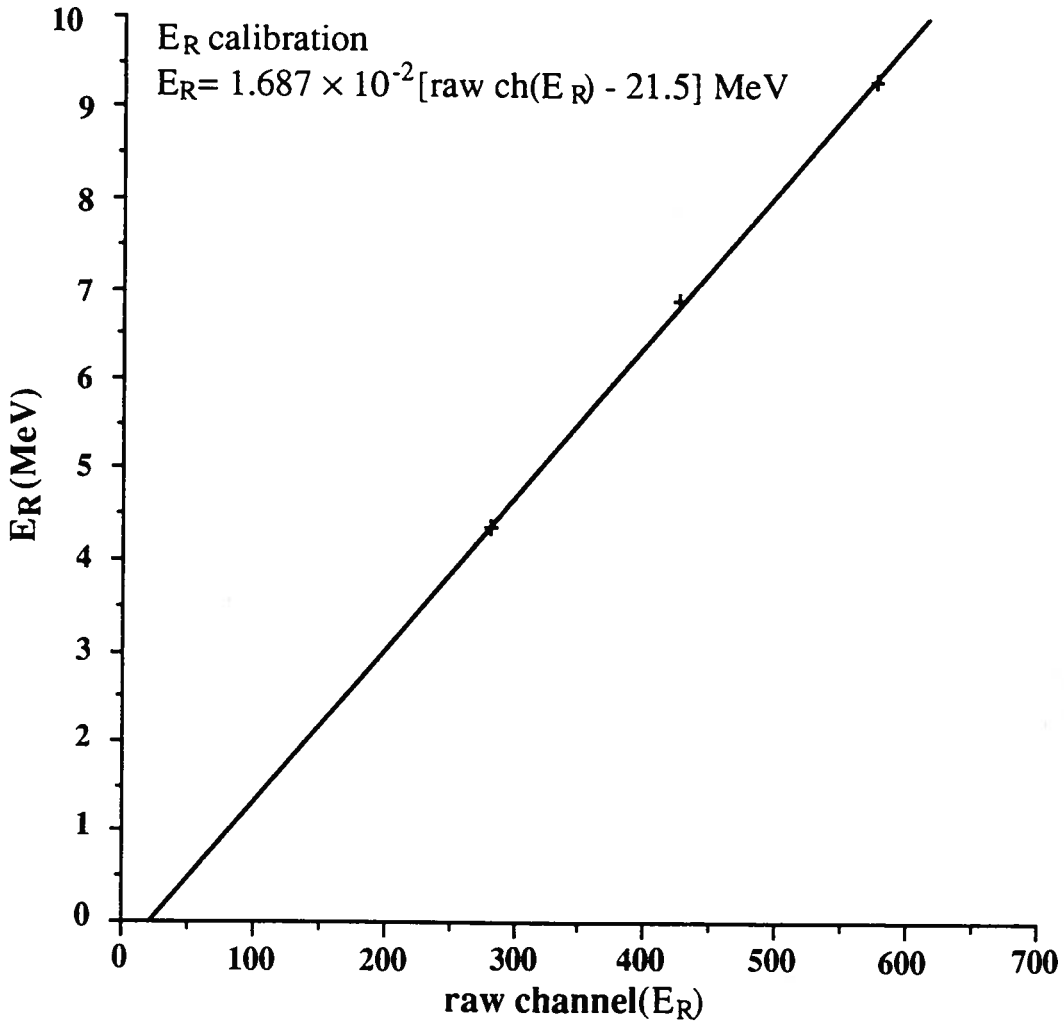

Fig. 2.14 $E_R - raw\ ch\ (E_R)$ calibration curve for the E_R detector.

recorded by data tapes, not scaled). The relations $\Delta E - raw\ ch(\Delta E)$ and $E_R - raw\ ch(E_R)$ are plotted in Figs. 2.13 and 2.14. The curves are straight lines described by

$$\Delta E = [raw\ ch(\Delta E) - 31.5]/57.0\ \text{MeV}, \qquad (2-17)$$

$$E_R = [raw\ ch(E_R) - 21.5]/59.2\ \text{MeV}. \qquad (2-18)$$

The total energy E_T is simply the sum

$$E_T = \Delta E + E_R \qquad (2-19)$$

It is practical to multiply the equations by a scaling factor 100 ch/MeV to get channel numbers:

$$ch(\Delta E) = 1.756[raw\ ch(\Delta E) - 31.5], \qquad (2-20)$$

$$ch(E_R) = 1.687[raw\ ch(E_R) - 21.5], \qquad (2-21)$$

$$ch(E_T) = ch(\Delta E) + ch(E_R), \qquad (2-22)$$

where the channel number $ch(\Delta E)$, when divided by 100, is the value of ΔE in MeV, etc.

Table 2.6. Input data for energy calibrations

Particle type	α		^{7}Li
Known E_T (MeV)	6.78	8.78	14.13
Known ΔE (MeV)	2.43	1.90	4.82
raw ch (ΔE)	171	139	306
Known E_R (MeV)	4.35	6.88	9.31
raw ch (E_R)	281	426	575
k (MeV^2)	1.01		1.08

The E_{coinc} detector in the back chamber was also calibrated in the same way.

It should be noted that the effects of pulse height defect and dead layers of the detectors have been eliminated, at least for $Z \doteq 3$, since the calibration curves map the energies and channel numbers on a one-to-one basis.

Besides providing data for energy calibrations, the ^{228}Th α-source and the scattered ^{7}Li beam also provide information for particle identification, in that they determine the k value in the formula

$$\Delta E \cdot E_T \approx kMZ^2 \qquad (2-23)$$

where k is nearly independent of M, Z and E_T.

The ^{7}Li peak, which is very sharp and hence has very well defined ΔE and E_T, forms a very small spot in the $\Delta E - E_T$ spectrum (Fig. 2.11). This spot defines a very precise k value

$$k(^{7}\mathrm{Li}) = \frac{\Delta E \cdot E_T}{MZ^2} = 1.08 \text{ MeV}^2 \qquad (2-24)$$

and a hyperbola

$$\Delta E \cdot E_T = 68.2 \text{ MeV}^2, \text{ for } ^{7}\mathrm{Li}, \qquad (2-25)$$

The significance of Eq. (2-25) is that it predicts that all particles that appear on the hyperbolic band are ^{7}Li ions, no matter what E_T they may have (as long as $E_T > \Delta E$, i.e. $E_R > 0$).

Since k is nearly constant, the value $k(^{7}\mathrm{Li})$ also helps to identify other types of particles through the relation

$$\Delta E \cdot E_T = k(^{7}\mathrm{Li})M(X)Z(X)^2 \text{ for particle X}, \qquad (2-26)$$

where X is any particle with MZ^2 not too far away from that of ^{7}Li. For example,

based on Eq. (2-26),

$$\Delta E \cdot E_T = 78.0 \text{ MeV}^2, \text{ for } ^8\text{Li} \qquad (2-27)$$

$$\Delta E \cdot E_T = 155.7 \text{ MeV}^2, \text{ for } ^9\text{Be} \qquad (2-28)$$

The k value determined by the ^{228}Th α-source is

$$k(\alpha) = 1.01 \approx k(^7\text{Li}). \qquad (2-29)$$

$k(\alpha)$ is different from $k(^7\text{Li})$ due to the large difference in MZ^2. Thus, $k(\alpha)$ should be used for particles with MZ^2 close to that of α-particles, such as ^{3}He and ^{6}He.

2.10 Position Calibration

Channel numbers for coordinates x and y are constructed according to

$$ch(x) = \frac{E(right) - E(left)}{E(right) + E(left)} \times 1024 + 1024, \qquad (2-30)$$

$$ch(y) = \frac{E(up) - E(down)}{E(up) + E(down)} \times 1024 + 1024, \qquad (2-31)$$

where (x, y) represent the particle's position of incidence relative to the center of the grid as viewed from the back (Fig. 2.15). According to the last two equations, if a particle hits the center of the $E_R - xy$ detector, $ch(x) = ch(y) = 1024$.

For position calibration, the grid of the rotatable aperture (Fig. 2.6) is placed in front of the detector telescope. Particles scattered by the second target or α-particles from the ^{228}Th source at the target position go through the holes and reach the $E_R - xy$ detector to form an image of the grid pattern (Fig. 2.16). The holes in the grid are evenly spaced and the separation between any two columns of holes is 0.1". The fact that the images of the same column have nearly the same

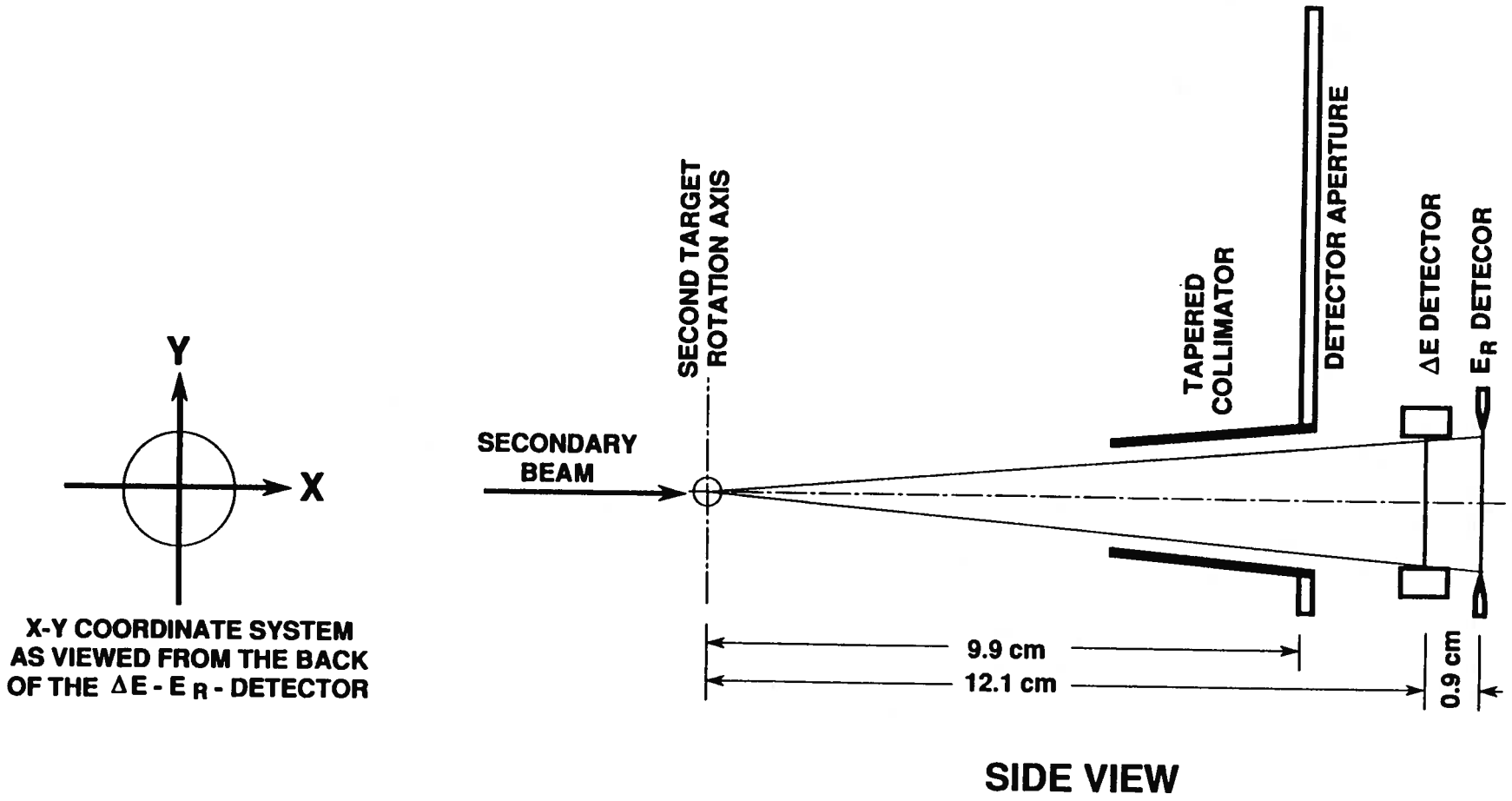

Fig. 2.15 The xy coordinate system and the configuration of the aperture and detectors.

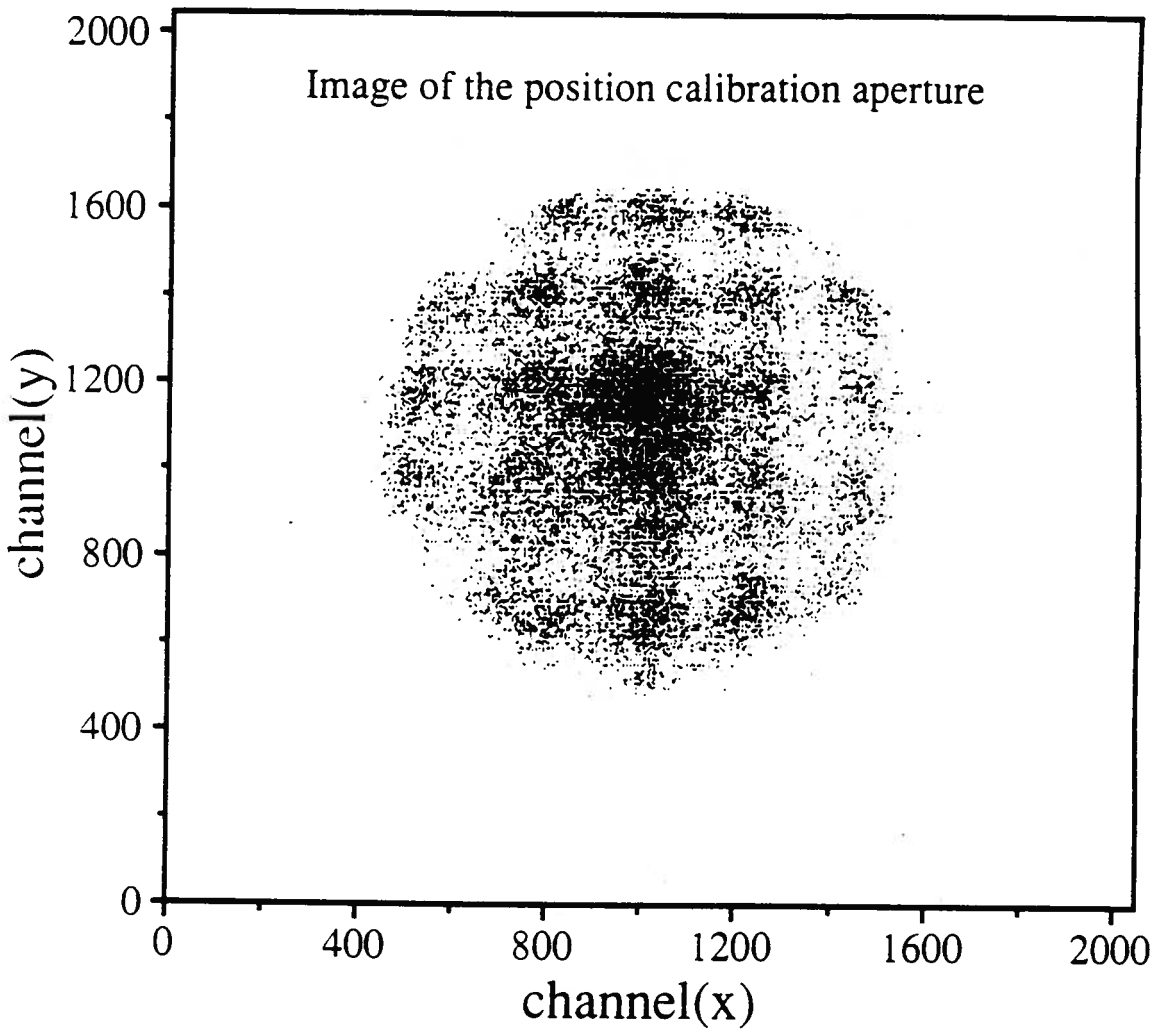

Fig. 2.16 Image of the position calibration grid.

x coordinate shows that the imaging of the data acquisition system is fairly linear. A set of (x, ch) is given in Table 2.7 and the position-channel relation is plotted in Fig. 2.17. The curve is described by a linear equation

$$x = (4.22 \times 10^{-4} ch - 0.416) \text{ inch} \qquad (2-32)$$

or

$$x = (1.07 \times 10^{-2} ch - 10.57) \text{ mm} \qquad (2-33)$$

Extraction of x coordinates from recorded channel numbers is done through these equations.

Table 2.7 Input data for position calibrations

ch number	507	752	997	1221	1457
x (inch)	-0.2"	-0.1"	0"	0.1"	0.2"

Since the ΔE detector is smaller than the $E_R - xy$ detector, the effective detection area of the detector telescope is defined by the ΔE detector. For solid angle calculations, the ΔE area is projected onto the front surface of the rotatable aperture and divided into small vertical strips. The area ΔS of a strip with edge coordinates X_1 and X_2 is

$$\Delta S = \int_{X_1}^{X_2} \sqrt{R^2 - X^2} dX, \qquad (2-34)$$

where $R = 13.1$ mm is the radius of the projection of the ΔE detection area. The solid angle $\Delta\Omega$ subtended by such strip is then

$$\Delta\Omega \approx \frac{\Delta S}{l^2} \qquad (2-35)$$

where $l = 99.4$mm is the distance of the grid front surface from the second target rotation axis (Fig. 2.15).

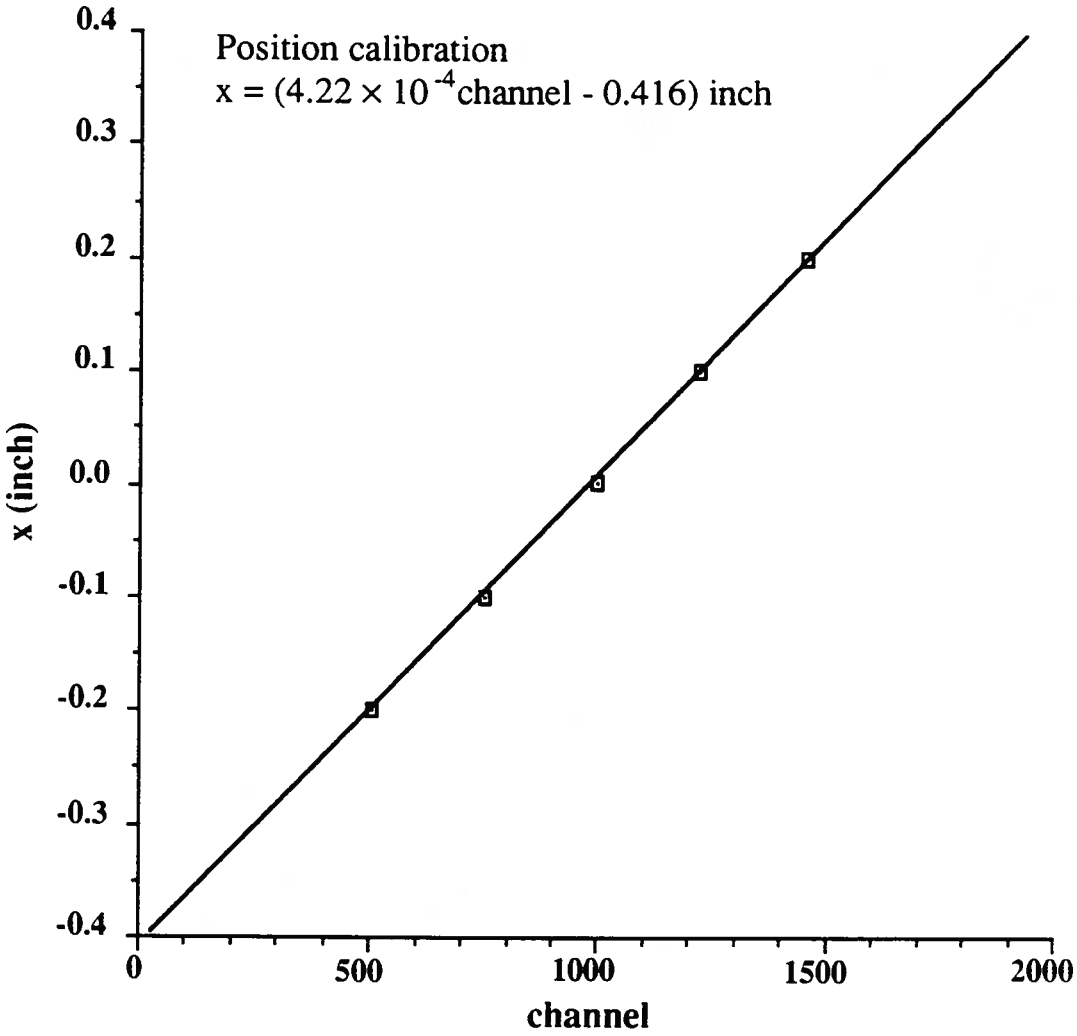

Fig. 2.17 Position calibration curve.

The scattering angle θ, of the detected reaction product (Fig. 2.5), is given by

$$\theta = \theta_o + arctan\left(\frac{x}{l}\right) \qquad (2-36)$$

where θ_o is the angle at which the $\Delta E - E_R$ detector is centered.

The electronic signals are stored via a CAMAC computer interface to the University of Notre Dame Perkin-Elmer model 3220 minicomputer. Individual events are recorded on magnetic tape using the data organization program, HAC. The tapes are brought back to the University of Michigan and analyzed on the Nuclear group's DEC Microvax II/GPX computer using the program LISA.

Footnotes to Chapter 2

[1]Intermagnetic General Corporation, Guilderland, NY, Model 31010.

[2]ORTEC, Inc., Model TD-075-200-20.

[3]J. Walton, Nuclear Chemistry Division, Lawrence Berkeley Laboratory, Berkeley, CA.

[4]Isotope Products Laboratories, 1800 N. Keystone Street, Burbank, CA 91504.

CHAPTER 3

PRODUCTION OF RADIOACTIVE ION BEAMS

3.1 Production of the ^{8}Li Beam

We have been able to successfully produce radioactive beams of ^{8}Li ($T\frac{1}{2}$ = 838 ms), ^{6}He ($T\frac{1}{2}$ = 806.7 ms) and ^{7}Be ($T\frac{1}{2}$ = 53.29d). Details of the production procedure and characteristics of the ^{8}Li beam will be given in this section since ^{8}Li was the most used beam in our experiments. ^{6}He and ^{7}Be beams will be briefly described in subsequent sections. Their production involved techniques similar to those for ^{8}Li.

The ^{8}Li beam was produced by bombarding a ^{9}Be target with a 17 MeV $^7Li^{+3}$ beam from the University of Notre Dame three-stage Van de Graaff accelerator.

Table 3.1. Production setup and characteristics of the ^{8}Li beam

Incident beam and energy	^{7}Li, 17 MeV
Production target and thickness	^{9}Be, 12.7 μm
Front aperture opening	5° - 11°
Back collimator dimensions	0.75" dia × 1.75" long
Solenoid focusing current	113 Amp
Conversion efficiency (^{7}Li to ^{8}Li)	1.61×10^{-7}
Production rate of ^{8}Li at 1 eμA $^7Li^{+3}$	3.4×10^5 ^{8}Li/sec
^{8}Li beam average energy	14.4 MeV
^{8}Li beam energy spread	650 keV FWHM
Half life of ^{8}Li	838 ms
Flight path of ^{8}Li	209.5 cm
Decay probability of ^{8}Li during flight	9.34×10^{-8}
Size of ^{8}Li beam at target	1 cm diameter
Purity of ^{8}Li beam	70%

The front aperture was $5° - 11°$. The ^{9}Be foil was 12.7 μm thick (or 2.29 mg/cm^2). The resulting ^{8}Li beam had an average energy of 14.4 MeV and an energy spread of 650 keV (Figs. 3.1 and 3.2). The production rate was 3.4×10^5 ^{8}Li/sec with a primary ^{7}Li beam of 1 eμA. Table 3.1 lists the characteristics of the ^{8}Li beam and more explanations are given below.

A. Choice of Nuclear Production Reaction

A ^{8}Li nucleus can be most easily created from the interaction of a ^{7}Li nucleus with a target nucleus through the one-neutron transfer reaction channel. Since ^{7}Li beams of high intensities are available from the accelerator, the remaining question is what should be used as the target.

There are two good candidate nuclear reactions to generate ^{8}Li:

$$^2\mathrm{H}(^7\mathrm{Li},^8\mathrm{Li})^1\mathrm{H}\ g.s.,\ Q = -0.191\ \mathrm{MeV}, \qquad (3-1)$$

$$^9\mathrm{Be}(^7\mathrm{Li},^8\mathrm{Li})^8\mathrm{Be}\ g.s.,\ Q = 0.368\ \mathrm{MeV}. \qquad (3-2)$$

The total cross sections of ^{2}H (^{7}Li, ^{8}Li) ^{1}H (McClenaham, 1975) and ^{9}Be (^{7}Li, ^{8}Li) ^{8}Be (Norbeck, 1959) at E (^{7}Li) $\approx$ 13 MeV are close to each other, both being of the order of 100 mb. But comparisons of other aspects favor the choice of ^{9}Be (^{7}Li, ^{8}Li) ^{8}Be g.s. Spectra obtained for the ^{7}Li + ^{9}Be reaction at E (^{7}Li) = 17 MeV are given in Appendix D.

First of all, the kinematic shifts of the two reactions are very different. These shifts affect the secondary ^{8}Li beam energy spread since the ^{8}Li ions must be collected over finite angular ranges to have reasonable beam intensities. Fig. A.2 (Appendix A) shows the angular dependence of ^{8}Li energies from the reactions. Over the range of 5° to 11°, the energy of ^{8}Li from reaction (3-1) decreases by 3.7 MeV, while the energy of ^{8}Li from reaction (3-2) only decreases by 0.5 MeV. As a

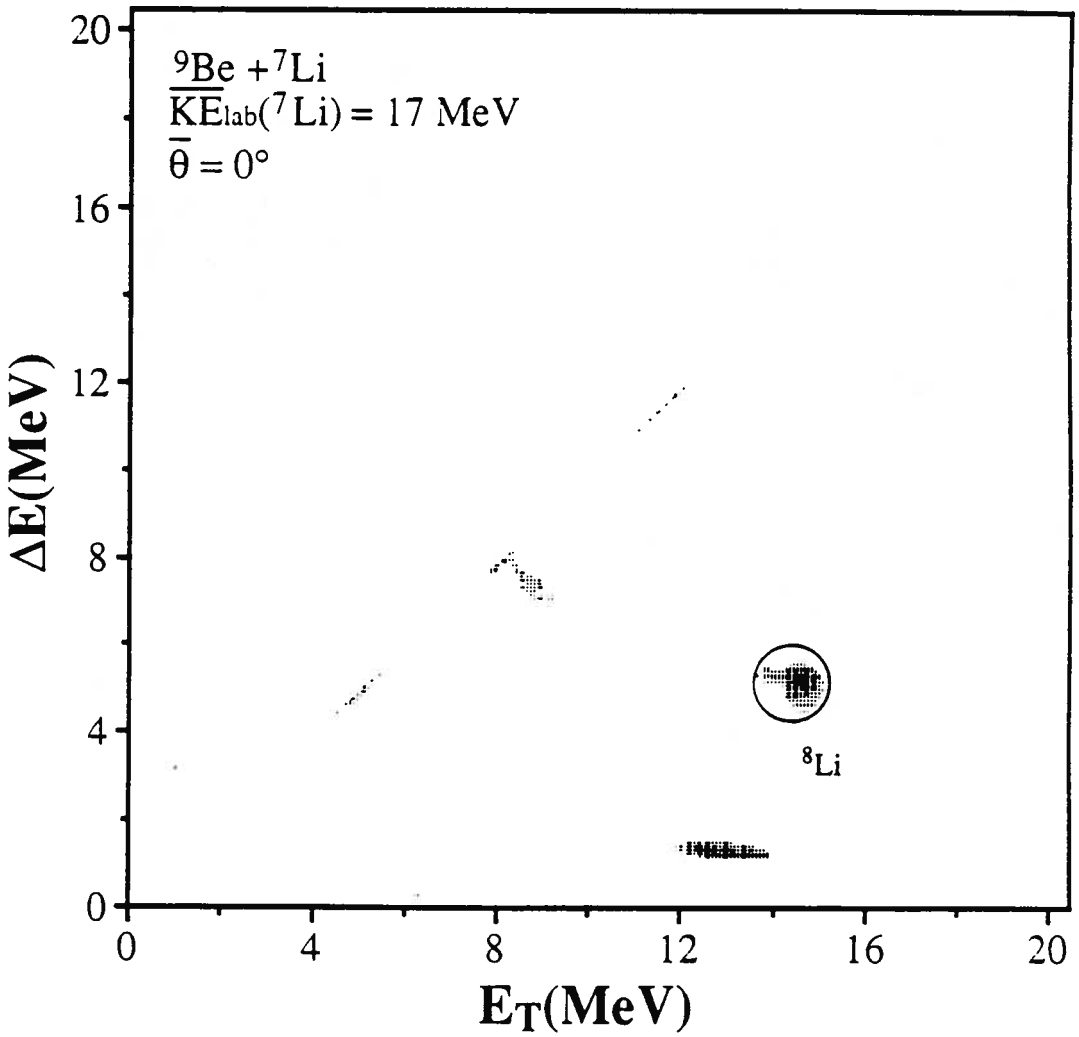

Fig. 3.1 $\Delta E - E_T$ spectrum of products from ^{9}Be + ^{7}Li reaction at $\overline{KE}_{lab}$ (^{7}Li) = 17 MeV at the solenoid focal plane.

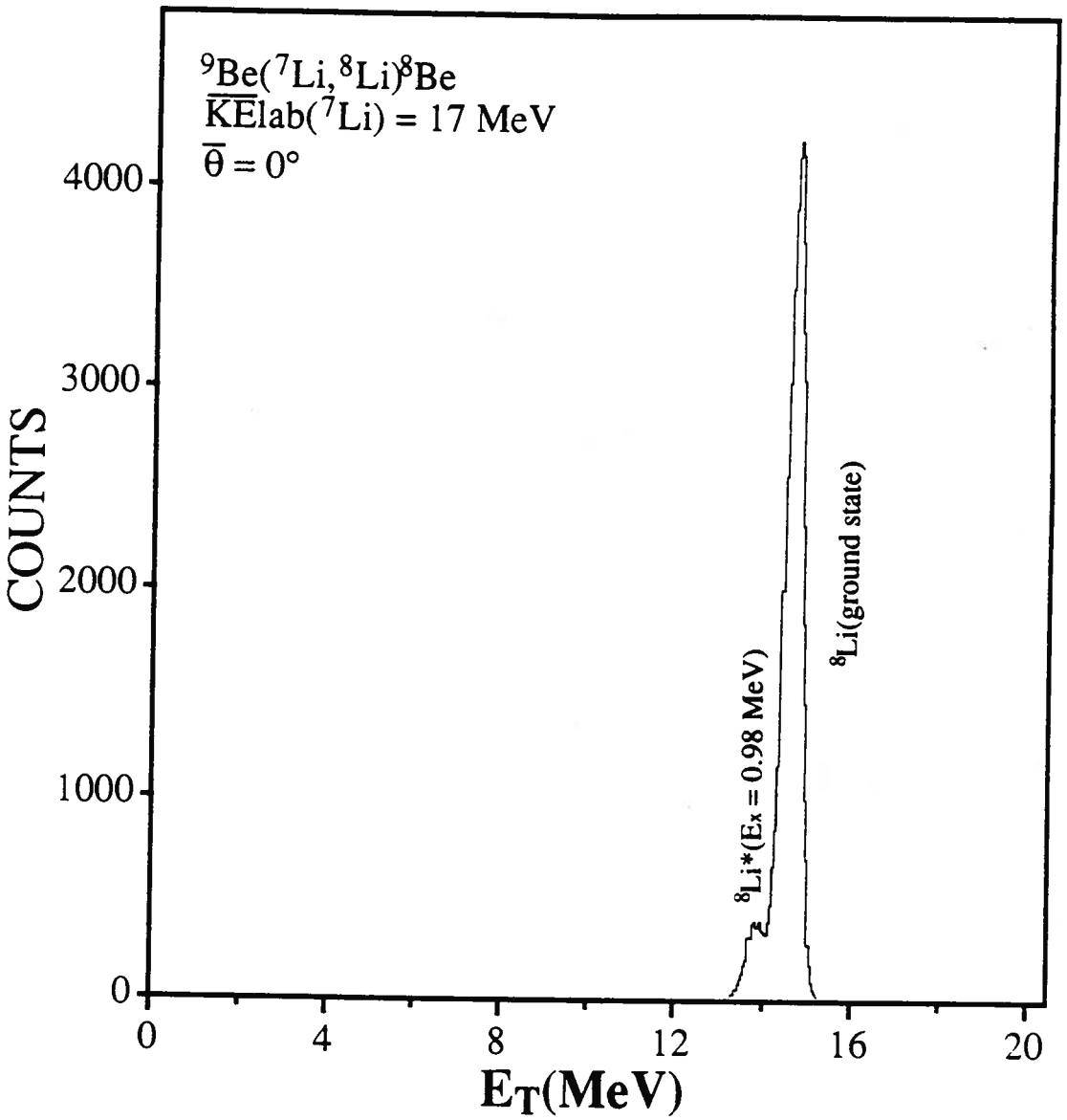

Fig. 3.2 E_T spectrum of the ^{8}Li beam.

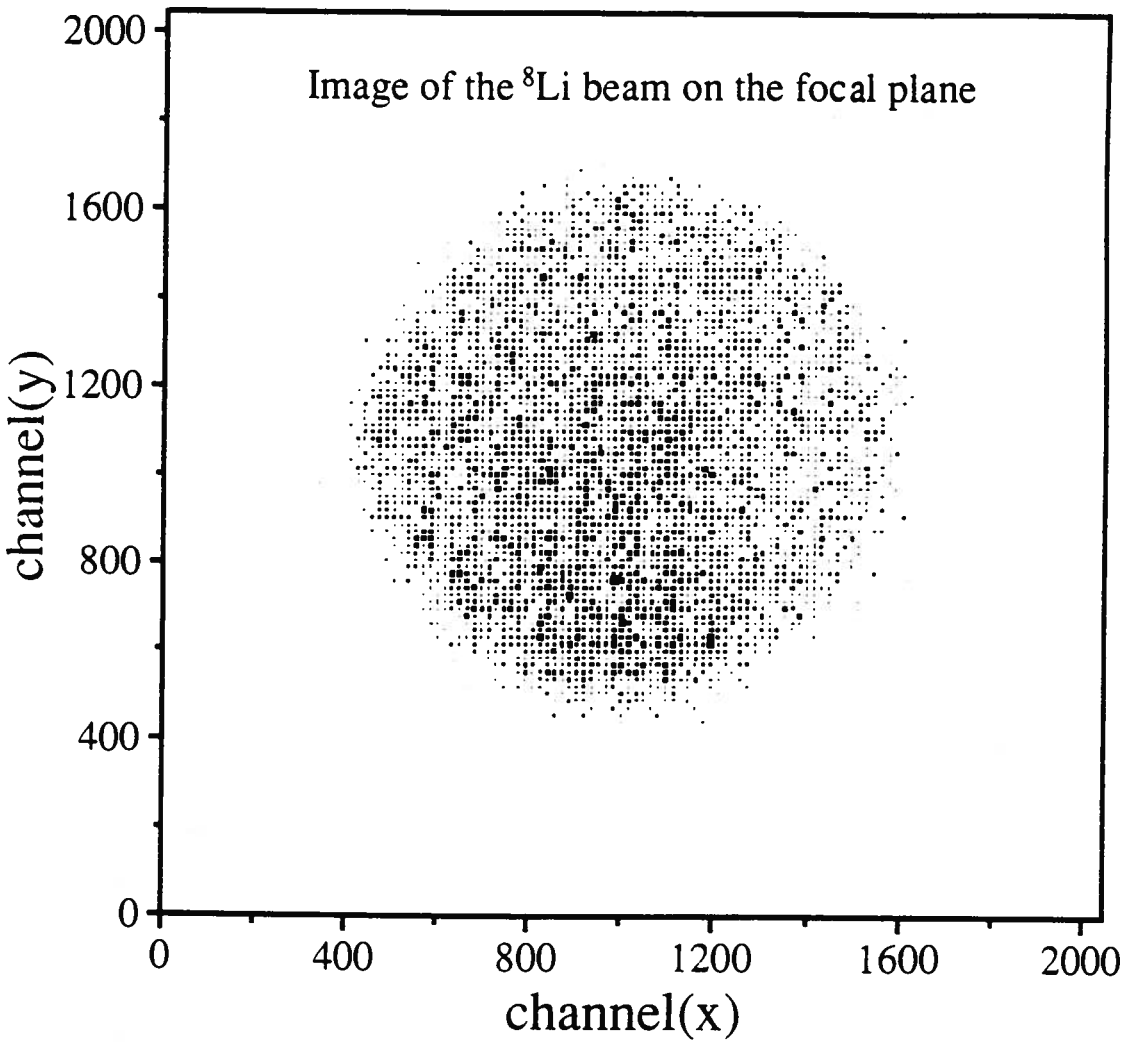

Fig. 3.3 Position spectrum of the ^{8}Li beam on the focal plane.

result, the energy resolution of the ^{8}Li beam from the reaction ^{9}Be(^{7}Li, ^{8}Li)^{8}Be is *much* better.

Secondarily, contamination must be considered. Pure ^{2}H (deuterium) foils do not exist, only foils of chemical compounds that contain ^{2}H are available. For the nuclear reaction (3-1), a CD_2 (deuterated polyethylene) foil is usually used (Boyd, 1988). Then the problem of contamination arises. ^{8}Li interacts with ^{2}H, but it also interacts with C to produce ^{8}Li of different energy or even different types of particles (^{6}Li, ^{6}He, ...). Even if the contaminant particles can be eliminated, the carbon in the foil increases energy losses and hence increases energy spreads. In contrast, very pure (99.8%) ^{9}Be foils are commercially available[1], and contamination can be mostly eliminated with a ^{9}Be target.

Thirdly, the heat conductivity and melting point of ^{9}Be is better than that of CD_2. Primary ^{7}Li beams are usually focused into point-like spots ($\sim$ 1 mm diameter). Such high fluxes of energetic ions often melt the targets. To avoid melting, a CD_2 target must be coated with metallic materials such as aluminum to improve its heat conductivity. Such coatings introduce further particle contamination and energy spread of the ^{8}Li beam. ^{9}Be itself is metallic with a higher melting temperature and the heat generated by the impinging of the intense primary beam is conducted to the target holder and then to the environment.

Fourthly, the difference in Q-value also favors the choice of ^{9}Be. The reaction ^{9}Be (^{7}Li, ^{8}Li) ^{8}Be has a positive Q-value (Q = 0.368 MeV) but ^{2}H (^{7}Li, ^{8}Li) ^{1}H has a negative one (Q = -0.191 MeV). The positive Q-value adds energy to the product ^{8}Li and makes it easier to separate ^{8}Li from ^{7}Li and other particles.

The comparisons discussed above lead us to adopt the reaction ^{9}Be (^{7}Li, ^{8}Li) ^{8}Be for our ^{8}Li beam production. From Figs. 3.1 and 3.2, three quantities important

to later data analysis are obtained:

$$\Delta E = 5.2 \text{ MeV}, \tag{3-3}$$

$$E_T = 14.4 \text{ MeV}, \tag{3-4}$$

$$\Delta E \cdot E_T = 75.0 \text{ MeV}^2, \tag{3-5}$$

where ΔE is the energy loss of the 14.4 MeV ^{8}Li in the ΔE detector. The last equation can be used for ^{8}Li identification since the product $\Delta E \cdot E_T$ remains nearly constant over a large range of energy.

B. Energy Spread of the ^{8}Li Beam

The energy spread of the ^{8}Li beam has four origins: the finite thickness of the ^{9}Be production target (12.7 μm), the finite angular range of collection (5° - 11°), the energy uncertainty of the primary beam of ^{7}Li, and the energy straggling in the target.

Table 3.2 Energies of ^{8}Li at four extreme configurations

	$\theta = 5°$	$\theta = 11°$	Difference
Point A	14.40 MeV	13.90 MeV	0.50 MeV
Point B	14.75 MeV	14.38 MeV	0.27 MeV
Difference	0.35 MeV	0.48 MeV	

As can be seen from Eq. (2-14), the energy loss is approximately proportional to the ion's mass. Accordingly, at the same energy, ^{8}Li will lose more energy than ^{7}Li does. So ^{8}Li ions can have various energies since the reaction ^{9}Be (^{7}Li, ^{8}Li) ^{8}Be can take place at any point between the front surface and the back surface of the target. Particularly, if the reaction takes place at point B (Fig. 3.4), the energy loss is minimal since ^{7}Li lose energy but ^{8}Li does not. If the reaction is at point A, the energy loss is maximal since now ^{8}Li is responsible for the total energy loss. The following lists the energies of ^{8}Li, corresponding to the two extremes, and the

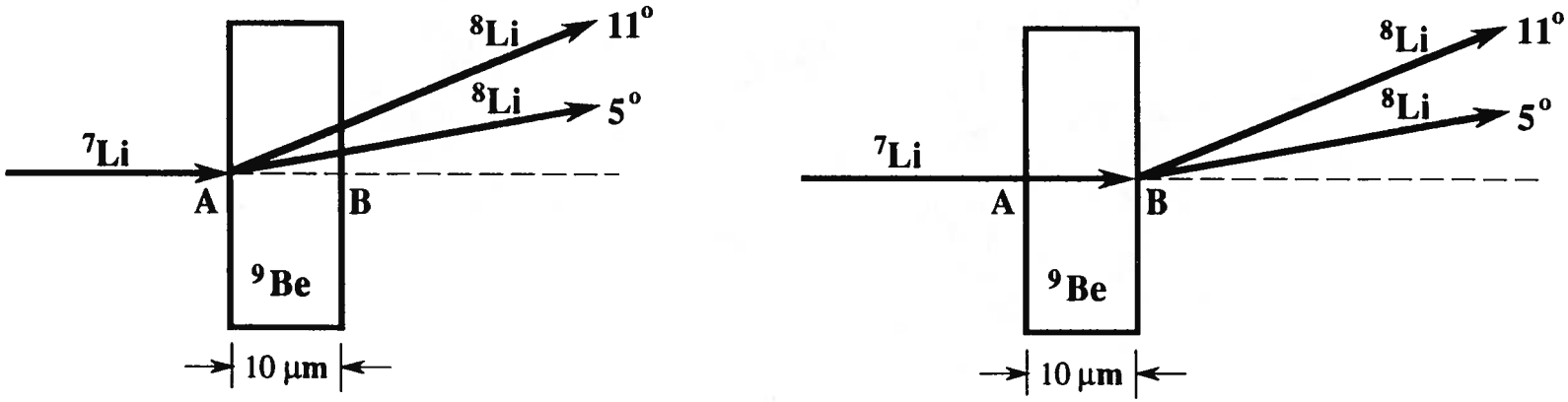

Fig. 3.4 Production of the ^{8}Li beam with finite target thickness and angular range.

spread at 11° (Table 3.2).

$$E(^8\mathrm{Li}) = 13.90 \text{ MeV, at point A,} \qquad (3-6)$$

$$E(^8\mathrm{Li}) = 14.38 \text{ MeV, at point B,} \qquad (3-7)$$

$$\delta E_1 = 0.48 \text{ MeV, at } \theta = 11°, \qquad (3-8)$$

where δE_1 stands for the energy spread resulting from the finite target-thickness.

The maximum acceptable δE_1 thus places a limit on the target thickness. A thick target produces more ^{8}Li ions but deteriorates the energy resolution. A thin target leads to a better resolution but does not produce an intense beam. In our experiments, a tradeoff between the energy resolution and beam intensity was made and a ^{9}Be foil of 12.7 μm was used. With this target, the production rate was 3.4 $\times$ 10^5 ^{8}Li ions/sec at 1 $e\mu A$ of $^7\mathrm{Li}^{+3}$. This rate is high enough for many cross section measurements and the spread $\delta E_1 = 0.48$ MeV is tolerable.

Another major source of energy spread is the kinematic shift effect. Details are discussed in Appendix A. Due to this effect, ^{8}Li ions ejected at different angles also have very different energies. As an example, two extreme energies of ^{8}Li corresponding to the two extreme angles (5° and 11°) and the energy spread δE_2 have the following values (Table 3.2).

$$E(^8\mathrm{Li}) = 14.40 \text{ MeV, at } \theta = 5° \qquad (3-9)$$

$$E(^8\mathrm{Li}) = 13.90 \text{ MeV, at } \theta = 11° \qquad (3-10)$$

$$\delta E_2 = 0.50 \text{ MeV, at point A} \qquad (3-11).$$

The third source of energy spread is the primary ^{7}Li beam energy spread δE_3.

It is small and negligible:

$$\delta E_3 = 0.01 \text{ MeV}. \qquad (3-12)$$

If we think of δE_1, δE_2, δE_3 as being independent, the total spread of the ^{8}Li beam is

$$\delta E = [(\delta E_1)^2 + (\delta E_2)^2 + (\delta E_3)^2]^{\frac{1}{2}} = 0.70 \text{ MeV}. \qquad (3-13)$$

This is the energy spread immediately behind the first target.

The energy spread measured by the $\Delta E - E_R$ detector at the point behind the second target, as represented by the FWHM of the energy peak in Fig. 3.2, is 0.65 keV, which is very close to the spread δE in Eq. (3-13). This near equality implies that the solenoid has effectively transmitted almost all the ^{8}Li ions produced at the first target to the second target position, and that the back collimator was not too small to cut down the number of ^{8}Li ions. On the other hand, the 70% purity of ^{8}Li beam (Table 3.1) implies that the collimator was not too big to allow many unwanted ions to pass.

The energy of the ^{8}Li beam ranges from 13.90 MeV to 14.75 MeV immediately behind the first target (Table 3.2). When the reaction takes place at point A and the ^{8}Li comes out at 11°, maximum energy loss and kinematic shift occur and the lower limit of beam energy is reached. The upper limit is reached when the reaction takes place at point B and the ^{8}Li energies at 5°, since then the energy loss and kinematic shift are both minimal. The average energy of the ^{8}Li beam is

$$E(^8\text{Li}) = 14.4 \text{ MeV} \qquad (3-14)$$

This is also shown in Fig. 3.2 (1 MeV/100 ch).

C. Focusing of the ^{8}Li Beam

C. Focusing of the ^{8}Li Beam

The ^{8}Li beam produced has an average energy of 14.4 MeV. To find the optimal solenoid current to focus this beam, the detector telescope was placed at 0°, i.e. aligned with the beam axis, and a rough estimate of current was made using Eq. (2-9). The beam image formed by the $\Delta E - E_R$ telescope was mapped to the CRT screen of the on-line computer. The solenoid current was then adjusted until a well-centered, smallest image spot was achieved. Fig. 3.3 shows a xy position spectrum of the ^{8}Li beam, i.e. an image as seen on the computer screen.

The current was then increased by 0.8% to focus the beam on the second target since the target was 12.1 cm forward of the detector (Fig. 2.6). The final current was 113 Amp (3.28 Tesla at the solenoid center). The ^{8}Li beam formed a spot of about 1 cm diameter, instead of a sharply focused point, on the second target, even when it was optimally focused. This is not surprising for two reasons. First, the beam was not procured at a single angle in an infinitesimally thin target. Rather, the ions in the beam came out of the target at angles between 5° and 11°, and hence their energies varied. Second, the solenoid focusing system had non-vanishing momentum dispersion, linear magnification and spherical aberration (Hawkes, 1982; Jiye, 1986).

The solenoid momentum dispersion can be evaluated with the help of the Gaussian focal length

$$f = \frac{4(B\rho)^2}{(\overline{B_z^2 L})} = \frac{4p^2}{q^2(\overline{B_z^2 L})},$$

whose derivative with respect to momentum p is

$$\frac{df}{dp} = \frac{8p}{q^2(\overline{B_z^2 L})}.$$

Since the position of the focal point z is related to f through equations

$$\frac{1}{d_{obj}} + \frac{1}{d_{ima}} = \frac{1}{f},$$

and

$$d_{obj} + d_{ima} = z,$$

and since $dp \neq 0$ at any angle, the derivative gives rise to the axial momentum dispersion dz/dp and radial (transverse) momentum dispersion dr/dp, which are related by

$$\frac{dr}{dp} = \frac{dz}{dp} \cdot M_\theta \cdot \theta,$$

where M_θ is the angular magnification and θ is the emerging angle in radian. Numerically, these dispersions are (Appendix B)

$$\Delta z/(\Delta p/p) = 2.7 \text{ cm}/\%,$$

$$\Delta r/(\Delta p/p) = 0.12 \text{ cm}/\%,$$

for particles at 7.5° angle and around 15 MeV energy, provided the focusing current is 113 Amp.

Therefore, a single solenoid cannot focus particles to the same point and a point image does not exist anywhere on the beam axis.

The linear magnification $M_L = -d_{obj}/d_{ima}$ also contribute to the image size of the ^{8}Li beam, though not significantly. In the configuration shown in Fig. 2.3, M_L = 157.2 cm/52.3 cm = −3.0. If the ^{7}Li beam spot size on the first target (object size) is 1 mm, then the ^{8}Li beam spot size on the second target (image size) is at least 3 mm, regardless of the momentum dispersion and spherical aberration effects.

The solenoid's spherical aberration is the most significant effect on the image size. The aberration occurs because of the non-paraxial nature of the ion trajectories. Particles emitted at a larger angle to the axis experience a larger radial deflection and thus cross the axis at a point closer to the solenoid than the paraxial

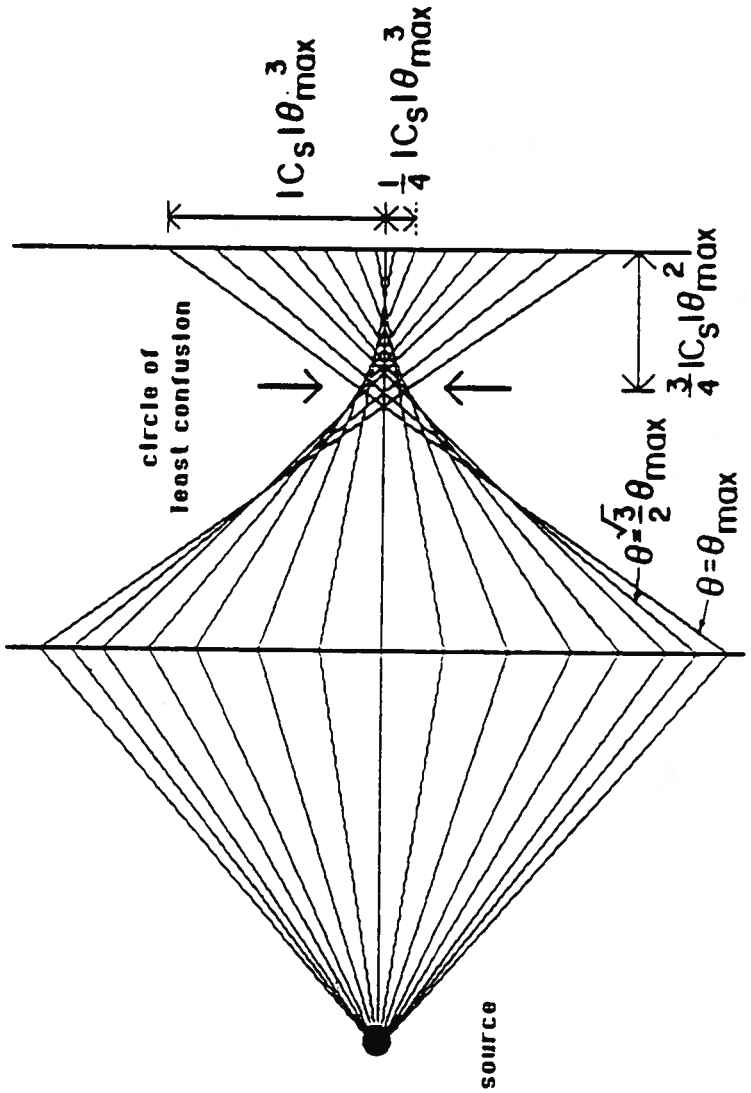

Fig. 3.5 Spherical aberration of the image of a point source (Stern, 1987).

focal point. As shown in Fig. 3.5 (Stern, 1987 and references cited therein), the image of a point source on the Gaussian focal plane is a fairly large disk instead of a point, but a smallest disk, called the circle of least confusion (clc), exists in front of the focal plane. The radius and the position of the circle, with respect to the focal plane, are given by

$$r_{clc} = \frac{1}{4}|C_s|\theta_{max}^3, \tag{3-15}$$

$$l_{clc} = \frac{3}{4}|C_s|\theta_{max}^2, \tag{3-16}$$

where θ_{max} is the maximum angle at which the particles are emitted and C_s is the spherical aberration constant given by

$$C_s = \frac{M_L}{12}\int_{z0}^{z_G}\left[16\left(\frac{B_{z0}}{2B\rho}\right)^4 + 5\frac{B_{Z_0}^{(1)}}{2B\rho} - \frac{B_{z0}B_{z0}^{(2)}}{(2B\rho)^2}\right] r_G^4(z)dz. \tag{3-17}$$

The quantity where M_L is the linear magnification, r_G is the Gaussian trajectory which corresponds to a particle emitted from the axis at $\theta = 45°$, and the integral is evaluated between the object plane and the Gaussian focal plane. It should be noted that both r_{clc} and l_{clc} are very sensitive to θ_{max}. Increasing θ_{max} in order to achieve larger solid angle for particle collection increases ρ_{clc} and l_{clc} drastically. Fig. B.3 shows that $\rho_{clc} = 0.85$ cm, if all $^8Li^{+3}$ ions are emitted in the range of 5° to 11° with energy 14.4 MeV.

A real radioactive beam usually has both energy and angular spreads. Momentum dispersion and spherical aberration then act together to form an image size greater than if any of them acts alone. Fig. 3.6 shows the imaging of a $^8Li^{+3}$ beam produced in a 12.7 μm ^9Be target bombarded by a 17 MeV ^7Li beam. This beam consists of all $^8Li^{+3}$ ions emitted in the range of 5° to 11°, corresponding to an energy range of 14.0 MeV to 14.7 MeV. The radius of the circle of least confusion

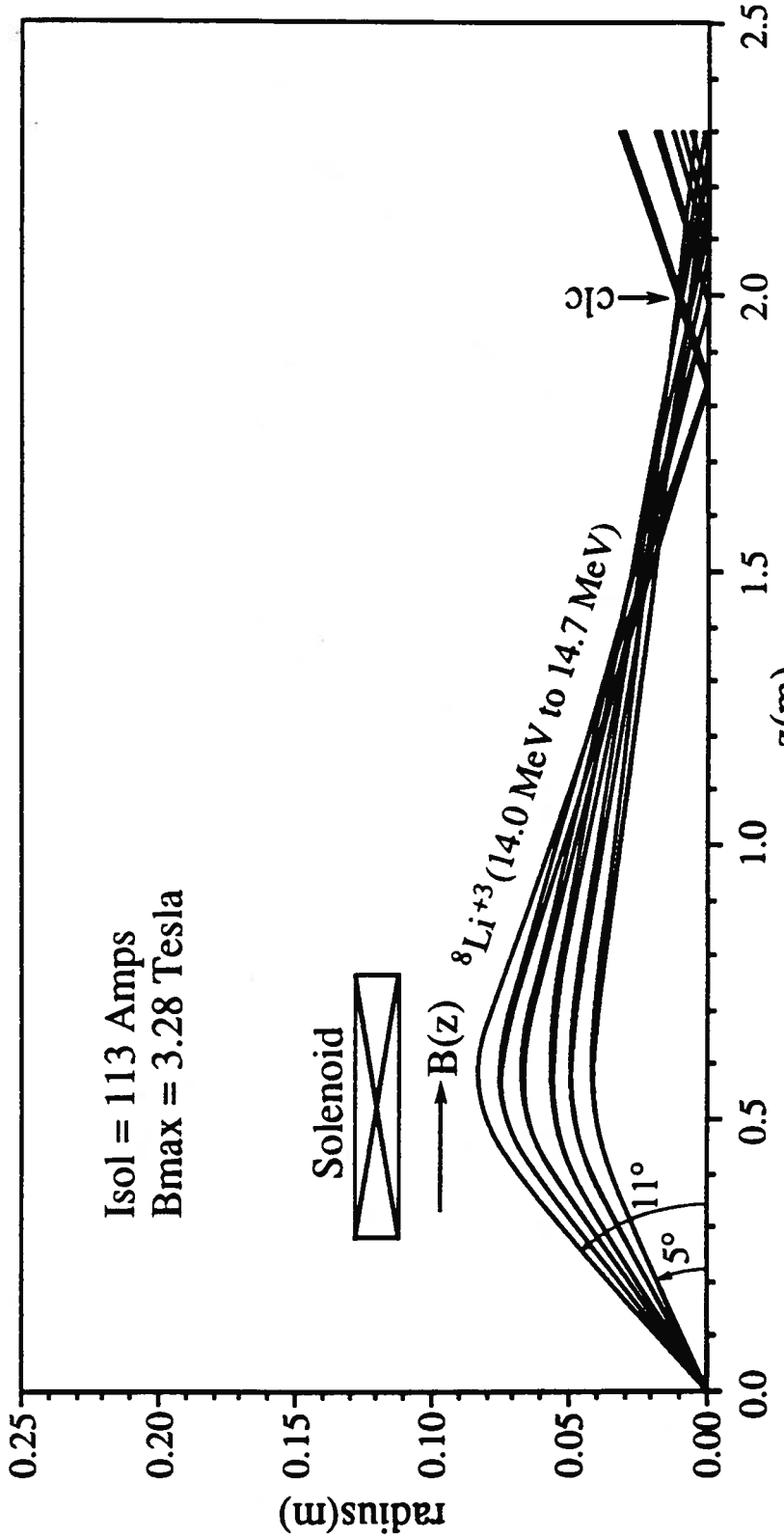

Fig. 3.6 Imaging of the ^{8}Li beam.

is $\rho_{clc} = 1.0$ cm. This image size is the joint effect of the momentum dispersion and spherical aberration.

Both momentum dispersion and spherical aberrations can be corrected by introducing defocusing devices such as electric dipoles or magnetic dipoles (Liu and Becchetti, 1989). Focusing of particles with much smaller images can then be achieved.

D. Purity of the ^{8}Li Beam and Production Rate

According to Eq. (2-11),

$$\frac{ME}{q^2} = 0.115 \times 10^{-3} I^2,$$

particles of the same $\frac{ME}{q^2}$ will be focused to the same point simultaneously. In the equation, M is the particle's mass in amu, E is the particle's energy in MeV, q is the particle's charge state, and ME/q^2 is proportional to the square of the particle's magnetic rigidity.

Table 3.3 Focused particles

Particle	Source reaction	Q (MeV)	M (amu)	q	$\bar{E}$ (MeV)	$\frac{M\bar{E}}{q^2}$
$^4H^{+2}$	$^7Li \rightarrow {}^4He + {}^3H$	2.468	4.003	2	13.0	13.0
$^6H^{+2}$	^9Be (^7Li, $^6He^*$)^{10}B	-7.187	6.109	2	8.6	12.9
$^6Li^{+2}$	^9Be(^7Li, ^6Li)^{10}Be	-0.438	6.015	2	8.5	12.7
$^8Li^{+3}$	^9Be(^7Li, ^8Li)^8Be	-0.368	8.022	3	14.4	12.8
$^9Be^{+3}$	^9Be(^7Li, ^7Li)^9Be	0	9.012	3	13.0	13.0
$^{11}B^{+4}$	^9Be(^7Li, ^5He)^{11}B	10.460	12.014	4	17.6	13.2

The focused $^8Li^{+3}$ beam had an average energy of 14.4 MeV and an energy spread of 0.65 MeV. This corresponds to a spread of ME/q^2, i.e.

$$\frac{ME}{q^2}(^8Li^{+3}) = 12.5 \text{ to } 13.1, \qquad (3-18)$$

where $M = 8.022$, q=3 and E=14.08 to 14.73.

Other contaminant particles such as ^{3}H, ^{4}He, ^{6}He, ^{7}Li, ^{9}Be and ^{11}B are also produced with continuous energies and hence continuous magnetic rigidities. Those with the right ME/q^2 are also focused together with $^{8}Li^{+3}$ ions.

Table 3.3 contains particles which could be produced in the ^{9}Be + ^{7}Li reaction and whose average ME/q^2 fell in the range in Eq. (3-18). All the listed particles actually reached the $\Delta E - E_R$ detector, but only three groups ($^{8}Li^{+3}$, $^{6}Li^{+2}$ and $^{4}He^{+2}$) were intense (Fig. 3.2). Among the focused particles, $^{6}He^{+2}$ ions were from the ^{6}He first excited state (1.80 MeV), while $^{6}Li^{+2}$, $^{9}Be^{+3}$, $^{11}B^{+4}$ ions were in charge states of +2, +3 and +4 respectively.

The contaminant particles amounted to 30% of the total ions collected by the detector. Thus, the purity of the ^{8}Li beam was 70%.

The contaminants cannot be eliminated by any combination of magnetic devices, since they will always have the same magnetic rigidity as that of $^{8}Li^{+3}$. However, adding proper electric devices like electric dipoles or coaxial cylinder lenses or energy absorbers can suppress the contamination and thus enhance the ^{8}Li beam purity.

The conversion efficiency is the ratio of the number of ^{8}Li ions produced to the number of ^{7}Li ions consumed. In our experiments, the efficiency was 1.61×10^{-7} ^{8}Li per ^{7}Li. When a 1 $e\mu A$ $^{7}Li^{+3}$ beam was used, ^{8}Li ions were produced at a rate of 3.4×10^{5} ^{8}Li/sec. From this efficiency, it can be deduced that the average differential cross section of the ^{9}Be (^{8}Li, ^{7}Li) ^{8}Be g.s. reaction is about 15 mb/sr in the range of 5° - 11°. Details of the production reaction are given in Appendix D.

E. Track Detector Imaging

A track detector, consisting of a piece of CRONAR plastic graphics film[2], was used to image $^{7}Li^{+3}$ from elastic scattering focused by the solenoid. Charged particles impinging on a solid foil cause radiolytic breaking of long polymer chains into

shorter fragments. These damaged regions are etched preferentially by chemicals and appear as distinct holes under a microscope. The film was placed near the focal point of the ions and was centered on the solenoid geometrical axis (Fig. 2.1). The film was then developed in a 6.25 N KOH solution (350 grams of KOH and 1 litre of distilled water) at 68°C for about 4 hours, forming a picture (white, cloudy) of the beam image visible to human eye. The picture was then digitized with a video camera connected to a computer.

Fig. 3.11 shows the picture (inversed) of the focused $^{7}Li^{+3}$ beam. The centroid of the beam was 2.5 mm below and 1.5 mm on the right of the geometrical beam, as seen along the beam direction. Using this information, the second target and the $\Delta E - E_R$ detector were accordingly placed off the geometrical axis.

3.2 Production of a ^{6}He Beam

A ^{6}He beam was produced with the same geometrical configuration for the ^{8}Li beam.

The production reaction was

$$^{9}\mathrm{Be}(^{7}\mathrm{Li},^{6}\mathrm{He})^{10}\mathrm{B}\ g.s.,\ \ Q = -5.387\ \mathrm{MeV}. \qquad (3-19)$$

The ^{7}Li beam energy was 14.63 MeV. The solenoid focusing current was 110 Amp, corresponding to a maximum magnetic field strength $B = 3.08$ Tesla at the solenoid center. The ^{6}He beam had an average energy of 8.2 MeV and energy spread of 0.78 MeV FWHM. Energy spectra are shown in Figs. 3.7 and 3.8.

The purity of ^{6}He beam was only 5% due to other particles such as ^{3}H, ^{4}He and ^{6,7}Li (Fig. 3.7) at the same magnetic rigidities. Electric focusing or defocusing devices or absorbers must be added for a higher purity ^{6}He beam.

Also, the conversion efficiency of ^{7}Li to ^{6}He was only 7.2×10^{-9}.

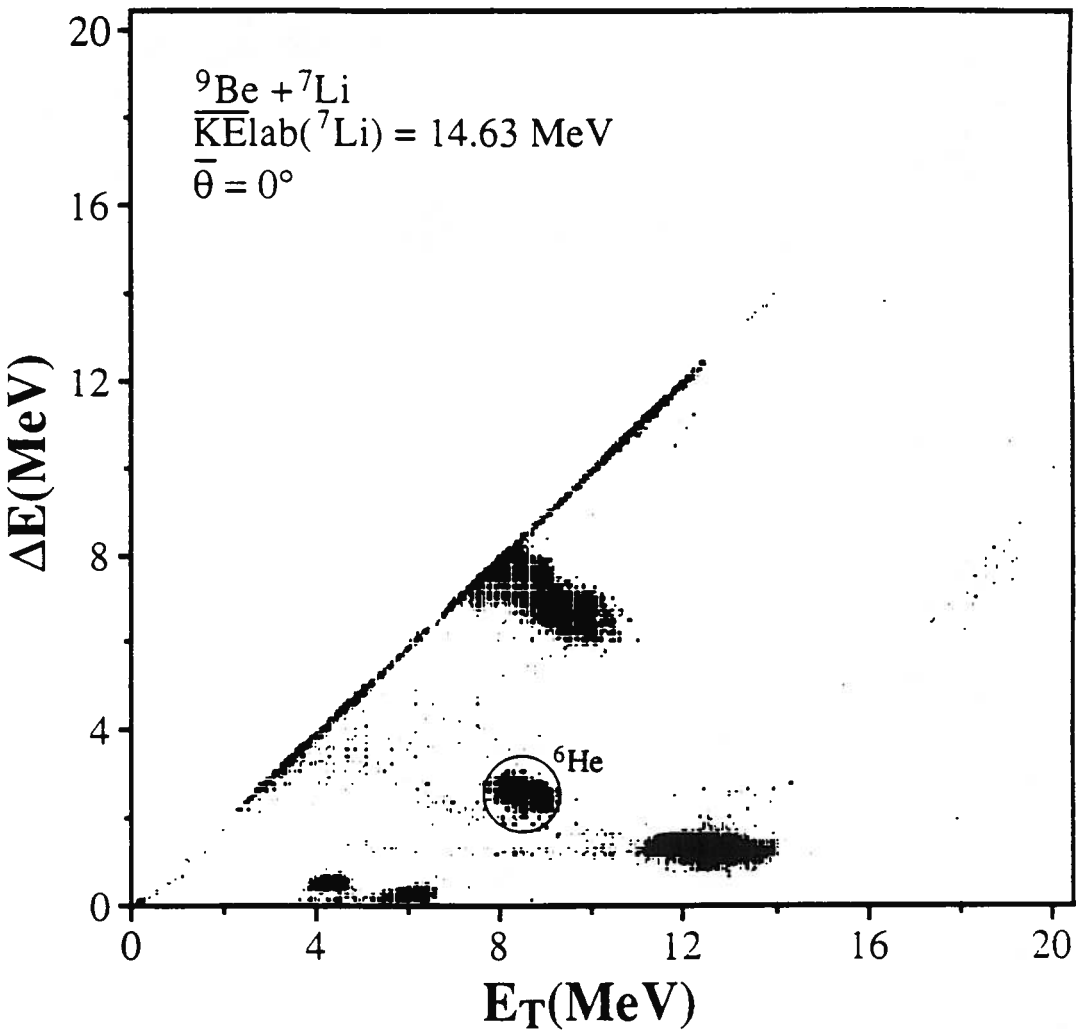

Fig. 3.7 $\Delta E - E_T$ spectrum of products from ^{9}Be + ^{7}Li reaction at $\overline{KE}_{lab}$ (^{7}Li) = 14.63 MeV.

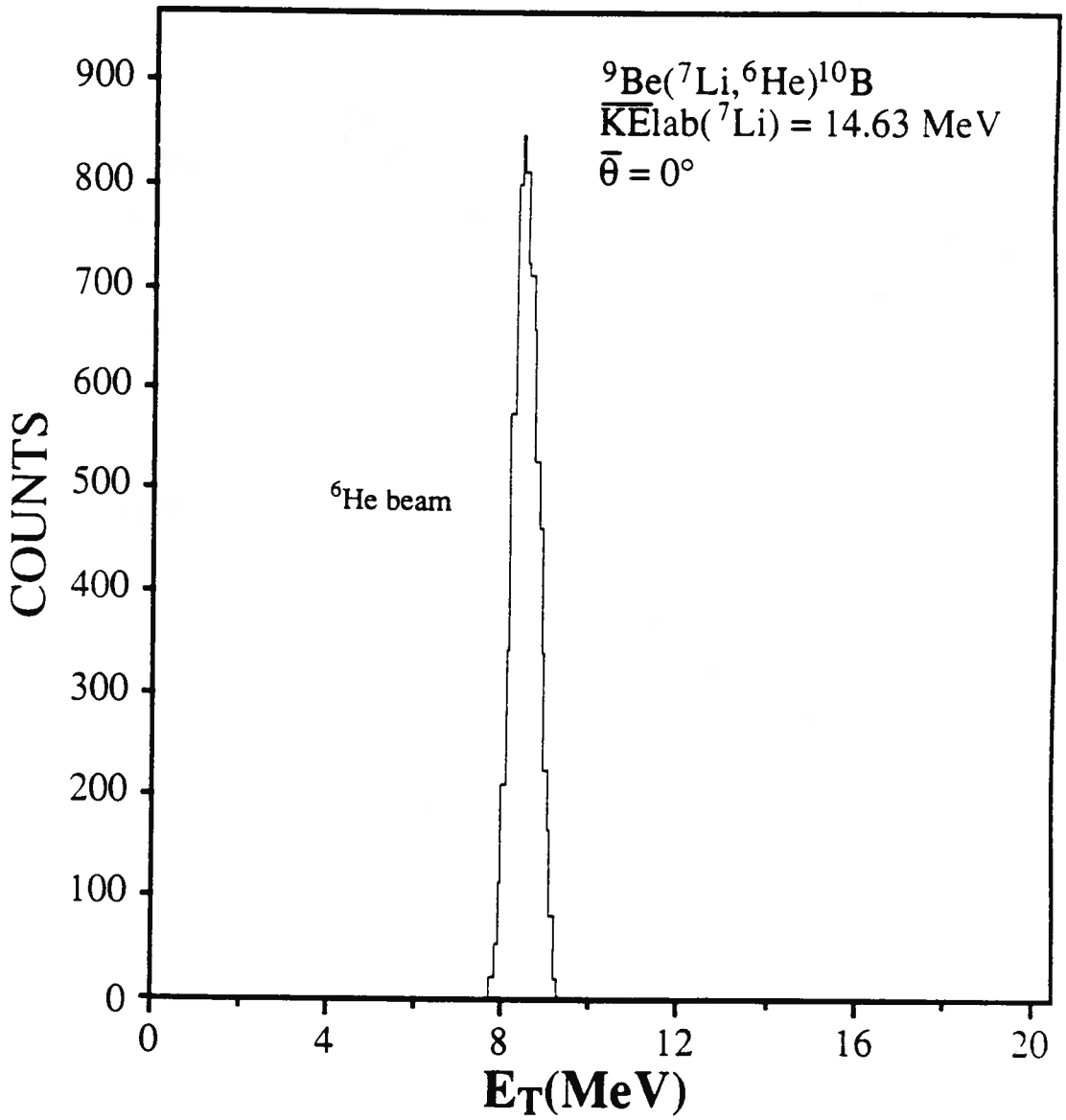

Fig. 3.8 E_T spectrum of the ^{6}He beam.

3.3 Production of a ^{7}Be Beam

The same geometrical setup for a ^{8}Li beam was also used to produce a ^{7}Be beam.

In addition, a ^{7}Be beam was made through the reaction

$$^1\mathrm{H}(^{10}\mathrm{B},^7\mathrm{Be})^4\mathrm{He},\ \ Q = 1.146\ \mathrm{MeV}. \qquad (3-20)$$

For this reaction, a 25.4 μm thick polyethylene (CH_2) foil was used as the production target together with a 26 MeV $^{10}B^{+4}$ beam. The focusing current was 88.5 Amp, or $B = 2.48$ Tesla at the solenoid center.

Fig. 3.9 shows the spectrum of all the reaction products collected by the $\Delta E - E_R$ detector ($\theta = 0°$) and Fig. 3.10 shows the spectrum of the gated ^{7}Be beam.

The reaction (3-20) suffered from large kinematic shift since the target ^{1}H is much lighter than the projectile ^{10}B (due to inverse kinematics). As a result, the ^{7}Be beam had a large energy spread, namely 1.1 MeV FWHM.

In contrast to its poor energy resolution, the ^{7}Be beam had very high purity (86%), mostly because $^7Be^{+4}$ had much higher magnetic rigidity than those of other lighter particles and separation was easy.

The ^{10}B to ^{7}Be conversion efficiency was 3.5×10^{-7}, partly because reaction (3-20) is a resonant reaction with a large cross section (Kolata, *et al.*, 1989b).

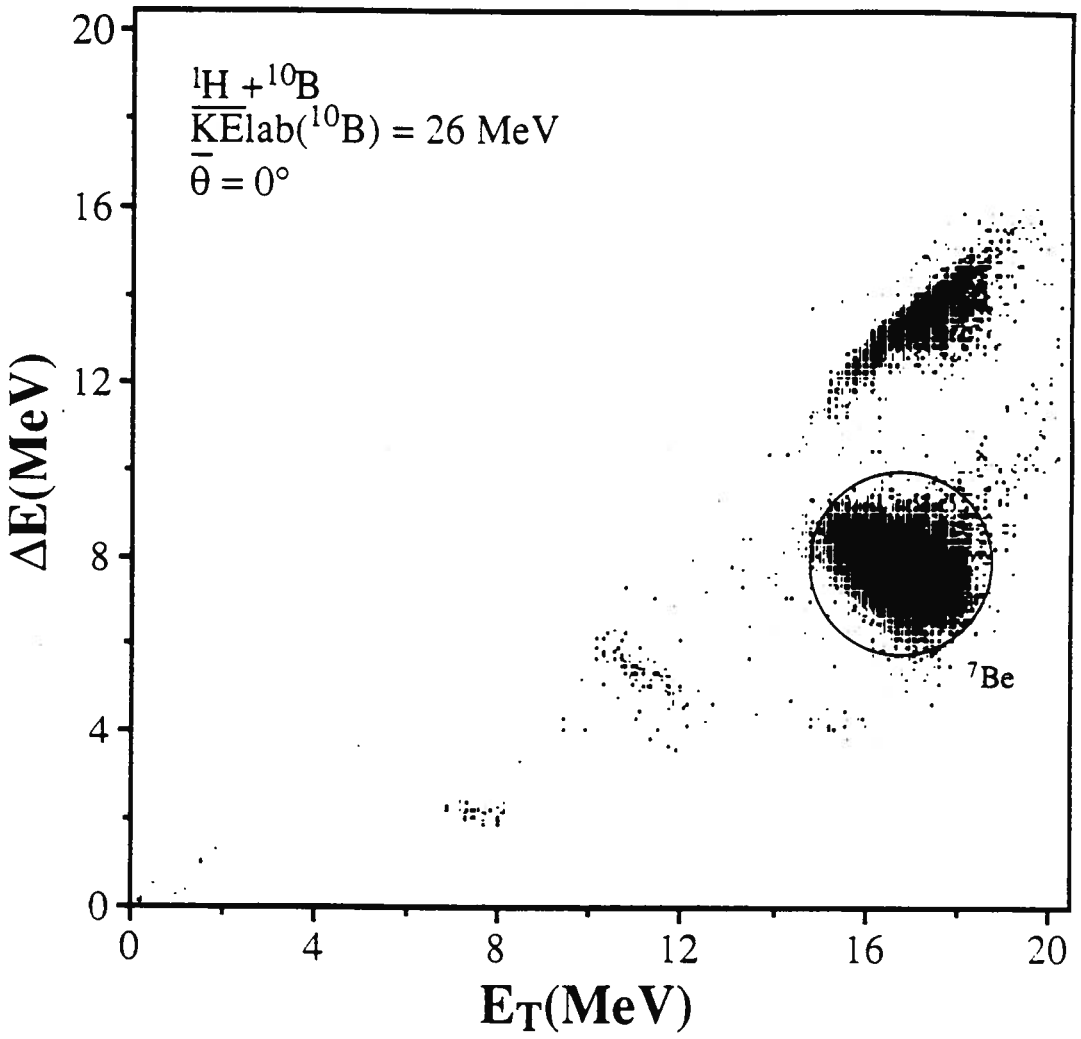

Fig. 3.9 $\Delta E - E_T$ spectrum of products from ^{1}H + ^{10}Be reaction at KE_{lab} (^{10}B) = 26 MeV at the solenoid focal plane.

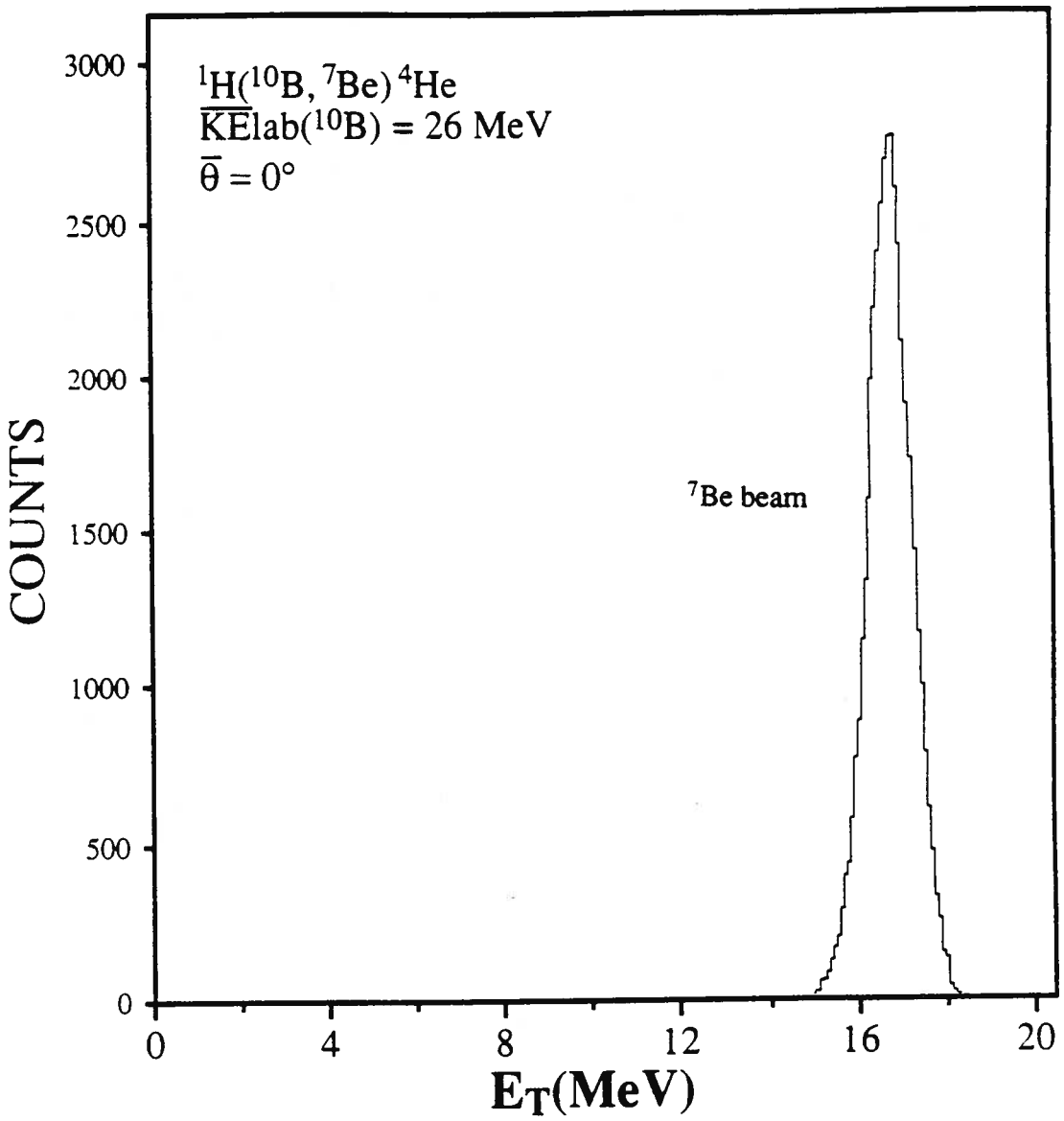

Fig. 3.10 E_T spectrum of the ^{7}Be beam.

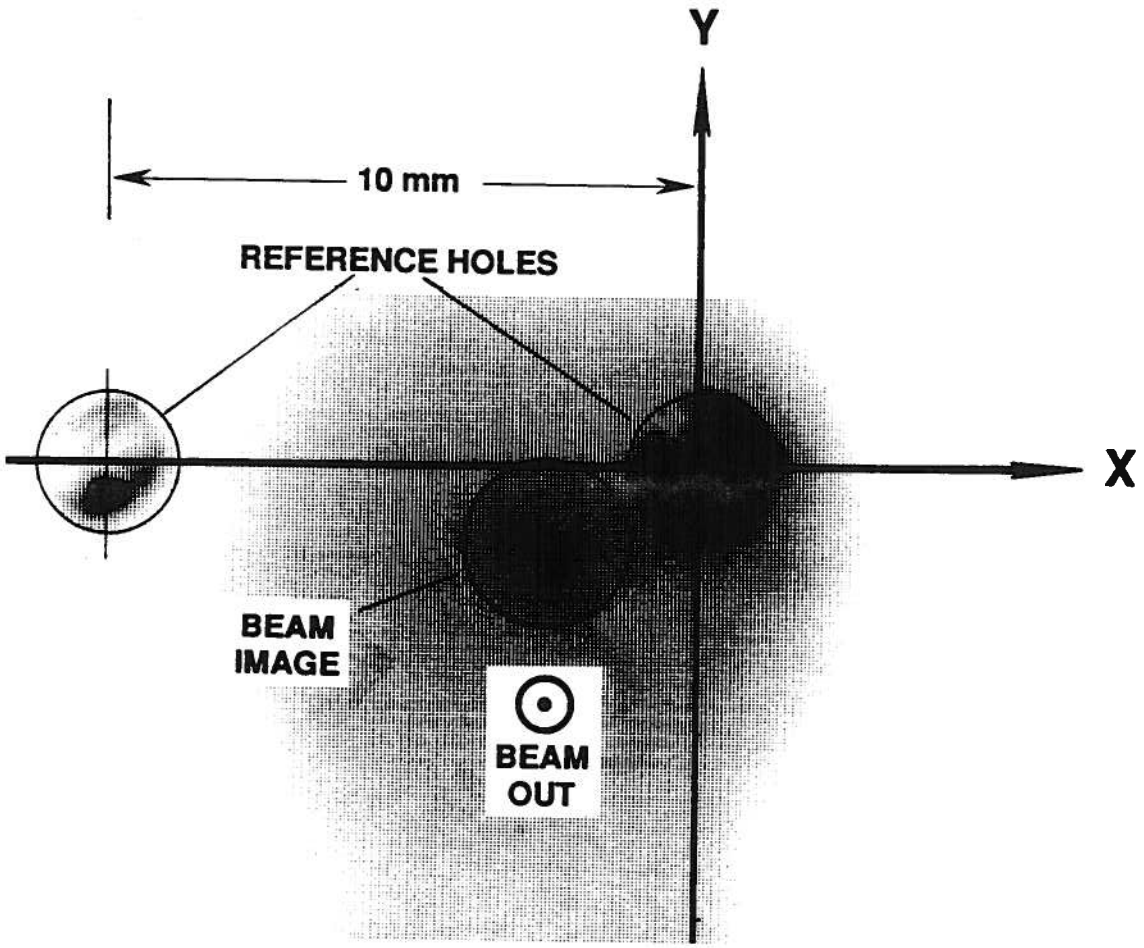

Fig. 3.11 Track detector image of focused, scattered $^{7}Li^{+3}$ ions.

Footnotes to Chapter 3

[1]LeBow Company, 5960 Mandarin Avenue, Goleta, California 93117.

[2]CRONAR unsensitized C42 0.1 mm graphics art film, Du Pont, Inc., Wilmington, DE.

CHAPTER 4

MEASUREMENT OF DIFFERENTIAL CROSS SECTIONS

4.1 Particle Identification

The purpose of our experiments is to measure differential cross sections for various nuclear reactions induced by radioactive ion beams. Since different types of particles are produced and will appear in the $\Delta E - E_T$ spectra, we need to know which particle groups are reaction products of interest.

A nucleus can be identified by its mass M and atomic number Z. To identify any events in the $\Delta E - E_T$ spectrum, we have to determine their M and Z values. Identification can be done with the help of equation

$$\Delta E \cdot E_T = kMZ^2, \qquad (4-1)$$

for the reasons stated below.

When an ion has energy greater than 1 MeV/nucleon, the probability that all its atomic electrons are stripped off when moving in solids is close to 1 (Marion, 1968). In our experiments, all ions involved had energies around 2 MeV/nucleon. When ions with such energies move in the 17.4 μm ΔE detector, most of them become naked nuclei. In other words, the charge states of most of the ions are equal to their atomic numbers, i.e. $q = Z$.

The correspondence between the pairs (M, Z) and the parabolas, called bands, defined by Eq. (4-1) is one to one for nuclei not far from stability. According to Eq. (4-1), for each Z value there is a family of bands corresponding to isotopes of the same Z. The bands within the family are separated by their masses, because M takes on only discrete values. Further, for the separation between two families, consider the ratio

$$R_{12} = \frac{(\Delta E \cdot E_T)_2}{(\Delta E \cdot E_t)_1} = \left(\frac{Z_2}{Z_1}\right)^2 \left(\frac{M_2}{M_1}\right). \qquad (4-2)$$

For light stable nuclei, $M \approx 2Z$, $\frac{M_2}{M_1} = \frac{Z_2}{Z_1}$,

$$R_{12} = \left(\frac{Z_2}{Z_1}\right)^3.$$

with $Z_2 = 4$ and $Z_1 = 3$, for example, $R_{12} = \frac{64}{9}$. Our experiments studied only one or two nucleon transfers from or to stable nuclei. Extremely neutron deficient or extremely neutron rich isotopes were not involved. So usually it is true that $\frac{M_2}{M_1} > \left(\frac{Z_1}{Z_2}\right)^2$ and $R_{12} > 1$. This means two neighboring families of Z are separated. As an example, if $Z_1 = 3$ (Li) and $Z_2 = 4$ (Be), then $\left(\frac{Z_2}{Z_1}\right)^2 = \frac{16}{9}$. For R_{12} to be less than 1, $\frac{M_2}{M_1}$ must be less than $\frac{16}{9}$. However, this requires very neutron deficient Be isotopes and very neutron rich Li isotopes which do not exist.

To sum up for our experiments, bands in the same family of Z (isotopes) are separated by their masses; families are separated predominantly by their Z values. So each band in the $\Delta E - E_T$ spectrum corresponds to a unique pair of (Z, M).

To determine the k values and to plot the M, Z bands for reference, some input data from known particles are needed. Table 4.1 lists the products $\Delta E \cdot E_T$ and k values for various known nuclei observed. Values of ΔE and E_T come from direct measurements. For other particles, $\Delta E \cdot E_T$ can be obtained through Eq. (4-1) with an average k. It is seen from the table that all k values are close to each other

so k can be treated as a constant. Fig. 4.1 shows discrete bands plotted according to Table 4.1.

Table 4.1. Values of $\Delta E \cdot E_T$ and k for different particles

Particle	Mass (amu)	Charge state	$\Delta E \cdot E_T$ (MeV^2)	k
^{4}He	4.003	+2	16.2	1.01
^{6}He	6.019	+2	22.3	0.93
^{7}Li	7.016	+3	68.2	1.08
^{8}Li	8.022	+3	75.0	1.04
^{7}Be	7.017	+4	130	1.16

When a nucleus appears in the $\Delta E - E_T$ spectrum, its position (ΔE, E_T) tells which band it belongs to and its MZ^2 and Z^2 are immediately known. Its mass is then calculated by dividing its $\Delta E \cdot E_T$ by Z^2. In this way the nucleus is identified.

Finally, for a nucleus to qualify as the product of certain reactions, its energy must be consistent with the kinematically predicted values (Appendix A). Also, based on the experiment setup, it must be true that the nuclei cannot be produced in other ways.

4.2 Correction for Kinematic Shift

In the two-body reaction $m_2(m_1, m_3)m_4$ the kinetic energy (Fig. A.1) of ejectile m_3 depends on its emission angle θ. Such dependence is called kinematic shift (see Appendix A). If we use $KE(\theta)$ to denote the kinetic energy, we can write it as

$$KE(\theta) = KE(\theta_o) - KS(\theta - \theta_o). \qquad (4-3)$$

The angle θ_o is a reference angle and is usually the angle at which the detector is centered. The shift term $KS(\theta - \theta_o)$ is such that $KE(\theta) < KE(\theta_o)$ when $\theta > \theta_o$.

In rare-event measurements like our radioactive beam experiments, a detector with a large solid angle is necessary to collect a reasonably large number of events.

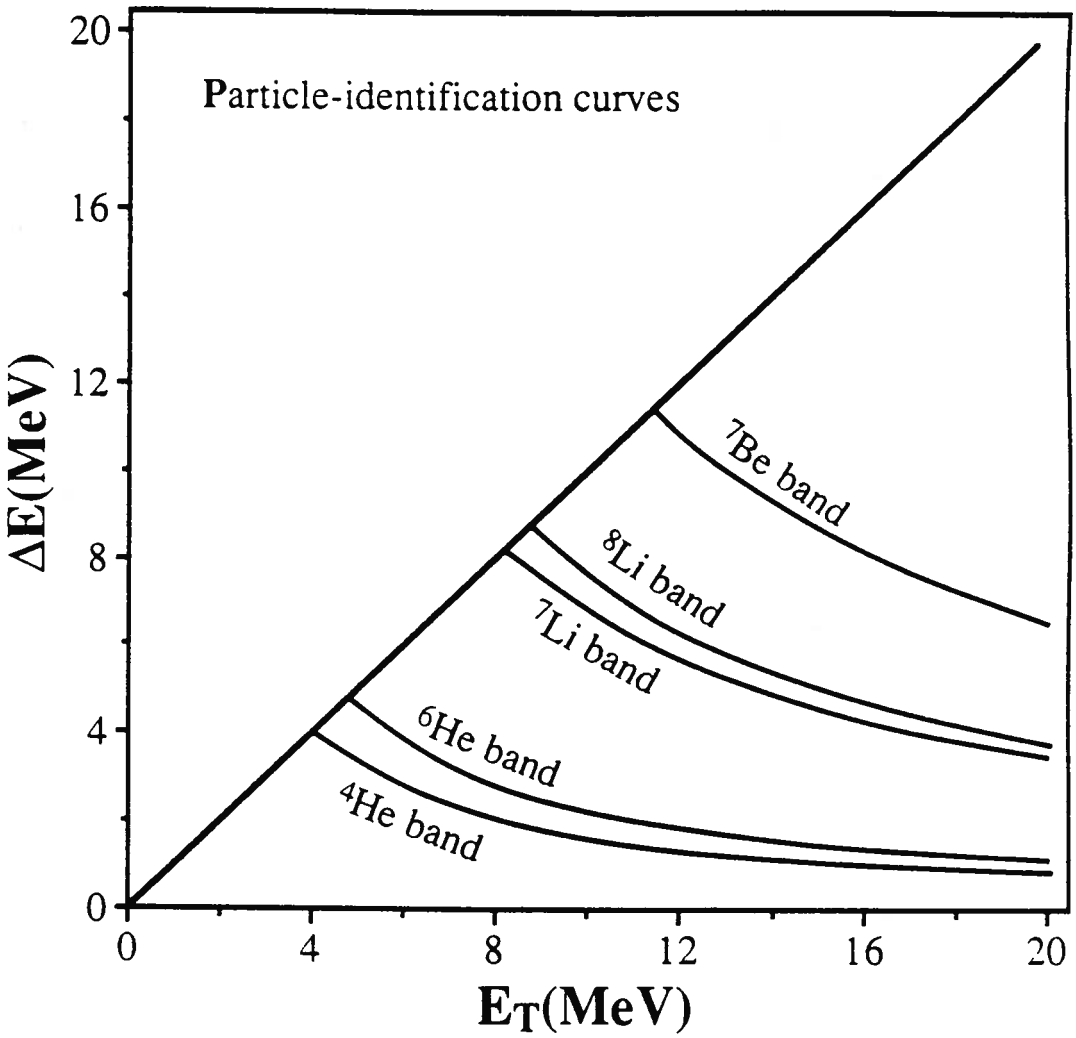

Fig. 4.1 Curves defined by $\Delta E \cdot E_T = kMZ^2$ for different types of particles.

However, the large solid angle introduces additional energy spreads to the ion peaks, which are already broad due to the energy spread of the incident beam and the target thickness. Neighboring peaks can then merge into each other. This makes it difficult to separate groups corresponding to closely spaced energy levels of the product particles. In some cases, correction for the kinematic shift is needed.

To illustrate the correction procedure and the change after correction, we take as an example the reaction ^{9}Be(^{8}Li,^{7}Li)^{10}Be g.s. In this experiment the ^{9}Be target was 1.80 mg/cm^2 thick and the detector was centered at 20°. The effective detection area was 200 mm^2, covering an angular range of 7.52°. The kinetic energy of the ^{8}Li beam was 14.4 MeV. Under these conditions the calculated kinetic energy spread, without regard to the loss in the target, is 0.92 MeV. To correct the kinematic shift, the energies of ^{7}Li at discrete angles are first calculated. $KS(\theta - \theta_o)$ is then fitted to a simple function. For the reaction under consideration, $KS(\theta - \theta_o)$ can be well approximated by a linear function:

$$KS(\theta - \theta_o) = [6.99(\theta - \theta_o) + 1.78 \times 10^{-2}] \text{ MeV}, \qquad (4-4)$$

where θ is measured in radians and is given by Eq. (2-38). This function is then added to $KE(\theta)$ to form $KE(\theta_o)$. The spectrum of $KE(\theta_o)$ is then free of kinematic shift.

Figs. 4-2 and 4-3 show the energy spectra of ^{7}Li from the reaction before and after kinematic shift correction. The energy spread is reduced from 1.13 MeV to 0.96 MeV. The remaining spread after correction is attributed to the beam energy spread and target thickness. In fact, the contributions from the beam and target can be estimated after this correction. Kinematic correction also helps to separate product particles from elastically scattered beam particles so reaction rates can be determined more precisely.

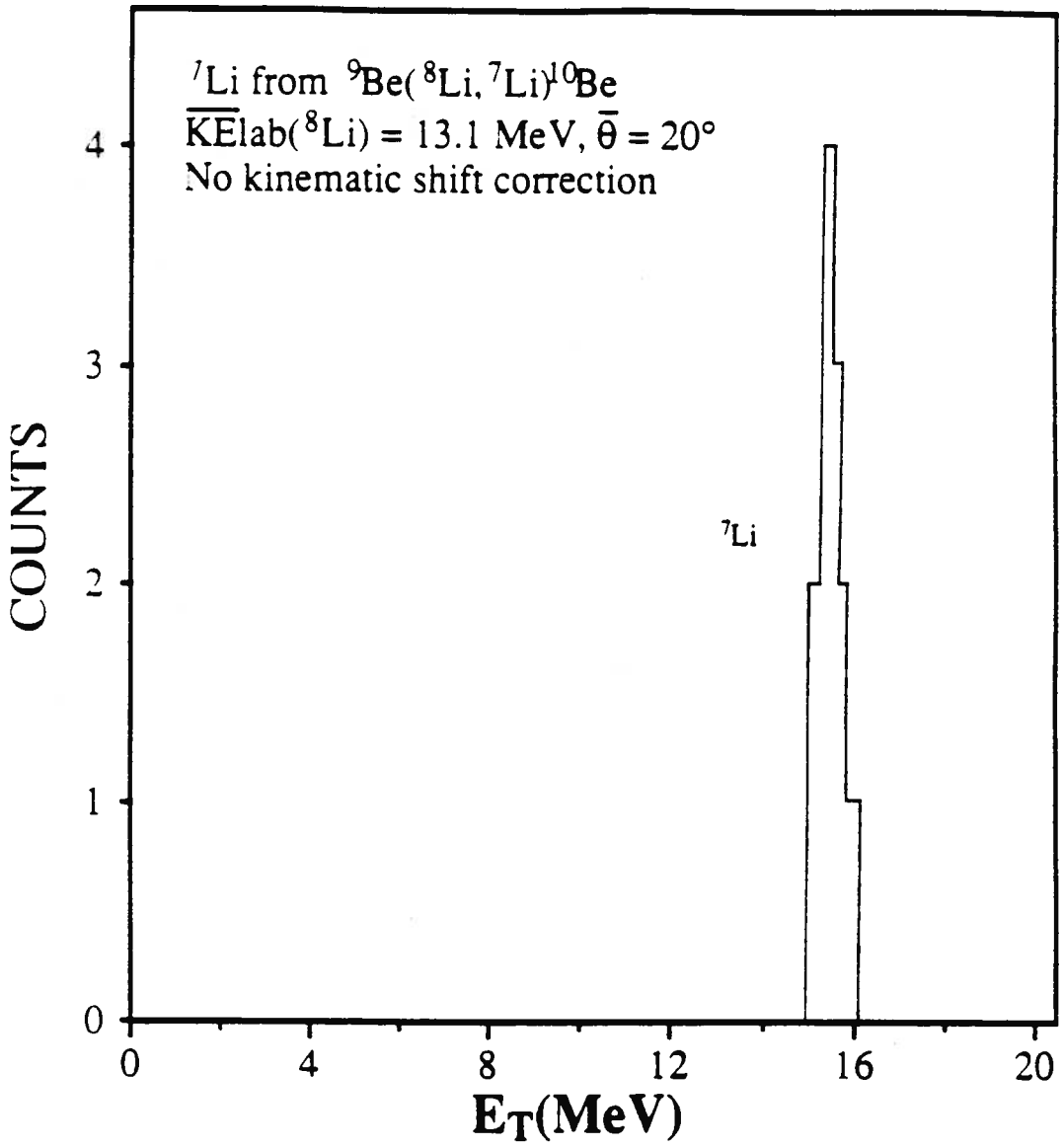

Fig. 4.2 Energy spectrum of ^{7}Li from reaction ^{9}Be(^{8}Li,^{7}Li)^{10}Be without kinematic shift correction, at $\overline{KE}_{lab}$ (^{8}Li) = 13.1 MeV and $\bar{\theta}_{lab} = 20°$.

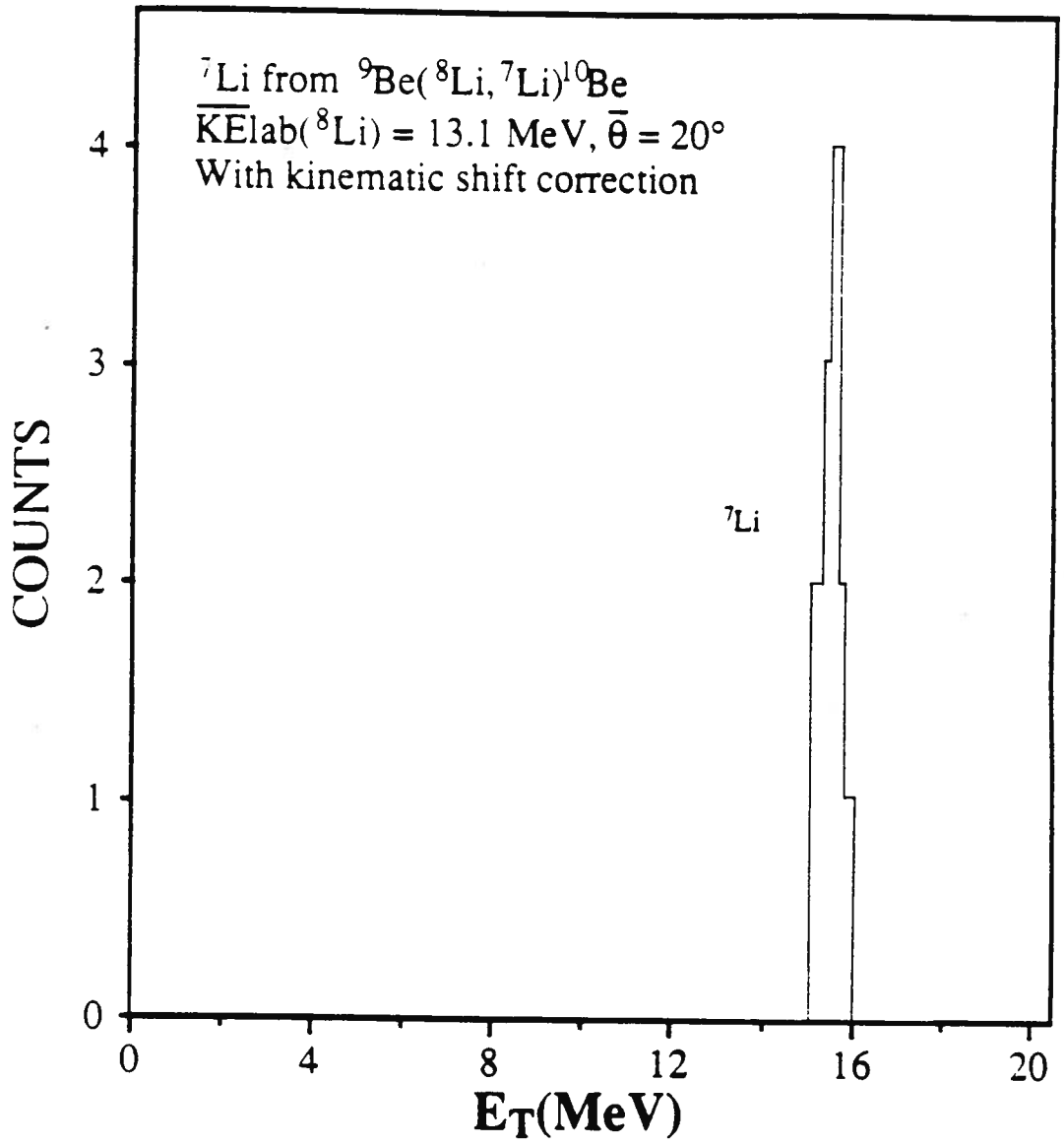

Fig. 4.3 Energy spectrum of ^{7}Li from reaction ^{9}Be(^{8}Li,^{7}Li)^{10}Be with kinematic shift correction, at $\overline{KE}_{lab}$ (^{8}Li) = 13.1 MeV and $\bar{\theta}_{lab} = 20°$.

4.3 Comments on the Measurement of $\frac{d\sigma}{d\Omega}$

The differential cross section $\frac{d\sigma(\theta,\phi)}{d\Omega}$ for the reaction $m_2(m_1,m_3)m_4$ is defined by

$$\frac{d\sigma(\theta,\phi)}{d\Omega} = \frac{\Delta N(\theta,\phi)}{N} \cdot \frac{1}{nx \cdot \Delta\Omega}, \ \Delta\Omega \to 0, x \to 0, \qquad (4-5)$$

where $\Delta\Omega$ is the solid angle element centered at (θ,ϕ), $\Delta N(\theta,\phi)$ is the number of particles of type m_3 ejected into this $\Delta\Omega$, N is the total number of type m_1 ions incident on the target, and nx is the target atomic number density n times its thickness x. Thus, the quantity $\frac{\Delta N(\theta,\phi)}{N}$ is the probability that an incident particle m_1 is converted into m_3 and that m_3 comes out in the $\Delta\Omega$ at (θ,ϕ). $\frac{d\sigma(\theta,\phi)}{d\Omega}$ is proportional to this probability.

The relationship between the differential cross section and the corresponding total cross section σ is simply

$$\sigma = \int_0^{2\pi} d\phi \int_0^{\pi} \frac{d\sigma(\theta,\phi)}{d\Omega} sin\theta d\theta. \qquad (4-6)$$

To perform the integration it is necessary that the distribution of $\frac{d\sigma(\theta,\phi)}{d\Omega}$ be known over the ranges $0 \leq \phi \leq 2\pi$ and $0 \leq \theta \leq \pi$.

If the target is unpolarized, and if the beam is unpolarized or only polarized in the direction of the beam axis, the reaction should be azimuthally symmetric and the differential cross section should be independent of ϕ. In this case we write

$$\frac{d\sigma(\theta)}{d\Omega} = \frac{\Delta N(\theta)}{N} \cdot \frac{1}{nx \cdot \Delta\Omega}, \qquad (4-7)$$

$$\sigma = 2\pi \int_0^{\pi} \frac{d\sigma(\theta)}{d\Omega} sin\theta d\theta. \qquad (4-8)$$

$\Delta\Omega_{lab}$ and θ_{lab} in the laboratory system are given by Eqs. (2-35) and (2-36), respectively. The corresponding quantities $\Delta\Omega_{cm}$ and θ_{cm} in the center-of-mass system

can be obtained via standard conversions [Eqs. (A1-17), (A1-19) and (A1-11) in the appendix]. All cross sections presented in this chapter have been calculated in the cm system.

While the quantities N, nx and $\Delta\Omega$ on the right hand side of Eq. (4-8) can be measured precisely, it takes some care to decide $\Delta N(\theta)$, the number of product particles of interest. $\Delta N(\theta)$ can be counted by setting a gate (a contour) around the reaction product group in the $\Delta E - E_T$ spectrum. The group is identified by its value of $\Delta E \cdot E_T$ and its average kinetic energy. The gate is centered at energy E_T corresponding to reaction taking place at the target center with average beam energy, but it extends horizontally to left and right with an amount equal to the sum of the energy spread of the beam, energy spread due to the target thickness and the energy resolution of the $\Delta E - E_R$ system. The extension of the gate in the ΔE direction (vertical) is equal to the ΔE-detector's energy resolution, plus the ΔE energy spread due to different impinging angles. Very careful determination of the gate sizes is not necessary for reactions of large Q-values for which the reaction products are distinctive. But it becomes important for reactions with small Q-values for which the reaction product groups are not far from the intense elastically scattered beam. Sometimes kinematic correction is needed for better separation of neighboring groups. The energy spectra of the product groups are obtained by projecting the gated events on the E_T coordinate.

4.4 Cross Sections for ^{8}Li Induced Reactions

The ^{8}Li beam, produced in the production target in the front chamber, was focused onto the focal plane at the second target position for different nuclear reactions. Elastically scattered ^{7}Li ions from the primary beam were stopped by the blocking detector in the mid chamber, and other types of ions that had magnetic rigidities different than that of ^{8}Li were filtered out by the collimator in the back

chamber. As previously noted, the ^{8}Li beam had a purity of 70%, an average energy of 14.4 MeV and an energy spread (FWHM) of 600 keV or less (see Chapter 3).

The second-target ladder in the back vacuum chamber (Fig. 2.1) was capable of holding four targets of about 1 inch diameter at a time. The desired target could be slid into the beam position to initiate nuclear reactions. If more than four targets must be used, the chamber had to be opened and new targets mounted. Table 4.2 shows the targets used and the corresponding transfer reactions studied. In the table ^{10}Be* stands for ^{10}Be in its first excited state of 3.368 MeV. Commercially available ^{9}Be foil[1] (99.99% pure) and ^{12}C foil[2] (98.90% pure) were used, while $^{13}CH_2$ and TiD_2 foils were prepared using the methods described in Appendix C. $^{13}CH_2$ was used for the reaction ^{13}C(^{8}Li,^{7}Li)^{14}C (Q = 6.143 MeV) because $^{13}CH_2$ foils could be made with large areas. The reaction ^{1}H(^{8}Li, ^{7}Li)^{2}H (Q = 0.191 MeV) from the H component in $^{13}CH_2$ did not interfere because of its much smaller Q-value, greater recoil energy and small maximum emerging angle of ^{7}Li ($\theta_{max} = 11.5°$) due to small mass of ^{2}H. For the reaction

$$^2\mathrm{H}(^8\mathrm{Li},\ ^7\mathrm{Li})^3\mathrm{H}\ g.s.,\ \ Q = 4.224\ \mathrm{MeV}, \qquad (4-9)$$

CD_2 foils were used in early runs, but the reaction

$$^{12}\mathrm{C}(^8\mathrm{Li},\ ^7\mathrm{Li})^{13}\mathrm{C},\ \ Q = 2.913\ \mathrm{MeV} \qquad (4-10)$$

also took place due to C component in CD_2. Particularly, ^{7}Li in (4-9) and ^{7}Li in (4-10) have nearly the same energy at $\theta_{lab} = 12°$ (16.85 MeV) and one cannot tell which reaction the ^{7}Li products come from. For this reason, TiD_2 foils were used instead in later runs. It is believed that the reaction

$$^{48}\mathrm{Ti}(^8\mathrm{Li},\ ^7\mathrm{Li})^{49}\mathrm{Ti},\ \ Q = 6.109\ \mathrm{MeV} \qquad (4-11)$$

has negligible cross section at E (^{8}Li) = 14.4 MeV. Even if this is not true, (4-12)

has a much higher Q-value and hence much lower recoil energy than (4-9). Thus reaction products from different target components are identifiable. Experimental data have proved TiD_2 to be good target for the reaction $^2H(^8Li, ^7Li)^1H$.

Table 4.2 One neutron transfer reactions and second targets used

Reaction	Q-value (MeV)	Target Composition	Thickness (mg/cm^2)
^9Be (^8Li, ^7Li) ^{10}Be	4.779	^9Be	1.80 ± 0.01
^9Be (^8Li, ^7Li) $^{10}Be^*$	1.411	^9Be	1.80 ± 0.01
^{12}C (^8Li, ^7Li) ^{13}C	2.913	^{12}C	2.20 ± 0.01
^{13}C (^8Li, ^7Li) ^{14}C	6.143	$^{13}CH_2$	0.54 ± 0.02
^2H (^8Li, ^7Li) ^3H	4.224	TiD_2	2.72 ± 0.03
		CD_2	1.90 ± 0.1

All data was collected from the UM Radioactive Ion Beam Facility attached to the University of Notre Dame three-stage Van de Graaff Accelerator. For each target, several measurements were made. Each measurement consisted of taking data with the $\Delta E - E_R$ detector at a fixed angle. Since the detector covered a large angular range ($\Delta\theta_{lab} = 7.5°$), it could be moved with large angular steps between measurements. To eliminate false events, a tapered collimator (Fig. 2.6) was placed in front of the $\Delta E - E_R$ detector. The collimator directly faced the second target and only particles originating from the target were collected. Background particles from other directions were mostly eliminated. The residual background was checked by removing the target. When there was no target in place, the ^7Li groups and other products were not seen. This verified that the products were really results of the interaction of the ^8Li beam with the targets. The ΔE and E_R detectors were sometimes operated in coincidence so that particles without sufficient energy to penetrate the ΔE detector were not registered.

All data was tape-recorded and data analyses have been performed with a general purpose data analysis program, named LISA, on the UM Nuclear Physics Group's Micro-VAXII/GPX computer. The analyses induced energy calibration,

position calibration, beam normalization, particle identification and spectra generation, etc. The energy signals have been such calibrated that the ratio 1 MeV/100 channel applies to all $\Delta E - E_T$ and E_T spectra, i.e.

$$E_T = ch(E_T) \times 0.01 \text{ MeV}, \qquad (4-12)$$

$$\Delta E = ch(\Delta E) \times 0.01 \text{ MeV}. \qquad (4-13)$$

A $\Delta E - E_T$ spectrum and an E_T spectrum for each of the reactions contained in Table 4.2 are shown in Figs. 4.4 - 4.11. The $\Delta E - E_T$ spectrum contains all events detected by the $\Delta E - E_R$ detector at a fixed angle. The events in the circles represent the reaction products. The E_T spectrum is the projection of the gated events on the E_T coordinate.

Elastic and inelastic scattering of ^{8}Li from various targets, Coulomb excitation of ^{8}Li from Au target, and single nucleon transfer reactions have been studied in our experiments. The observed angular distributions of differential cross sections for the one neutron transfer reactions listed in Table 4.2 are shown below (Figs. 4.12 - 4.16). The angle θ_{cm} is the product particle's emerging angle with respect to the beam axis in the center-of-mass system, and $\left(\frac{d\sigma}{d\Omega}\right)_{cm}$ (independent of the azimuthal angle ϕ) represents the differential cross section measured in the same system. Our measured differential cross sections have typical uncertainties of about 20%. Angular uncertainties are about 4°, which largely come from the angular divergence ($\pm$ 3.5°) of the cone-shape secondary beam (Fig. 2.3) and the finite size ($\sim$ 1 cm diameter) of the beam spot on the second target. We emphasize here that these are results of *secondary* reactions. The intensity of a secondary beam is only about 10^{-7} times that of a primary beam. Large collection solid angles are necessary to make a usable beam and large angular uncertainties result. Although

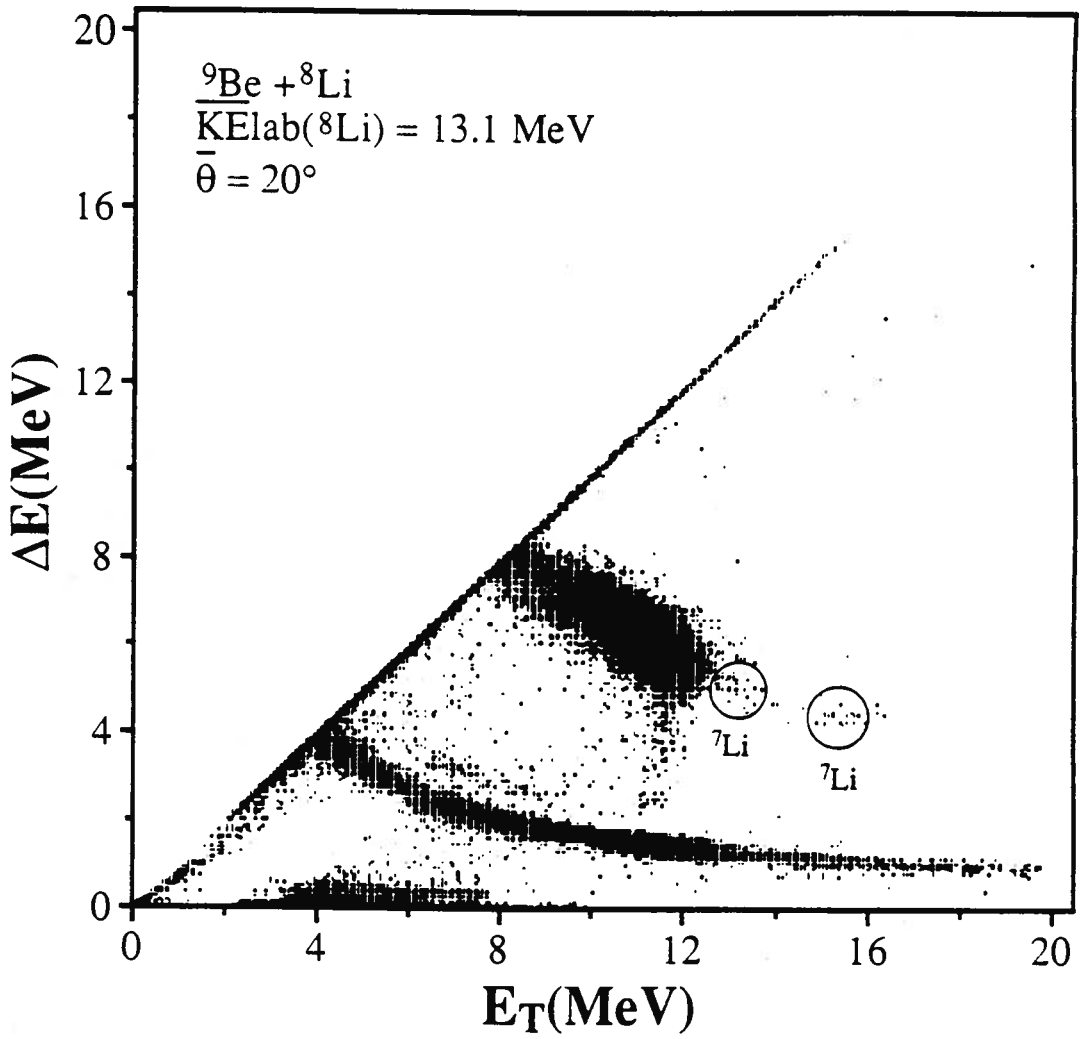

Fig. 4.4 $\Delta E - E_T$ spectrum of products from ^{9}Be + ^{8}Li reaction at $\overline{KE}_{lab}$ (^{8}Li) = 13.1 MeV and $\bar{\theta}_{lab} = 20°$.

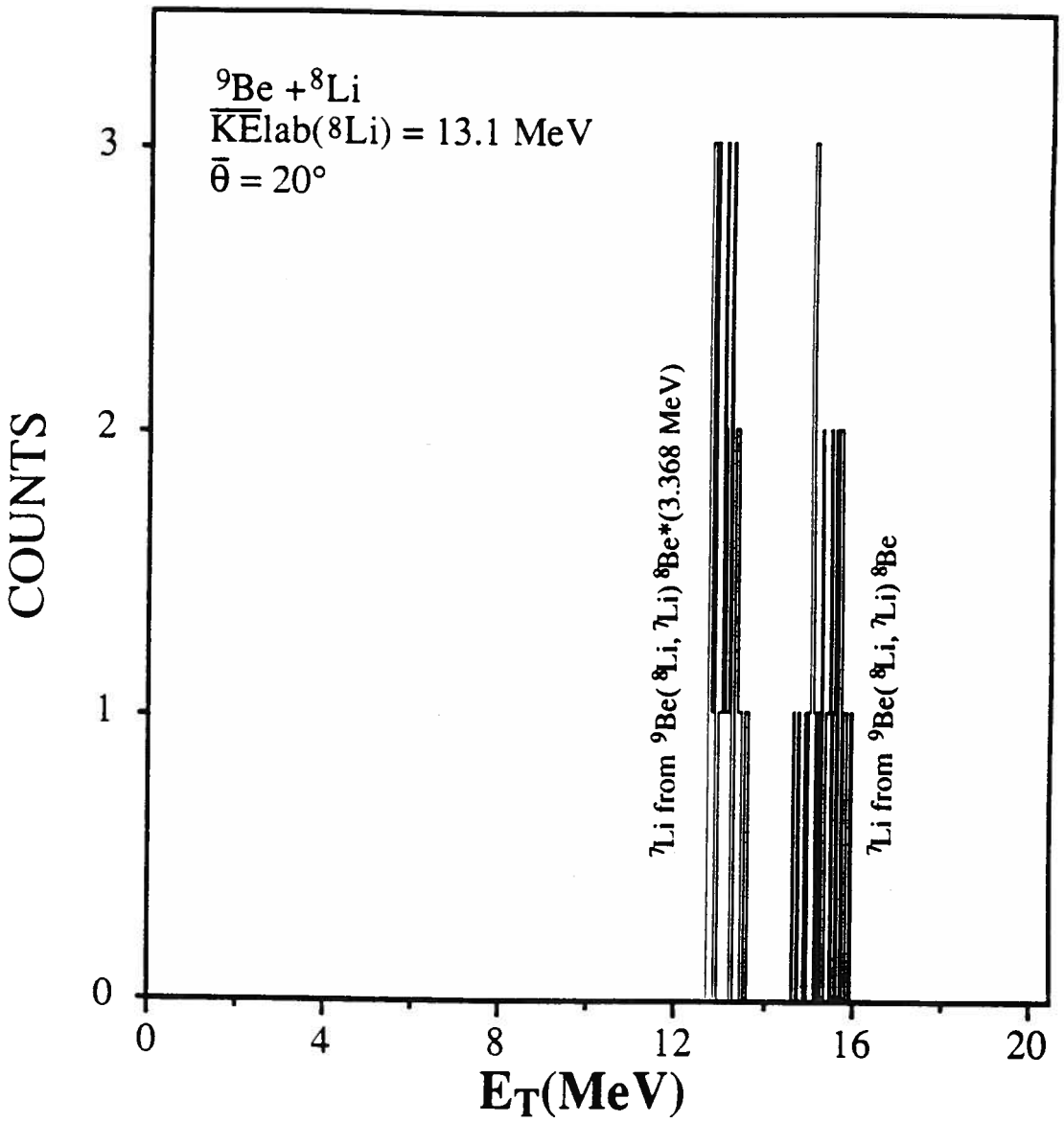

Fig. 4.5 E_T spectrum of ^{7}Li products from ^{9}Be(^{8}Li,^{7}Li)^{10}Be and ^{9}Be(^{8}Li,^{7}Li)^{10}Be* (3.368 MeV at $\overline{KE}_{lab}$ (^{8}Li) = 13.1 MeV and $\bar{\theta}_{lab} = 20°$.

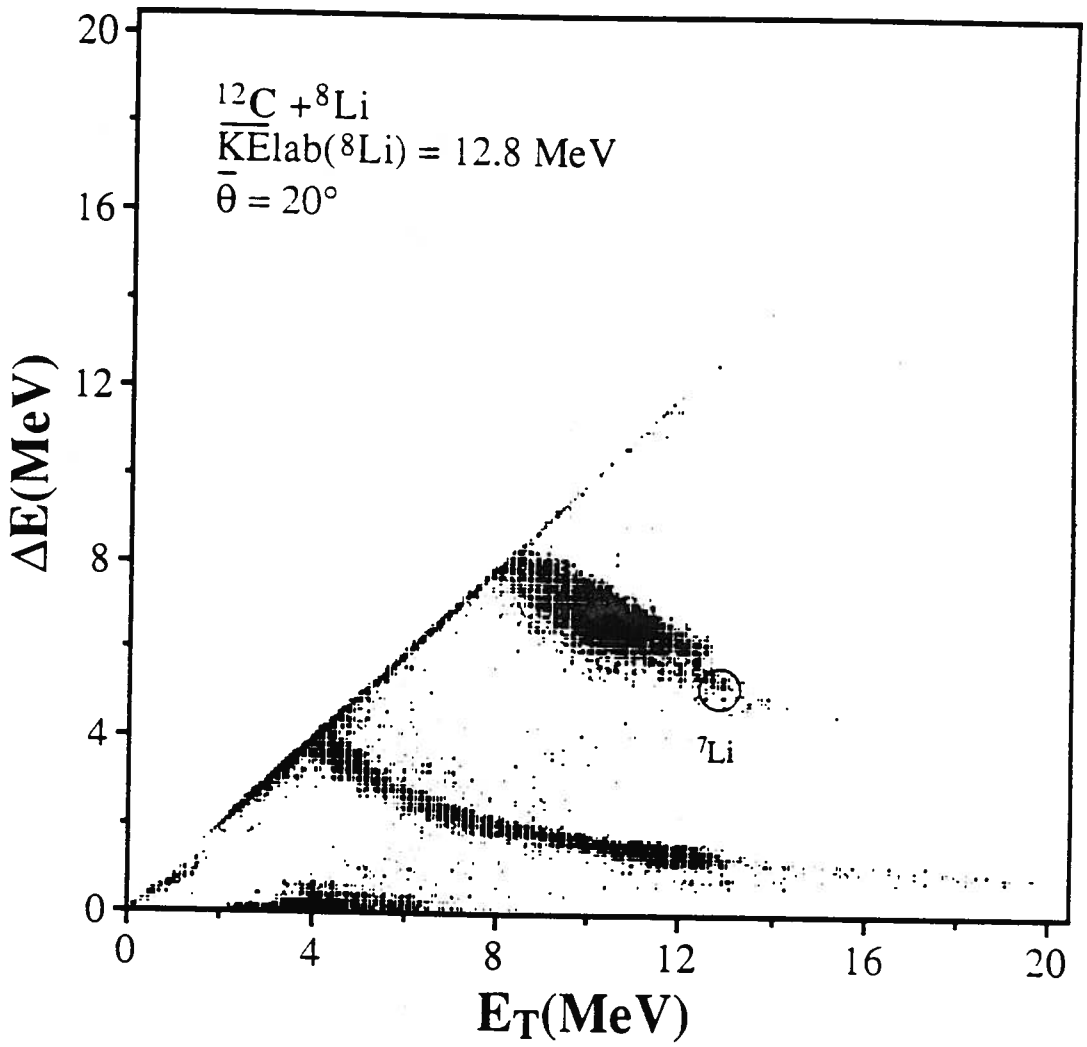

Fig. 4.6 $\Delta E - E_T$ spectrum of products from $^{12}C + ^{8}Li$ reaction at $\overline{KE}_{lab}$ (^{8}Li) = 12.8 MeV and $\bar{\theta}_{lab} = 20°$.

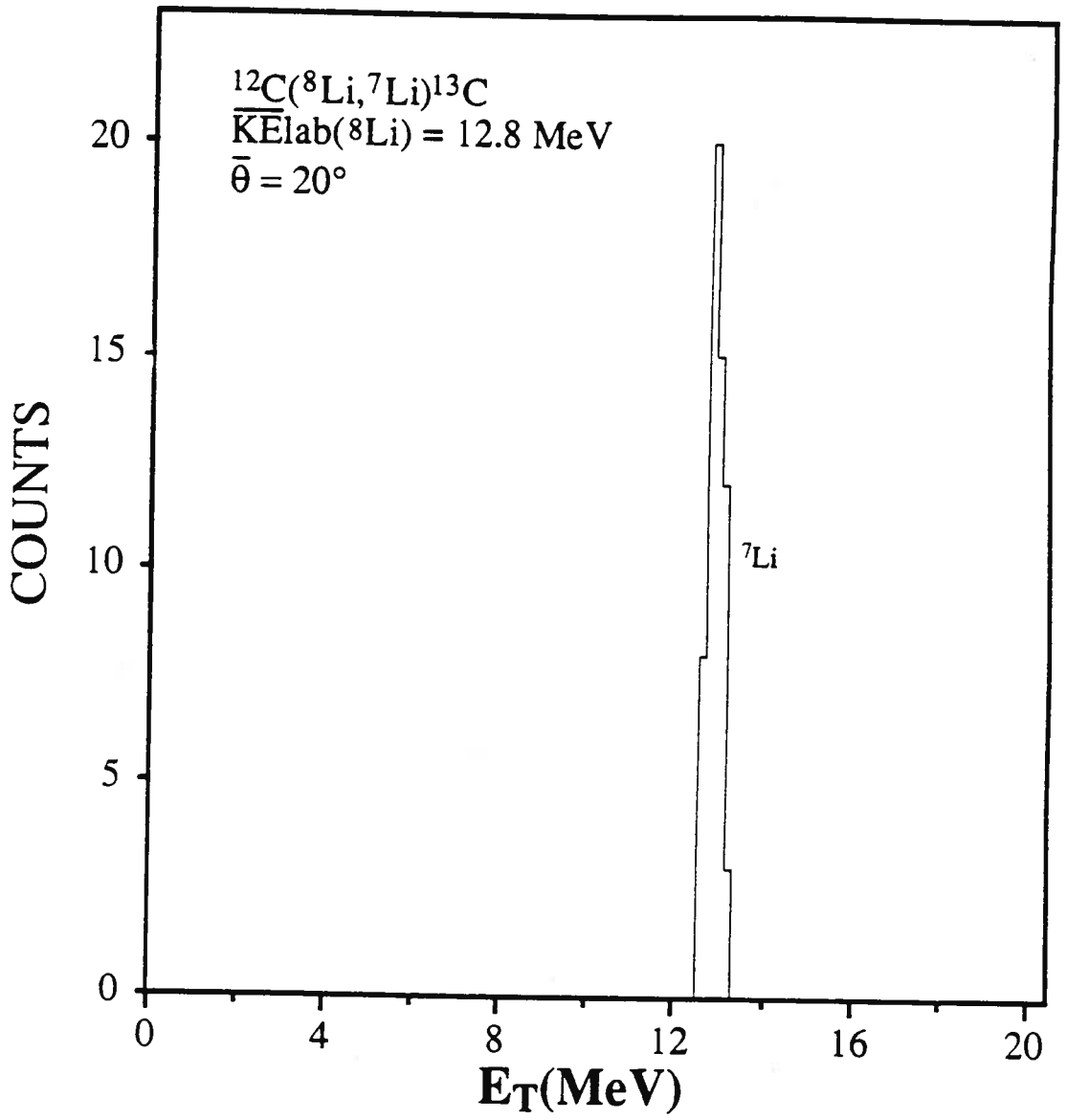

Fig. 4.7 E_T spectrum of ^{7}Li from ^{12}C(^{8}Li,^{7}Li)^{13}C at $\overline{KE}_{lab}$ (^{8}Li) = 12.8 MeV and $\bar{\theta}_{lab} = 20°$.

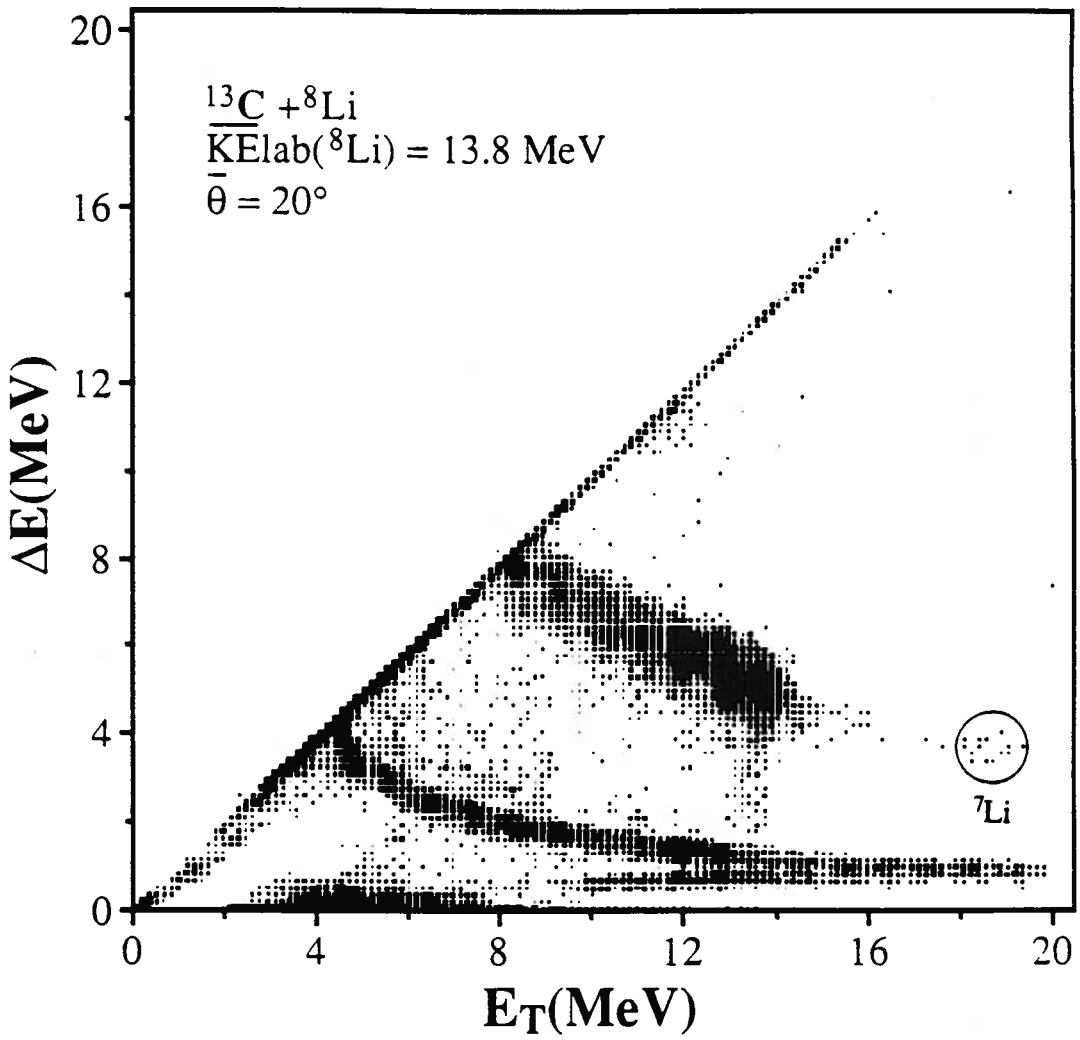

Fig. 4.8 $\Delta E - E_T$ spectrum of products from ^{13}C + ^{8}Li reaction at $\overline{KE}_{lab}$ (^{8}Li) = 13.8 MeV and $\bar{\theta}_{lab} = 20°$.

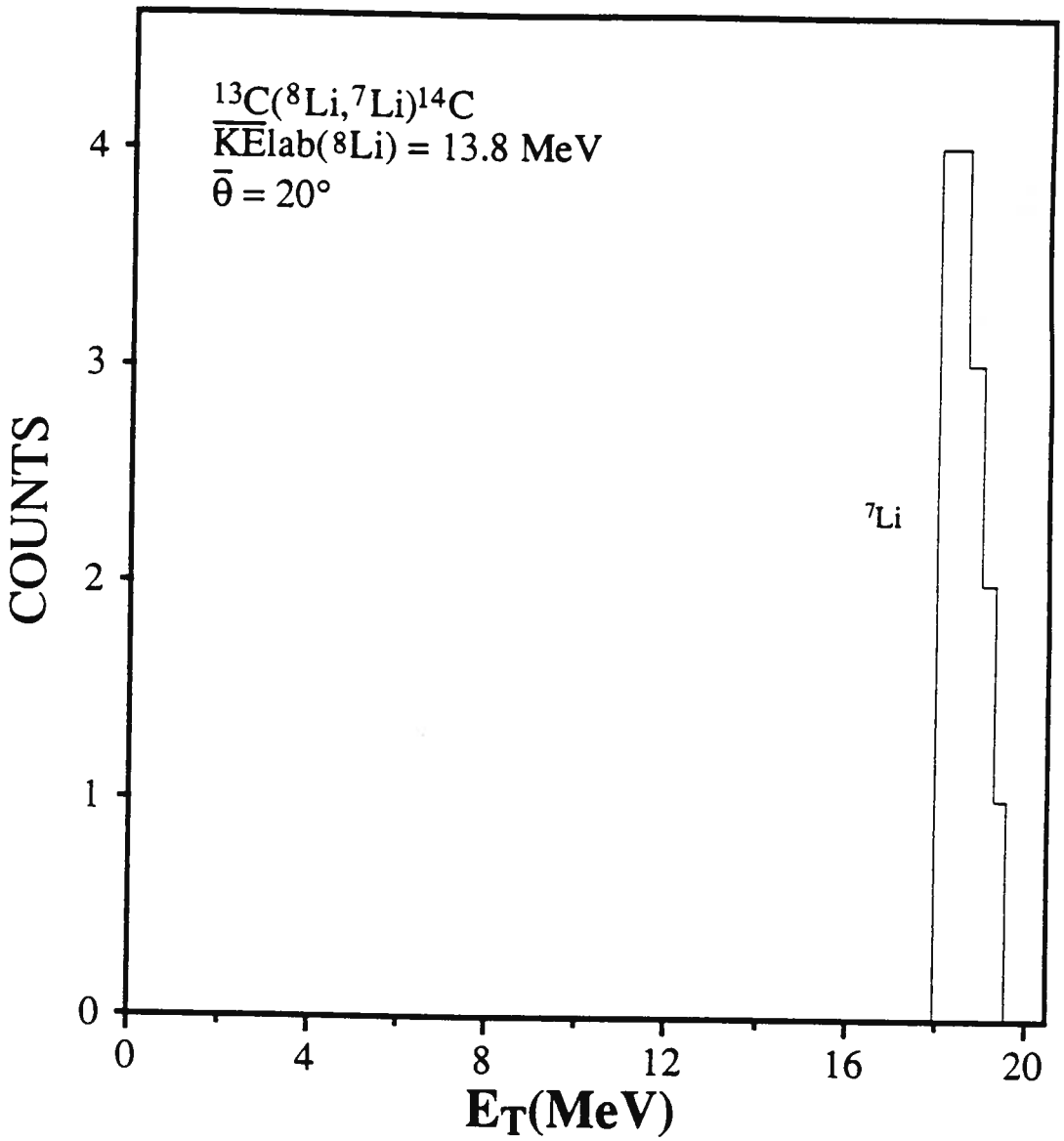

Fig. 4.9 E_T spectrum of ^{7}Li from ^{13}C(^{8}Li,^{7}Li)^{14}C at $\overline{K^{*}E}_{lab}$ (^{8}Li) = 13.8 MeV and $\bar{\theta}_{lab} = 20°$.

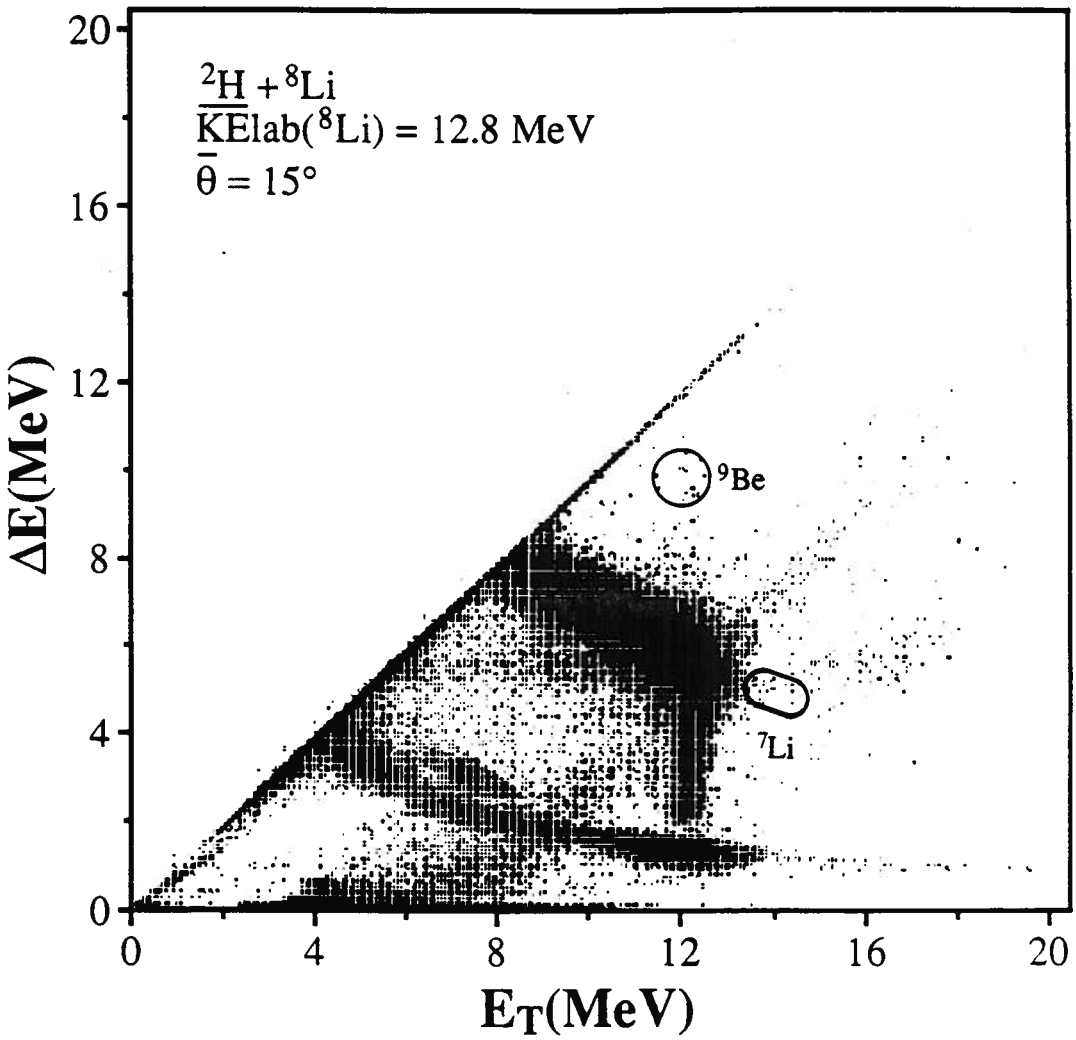

Fig. 4.10 $\Delta E - E_T$ spectrum of products from ^{2}H + ^{8}Li reaction at $\overline{KE}_{lab}$ (^{8}Li) = 12.8 MeV and $\bar{\theta}_{lab} = 15°$ using TiD_2 target.

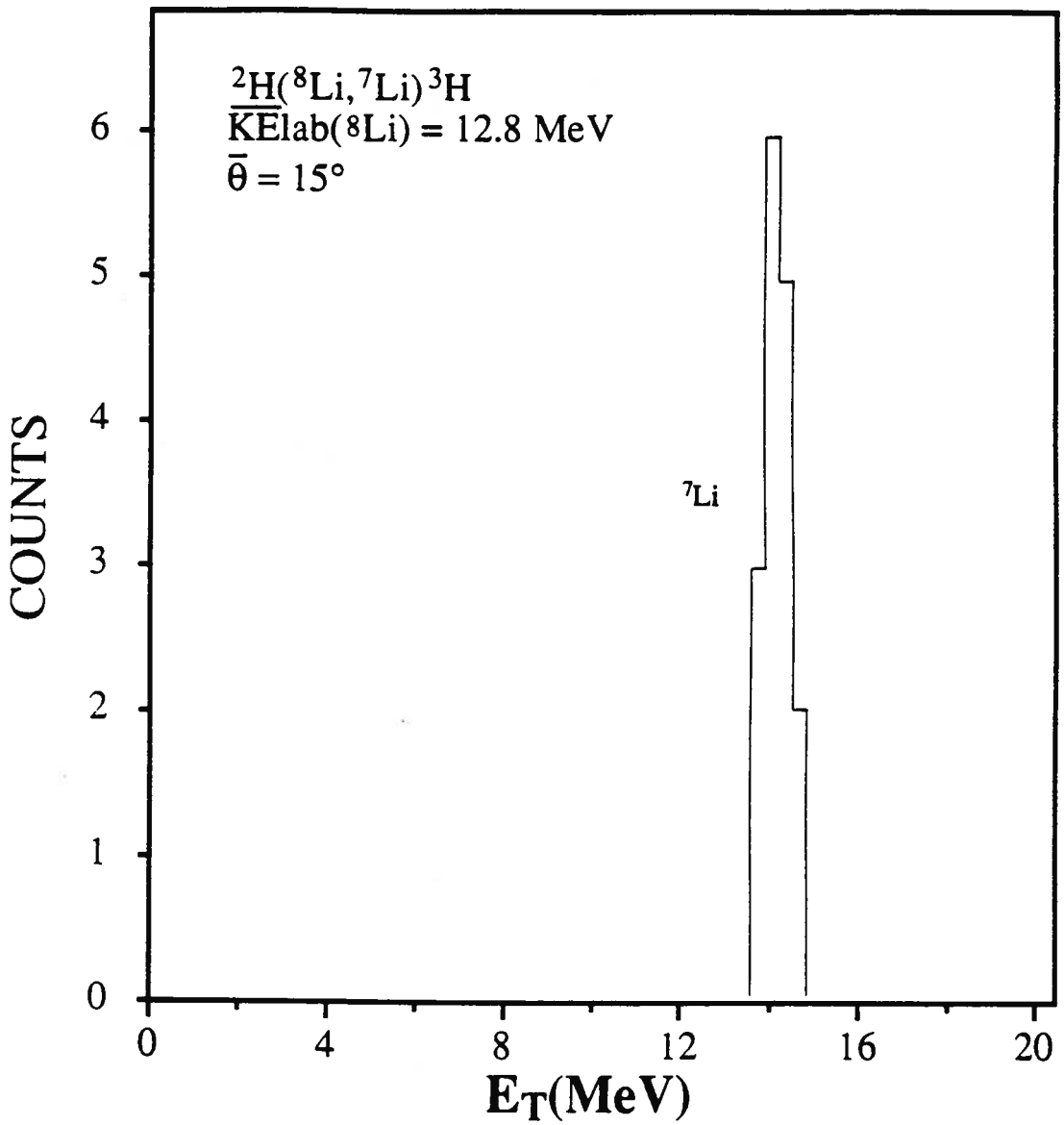

Fig. 4.11 E_T spectrum of ^{7}Li from ^{2}H(^{8}Li,^{7}Li)^{3}H at $\overline{KE}_{lab}$ (^{8}Li) = 12.8 MeV and $\bar{\theta}_{lab} = 15°$ using TiD_2 target.

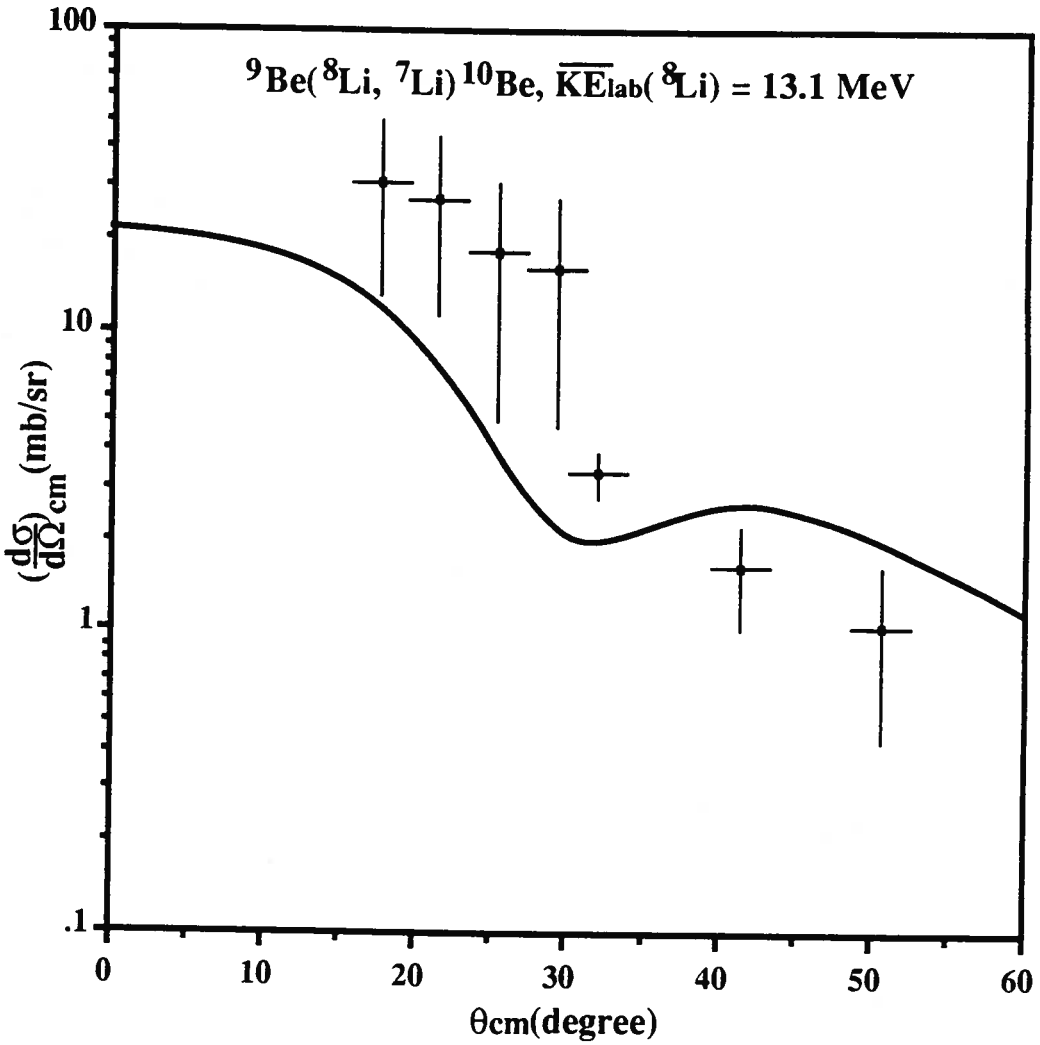

Fig. 4.12 Angular distribution of measured differential cross sections for ^{9}Be(^{8}Li,^{7}Li)^{10}Be at $\overline{KE}_{lab}$ (^{8}Li) = 13.1 MeV.

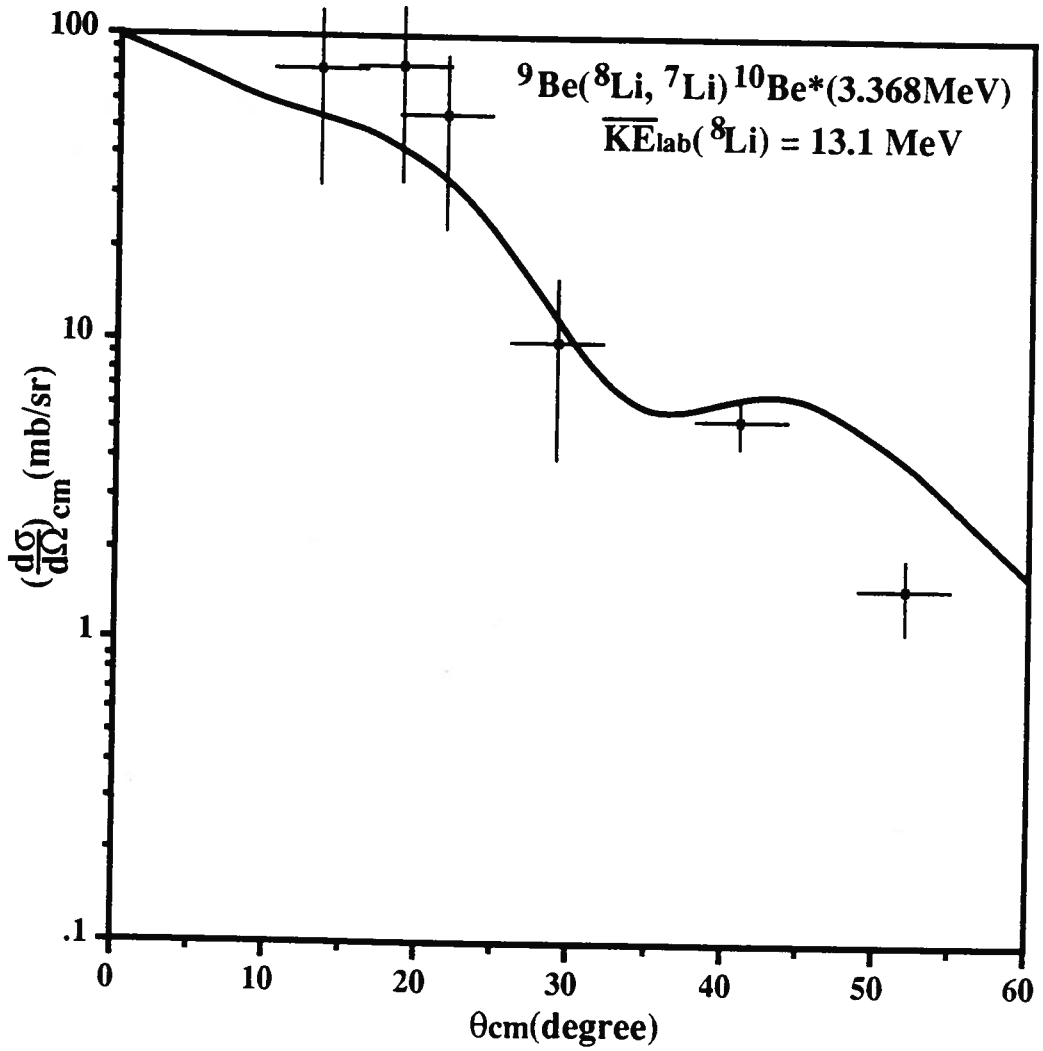

Fig. 4.13 Angular distribution of measured differential cross sections for ^{9}Be(^{8}Li,^{7}Li)^{10}Be* (3.368 MeV) at $\overline{KE}_{lab}$ (^{8}Li) = 13.1 MeV.

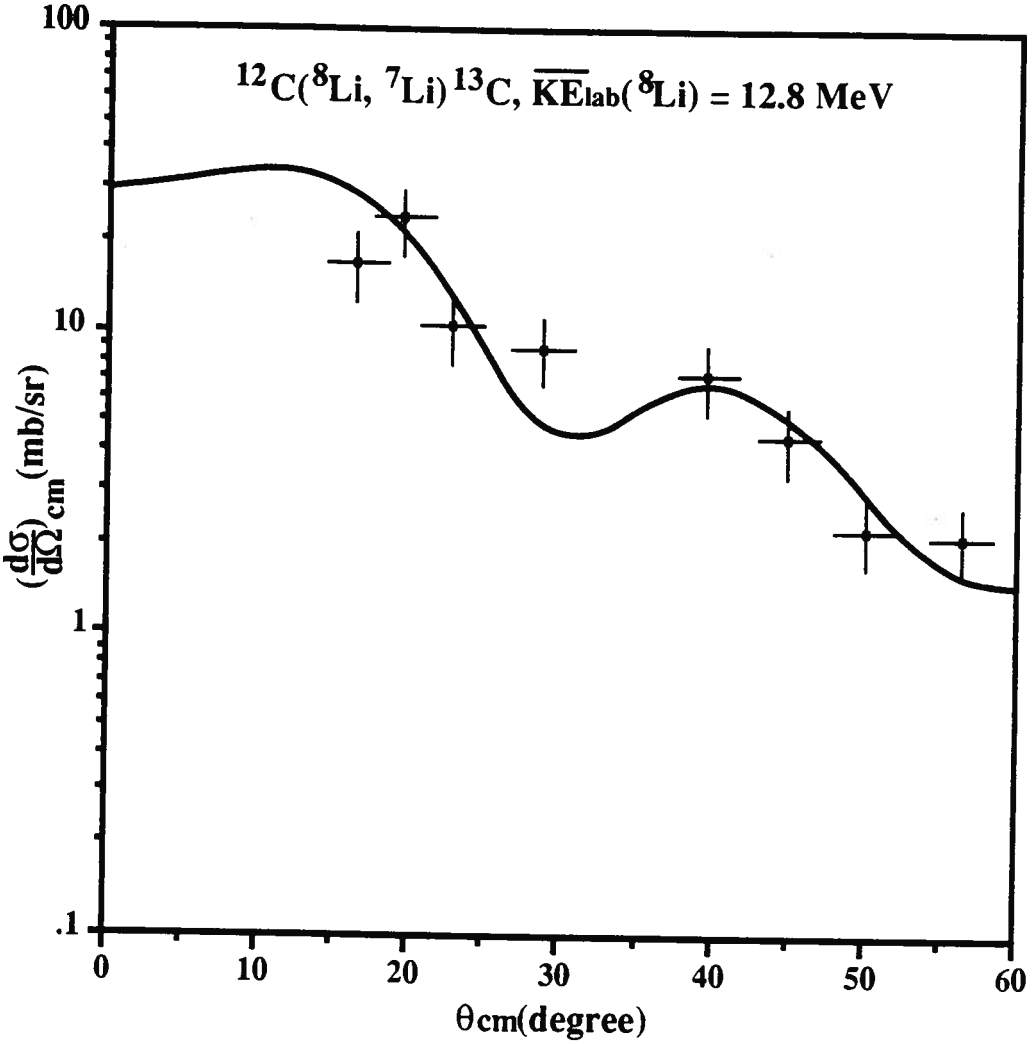

Fig. 4.14 Angular distribution of measured differential cross sections for $^{12}C(^{8}Li,^{7}Li)^{13}C$ at $\overline{KE}_{lab}$ (^{8}Li) = 12.8 MeV.

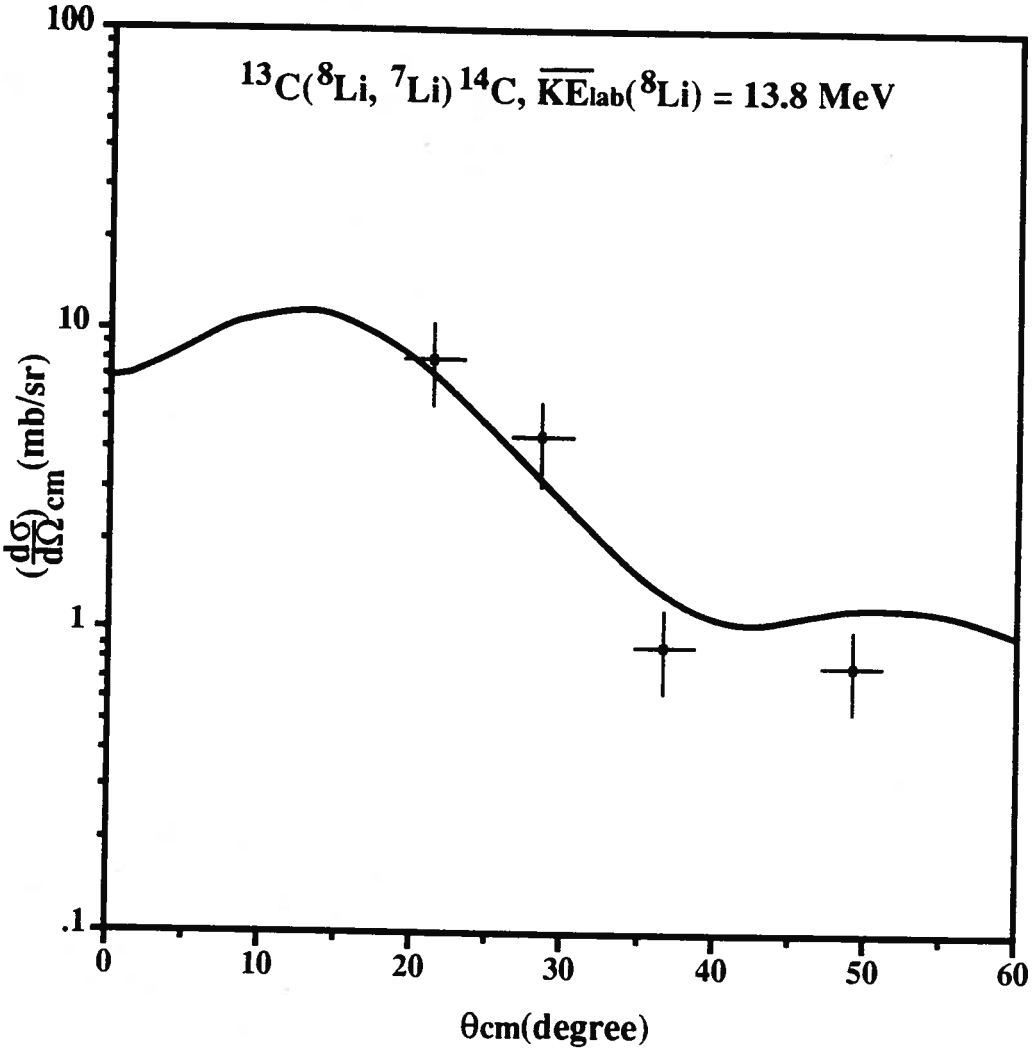

Fig. 4.15 Angular distribution of measured differential cross sections for $^{13}C(^{8}Li,^{7}LI)^{14}C$ at $\overline{KE}_{lab}$ (^{8}Li) = 13.8 MeV.

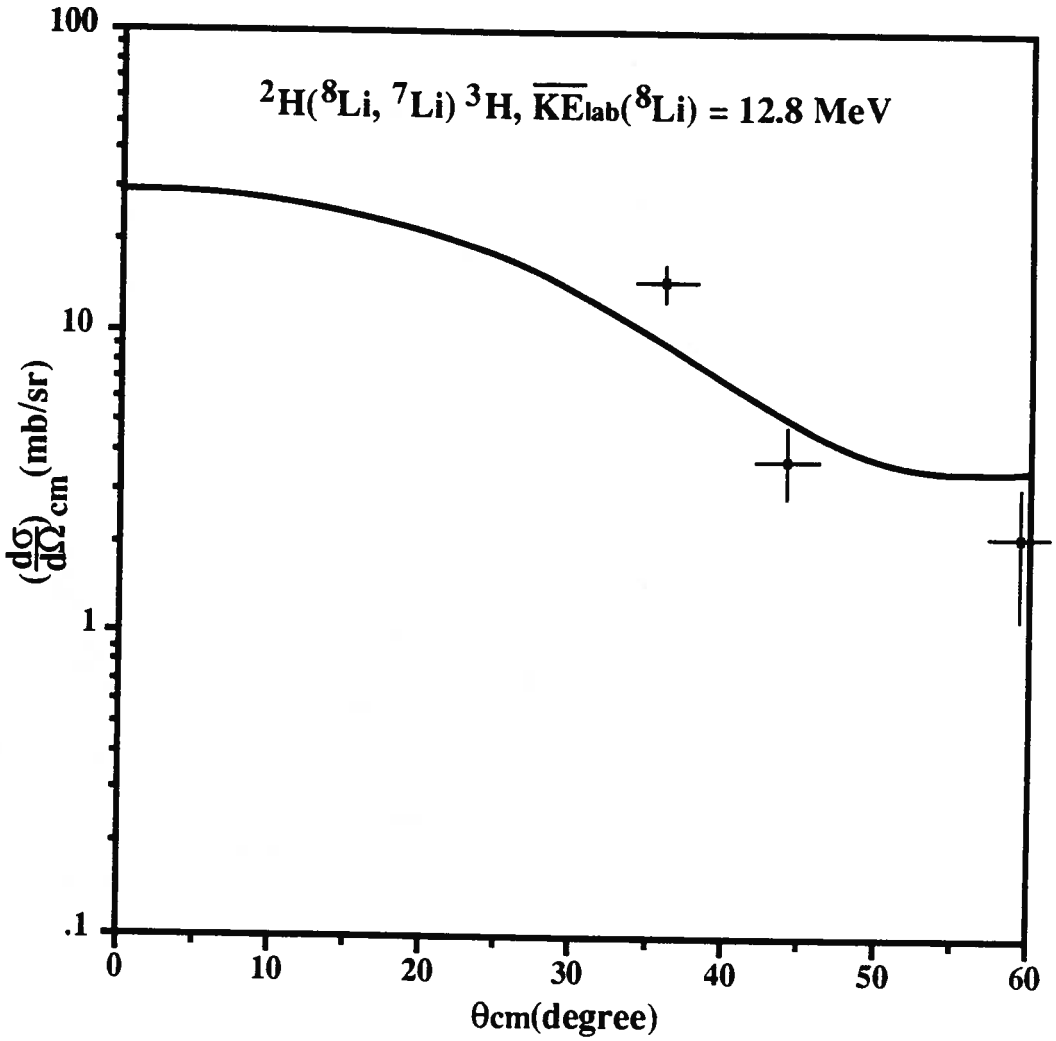

Fig. 4.16 Angular distribution of measured differential cross sections for ^{2}H(^{8}Li,^{7}Li)^{3}H at $\overline{KE}_{lab}$ (^{8}Li) = 12.8 MeV.

the running time at each angle is typically 8 to 16 hours, one cannot expect very good statistics of secondary reaction data.

Our present data of angular distributions do not cover the whole range of $\theta_{cm} = 0° - 180°$. Due to the angular spread of the secondary beam, the low angle edge of the $\Delta E - E_R$ detector must be about 8° (lab. angle) away from the beam axis to avoid direct beam impinging on the detector holder. This prevented us from collecting data at very small angles. Data at very large angles have not been obtained due to the very small reaction rates and limited accelerator running time. For light targets, there is also a kinematic restriction on the emerging angle. For example, for the reaction ^{2}H (^{8}Li, ^{7}Li) ^{3}H the maximum angle is $(\theta_{lab})_{max} = 31°$, or $(\theta_{cm})_{max} = 105.6°$.

The primary transfer reactions induced by ^{8}Li appear to be (^{8}Li, ^{7}Li). The transfer reactions (^{8}Li, ^{9}Li) and (^{8}Li, ^{9}Be) appear to be weaker (Figs. 4.4 - 4.11). In particular, the reaction ^{2}H(^{8}Li, ^{9}Be)n is of interest in nucleosynthesis (Sec. B, Chapter 1). We measure $d\sigma/d\Omega \approx 3$ mb/sr for this reaction (Fig. 4.10) at $\bar{\theta} = 15°$ and $\bar{E}_{lab} = 12.8$ MeV ($\bar{E}_{cm} = 2.56$ MeV).

The curves in the figures of angular distributions are results of FRDWBA (Finite Range Distorted Wave Born Approximation) calculations (see Chapter 5).

4.5 Inverse Reaction Test

Consider the nuclear reaction

$$^{12}\mathrm{C}(^8\mathrm{Li},\ ^7\mathrm{Li})^{13}\mathrm{C},\ \ Q = 2.913\ \mathrm{MeV} \qquad (4-14)$$

and the inverse reaction

$$^{13}\mathrm{C}(^7\mathrm{Li},\ ^8\mathrm{Li})^{12}\mathrm{C},\ \ Q = -2.913\ \mathrm{MeV} \qquad (4-15)$$

The reaction (4-14) can only take place as a secondary reaction in the laboratory

because a radioactive ^{8}Li beam has to be produced in a preceding stage of reaction. The secondary beam intensity is usually too weak to be measured by a Faraday cup but too intense to be measured by a solid state detector. It can only be measured by some indirect means, for example, by detecting the scattering of the primary beam from the first target. The reaction is also subject to low event rate due to the low intensity of the ^{8}Li beam. For these reasons, measurements of reactions like (4-14) are very involved and experimental data are subject to poor statistics.

In contrast, reaction (4-15) can be carried out readily and precise measurements are permissible since the stable ^{7}Li beam is available with high intensity directly from the accelerator. It is therefore desirable to use this reaction to verify the measurements of reaction (4-14) and hence techniques employed in our radioactive beam experiments. Such verification is based on the detailed balance theorem. Conversely, if the data from the two reactions are precise enough, we can use them to verify the theorem, i.e. test time-reversal invariance.

Let $A + a \rightarrow B + b + Q$ represent the two-body reaction and let $\frac{d\sigma}{d\Omega}(A \rightarrow B)$ be the differential cross section for the reaction preceding from the left to the right and $\frac{d\sigma}{d\Omega}(B \rightarrow A)$ for the other way. According to the detailed balance theorem the ratio of cross sections is (Segré, 1977)

$$\frac{\frac{d\sigma}{d\Omega}(A \rightarrow B)}{\frac{d\sigma}{d\Omega}(B \rightarrow A)} = \frac{p_b^2}{p_a^2} \cdot \frac{(2I_B + 1)(2I_b + 1)}{(2I_A + 1)(2I_a + 1)}. \qquad (4-16)$$

The two reactions are considered in the center-of-mass system and are assumed to occur at the same c.m. energy. The momenta p_a and p_b are measured in that system. I is spin.

The reaction ^{12}C (^{8}Li, ^{7}Li) ^{13}C was first carried out with a projectile kinematic energy of KE_{lab} (^{8}Li) = 14.4 MeV, corresponding to a *total* energy in the center-of-mass E_{cm} = 18659.13 MeV, including the rest energy of the masses. The differential

cross section at $\theta_{cm} = 25.37°$ was determined to be $\frac{d\sigma}{d\Omega}(A \rightarrow B) = (3.1 \pm 0.3)$ mb/sr. To use the detailed balance theorem, the inverse reaction ^{13}C (^{7}Li, ^{8}Li) ^{12}C must have the same E_{cm} which requires that KE_{lab} (^{7}Li) = 17.77 MeV. At KE_{lab} (^{7}Li) = 17 MeV and $\theta_{cm} = 25.37°$, the measured differential cross section is $\frac{d\sigma}{d\Omega}(B \rightarrow A) =$ 1.5 mb/sr. The uncertainty in $\frac{d\sigma}{d\Omega}$ is much smaller than that of the other reaction and is ignored. Listed below are the data from the reactions. The calculated quantities $p_a c$ and $p_b c$ are the momenta times the speed of light.

Reaction ^{12}C (^{8}Li, ^{7}Li) ^{13}C, Q = 2.913 MeV,

KE_{lab} (^{8}Li) = 14.4 MeV, E_{cm} = 18659.13 MeV,

$\frac{d\sigma}{d\Omega}(A \rightarrow B) = (3.1 \pm 0.3)$ mb/sr at $\theta_{cm} = 25.37°$,

$p_b c$ = 313.08 MeV, $(2I_B + 1)(2I_b + 1) = 8$,

$(p_b c)^2 \cdot (2I_B + 1)(2I_b + 1) = 7.84 \times 10^5$ MeV^2.

Reaction ^{13}C (^{7}Li, ^{8}Li) ^{12}C, Q = -2.913 MeV

KE_{lab} (^{7}Li) = 17.77 MeV, E_{cm} = 18659.13 MeV,

$\frac{d\sigma}{d\Omega}(B \rightarrow A) = 1.5$ mb/sr at $\theta_{cm} = 25.37°$,

$p_a c$ = 278.02 MeV, $(2I_A + 1)(2I_a + 1) = 5$,

$(p_a c)^2 \cdot (2I_A + 1)(2I_a + 1) = 3.86 \times 10^5$ MeV^2.

From the data above we have the ratios

$$\frac{\frac{d\sigma}{d\Omega}(A \rightarrow B)}{\frac{d\sigma}{d\Omega}(B \rightarrow A)} = 2.07 \pm 0.20, \qquad (4-17)$$

$$\frac{(p_b c)^2(2I_B + 1)(2I_b + 1)}{(p_a c)^2(2I_A + 1)(2I_a + 1)} = 2.03. \qquad (4-18)$$

The ratios agree with each other well. This agreement serves to verify our measurements of the radioactive beam induced reaction. The $\frac{d\sigma}{d\Omega}(B \rightarrow A)$ for ^{13}C (^{7}Li, ^{8}Li) ^{12}C was actually measured at KE_{lab} (^{7}Li) = 17 MeV and would likely be lower than the cross section at the exact value KE_{lab} (^{7}Li) = 17.77 MeV.

Footnotes to Chapter 4

[1]Le Bow Company, 5960 Mandarin Avenue, Goleta, California 93117.

[2]The Arizona Carbon Foil Company, Inc., 2239 East Kleindale Road, Tucson, Arizona 85719.

CHAPTER 5

FRDWBA CALCULATIONS

The measured angular distributions of the cross sections for (^{8}Li,^{7}Li) transfer reactions have been compared with FRDWBA (Finite Range Distorted Wave Born Approximation) calculations using the computer program FRUCK2 (Kunz, 1983). For the one neutron transfer, we can symbolically write

$$T(P,E)R,\ R = T + n,\ P = E + n, \qquad (5-1)$$

where T, P, E, R and n denote the target, projectile, ejectile, residual nucleus and the transformed neutron, respectively. A_T, A_P, A_E and A_R are the corresponding mass numbers, and Z_T, Z_P, Z_E and Z_R the corresponding atomic numbers. Fig. 5.1 schematically shows the initial and final states of the reaction. In the FRDWBA approximation, the projectile nucleus is treated as a core (consisting of the ejectile) and a neutron in certain nuclear shell model orbit. After transfer, the neutron orbit around the target nucleus T, forming the residual nucleus R. The internal structures of the core and the target T are not relevant in this approximation.

As Fig. 5.1 suggests, the total Hamiltonians in the prior and post forms can be written as

$$H_t(prior) = T_{PT} + T_{nE} + V_{nE} + V_{nT} + V_{ET}, \qquad (5-2)$$

$$H_t(post) = T_{ER} + T_{nT} + V_{nT} + V_{nE} + V_{ET}, \qquad (5-3)$$

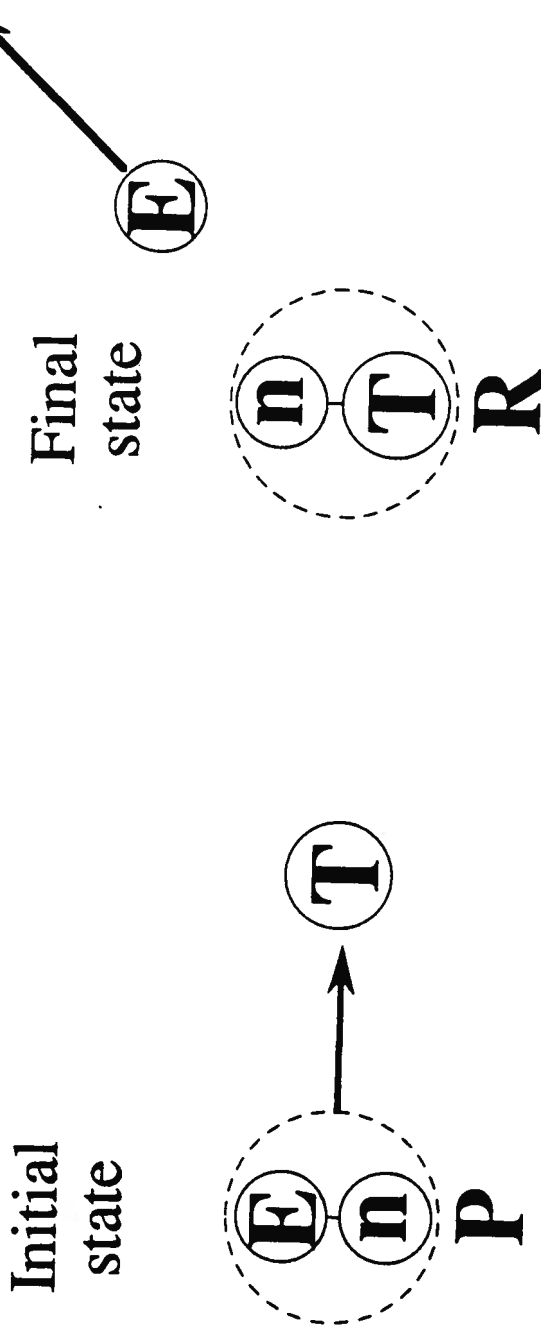

Fig. 5.1 Schematic representation of the one neutron transfer reaction $T(P,E)R$, where $R = T + n, P = E + n$.

where T_{PT} is the operator for the relative kinetic energy of the project-target system, V_{ET} is the relative potential energy of the ejectile-target system, etc. The asymptotic forms of the Hamiltonians for the initial and final states can be written as

$$H_i = T_{PT} + T_{nE} + V_{nE} + V'_{PT}, \qquad (5-4)$$

$$H_f = T_{ER} + T_{nT} + V_{nT} + V'_{ER}, \qquad (5-5)$$

where V'_{PT} and V'_{ER} are the complex optical model potentials. According to Eqs. (5-2) through (5-5), the perturbations in the prior and post forms are

$$H'(prior) = H_t(prior) - H_i = V_{nT} + V_{ET} - V'_{PT}, \qquad (5-6)$$

$$H'(post) = H_t(post) - H_f = V_{nE} + V_{ET} - V'_{ER}, \qquad (5-7)$$

$H'\,(prior)$ and $H'\,(post)$ are completely equivalent. But $H'\,(post)$ is simpler because when assuming $V_{ET} \approx V'_{ER}$ we get

$$H'(post) = V_{nE} \qquad (5-8)$$

This simple choice for the perturbing potential has been used in our FRDWBA calculations. That this choice is reasonable can be seen by considering the inverse $R(E,P)T$ pickup reaction. In this reaction the ejectile E approaches the residual nucleus R and plucks out a neutron to form the projectile P, the ejectile-neutron potential V_{nE} is naturally the interaction that performs the transfer.

According to FRDWBA, the differential cross section for the stripping reaction from the initial state α (entrance channel) to the final state β (exit channel) in the

center-of-mass system can be written as (Enge, 1966; Hodgson, 1971)

$$\frac{d\sigma(\alpha,\beta)}{d\Omega} = \frac{\mu_p \mu_e}{4\pi^2\hbar^4}\frac{k_P}{k_E}|A_{\alpha,\beta}|^2, \qquad (5-9)$$

where μ_P and k_P are the reduced mass and cm wave number of the projectile, and μ_E and k_E are those for the ejectile. $A_{\alpha,\beta}$ is the matrix element of the perturbing potential H'

$$A_{\alpha,\beta} = \int \Psi_f^* H' \Psi_i d\tau_n d\tau_E. \qquad (5-10)$$

The wave functions are

$$\Psi_i = \Phi_i \cdot \phi_i, \qquad (5-11)$$

$$\Psi_f = \Phi_f \cdot \phi_f. \qquad (5-12)$$

Ψ_i and Ψ_f are eigenfunctions of the Hamiltonians (5-4) and (5-5), respectively. Φ_i and Φ_f are the wave functions corresponding to the optical model potential V'_{PT} and V'_{ER}, and describe the center-of-mass motion of the projectile and the ejectile. ϕ_i and ϕ_f are the shell model wave functions corresponding to the real nuclear potentials V_{nE} and V_{nT}, and describe the orbital motion of the neutron in the projectile and in the residual nucleus.

Eq. (5-9) gives the differential cross section for a given entrance channel α and a given exit channel β. For both channels all linear and angular momenta are completely specified. The total differential cross section is obtained by summing the contributions from all angular momenta and spins of the projectile and ejectile consistent with the angular momenta of the transferred neutron. To see the range of summation, we consider the operations on all angular momenta involved in the reaction. Let $\vec{I}_T$ and $\vec{I}_R$ denote the total angular momenta of a given target nucleus

and a given residual nucleus, l_n and s_n the orbital and spin angular momentum of the captured neutron. According to angular momentum conservation we have

$$\vec{I}_R = \vec{I}_T + \vec{l}_n + \vec{s}_n. \qquad (5-13)$$

l_n is thus restricted by the inequality

$$\|I_R - I_T| - \tfrac{1}{2}| \leq l_n \leq I_T + I_R + \tfrac{1}{2} \qquad (5-14)$$

as well as by the fact that l_n must be odd if the target and residual nucleus have opposite parity, or must be even if they have the same parity. Note this restriction on l_n is totally determined by the target and residual nucleus alone, regardless of the projectile and ejectile. The total angular momentum of the neutron is then

$$J_n = l_n \pm \tfrac{1}{2}. \qquad (5-15)$$

The transferred angular momentum l_n is related to the angular momenta of the projectile and ejectile, which are connected by

$$\vec{I}_f + \vec{l}_E + \vec{s}_E = \vec{I}_i + \vec{l}_P + \vec{s}_P,$$

or

$$\Delta\vec{I} = \vec{I}_f - \vec{I}_i = \vec{l}_P - \vec{l}_E + \vec{s}_P - \vec{s}_E \qquad (5-16)$$

where $\vec{l}_P$ and $\vec{s}_P$ are the orbital and spin angular momentum of the projectile, $\vec{l}_E$ and $\vec{s}_E$ are those for the ejectile, and $\vec{I}_f - \vec{I}_i$ is just the vector difference. From Eq. (5-16) we get

$$|\vec{l}_P - \vec{l}_E + \vec{s}_P - \vec{s}_E|_{min} \leq |\Delta\vec{I}| \leq l_P + l_E + s_P + s_E. \qquad (5-17)$$

The quantity $|\Delta\vec{I}|_{max} = (l_P + l_E + s_P + s_E)$ is the maximum angular momentum increase available for the target, without regard to what targets are involved.

Eq. (5-14) determines the possible l_n values that the neutron brings into the residual nucleus and Eq. (5-17) determines the angular momentum available from the projectile. Each l_n must be one of the $|\Delta\vec{I}|$ values. In other words, the angular momentum of the captured neutron must arise from the angular momentum change of the projectile. Since many l_n values can result in the same I_T and I_R, and many combinations of (l_n, l_E, l_P, s_E) can result in the same l_n, the summation for the total differential cross section is carried out over all allowable l_n, all combinations of (l_n, l_E, s_P, s_E) for each l_n.

In passing, radioactive nuclei like ^{8}Li have large ground state angular momentum $[J^\pi(^8\text{Li}) = 2^+]$, this ensures that $|\Delta\vec{I}|_{max}$ is usually large enough to provide all necessary angular momenta for all l_n transfers to be completed. Thus, cross sections for nuclear reactions involving radioactive ions are usually large.

The optical model potentials (V'_{PT} and V'_{ER}) have the following from:

$$U(r) = -V[1 + exp\frac{R - R_v}{a_v}]^{-1} - iW[1 + exp\frac{r - R_w}{a_w}]^{-1} + V_c. \qquad (5-18)$$

The first two terms are of the Saxon-Woods type, and are characterized by being near constant for small r and decaying exponentially at large distances. The second term is imaginary and corresponds to the absorption of the incident waves in nuclear matter. V and W are the real and imaginary potential depth, a_v and a_w are the difusenesses of the potential wells and R_v and R_w are given by

$$R_v = r_v A^{1/3}, \qquad (5-19)$$

$$R_w = r_w A^{1/3}, \qquad (5-20)$$

where $A = A_T$ for the entrance channel, and $A = A_R$ for the exit channel. V_c is the Coulomb potential, and for most practical purposes V_c can be taken as the Coulomb

interaction arising from a point charge incident on a uniform charge distribution:

$$V_c = Z_1 \cdot Z_2 e^2(3 - r^2/R_c^2)/(2R_c) \text{ for } r \leq R_c$$
$$= Z_1 \cdot Z_2 e^2/r \qquad \text{for } r > R_c, \qquad (5-21)$$

where

$$R_c = 1.3(A_1^{1/3} + A_2^{1/3}) \text{ fm.} \qquad (5-22)$$

The subscripts 1 and 2 represent two interacting particles. For the entrance channel (1,2) = (P,T), and for the exit channel (1,2) = (E,R).

The potentials (V_{nE} and V_{nT}) for the bound state wave functions (neutron in the projectile and in the residual nucleus) consists of a real Saxon-Woods potential and a spin-orbit coupling term V_s:

$$U_b(r) = -V_b[1 + exp\frac{r - R_b}{a_b}] + V_s, \qquad (5-23)$$

where the subscript b refers to "bound state", $R_b = r_b A_T^{1/3}$ for the residual nucleus and $R_b = r_b A_E^{1/3}$ for the projectile. $U_b(r)$ does not contain the imaginary part because no absorption occurs for stable states. The Coulomb potential does not enter $U_b(r)$ because the neutron is electrically neutral. In our one neutron transfer FRDWBA calculations, the geometry parameters were taken to be $r_b = 1.25$ fm, $a_b = 0.75$ fm, and V_b was determined by the binding energy of the neutron. The spin-orbit parameter used was $\lambda = 25$.

Table 5.1 lists the optical model potential parameters used in our FRDWBA calculations. ^{10}Be* is ^{10}Be in its first excited state of 3.368 MeV. The parameters have been adopted from literature on nuclear reactions involving particles similar to particles involved in our experiments, with W and r_w modified for the appropriate energies.

Table 5.1. Optical model potential parameters

Reaction channel	KE_{lab} (MeV)	V (MeV)	r_v (fm)	a_v (fm)	W (MeV)	r_w (fm)	a_w (fm)
$^{12}C + ^{8}Li$	12.8	245.0	1.210	0.759	5.89	2.049	0.909
$^{13}C + ^{7}Li$	15.7	248.2	1.210	0.755	6.42	2.038	0.944
$^{13}C + ^{8}Li$	13.8	187.8	1.208	0.824	5.25	2.220	0.770
$^{14}C + ^{7}Li$	19.9	166.4	1.208	0.763	4.75	2.208	0.950
$^{9}Be + ^{8}Li$	13.1	173.1	1.190	0.780	4.06	2.560	0.924
$^{10}Be + ^{7}Li$	17.8	173.2	1.210	0.802	4.11	2.210	0.947
$^{10}Be^{*} + ^{7}Li$	14.5	173.2	1.210	0.802	4.11	2.210	0.947
$^{2}H + ^{8}Li$	12.8	118.0	0.886	0.907	12.60	2.770	0.660
$^{3}H + ^{7}Li$	17.0	118.0	0.886	0.907	12.60	2.770	0.660

From analyses of many sets of optical model parameters, it has been found (Vineyard, 1984) that V, r_v, a_v and a_w in Eq. (5-18) are essentially independent of energy, but W and r_w depend linearly on energy:

$$W = a_1 + k_1 \cdot KE_{lab}$$

$$r_w = a_2 + k_2 \cdot KE_{lab}.$$

Specifically, W and r_w for the $^{12}C + ^{6}Li$ scattering channel are

$$W = 1.03 \text{ MeV} + k_1 \cdot KE_{lab}, \qquad (5-24)$$

$$r_w = a_2 + k_2 \cdot KE_{lab}. \qquad (5-25)$$

For example, it has been determined that $W = 12.7$ MeV and $r_w = 2.00$ fm for the $^{13}C + ^{7}Li$ scattering channel at KE_{lab} (^{7}Li) = 34 MeV (Schumacher, 1973). Inserting these values into Eqs. (5-24) and (5-25) yields $k_1 = 0.343$ and $a_2 = 2.071$ fm, which lead to

$$W = 1.03 \text{ MeV} + 0.343 KE_{lab},$$

$$r_w = 2.071 \text{ fm} + 0.0021 \text{ fm/MeV} \cdot KE_{lab}.$$

In our experiments, ^{7}Li from $^{12}C(^{8}Li, ^{7}Li)^{13}C$ has energy $KE_{lab}(^{7}Li) = 15.7$ MeV. According to the last two equations, the proper W and r_w should be

$$W = 6.42 \text{ MeV},$$

$$r_w = 2.038 \text{ fm}.$$

These two parameters have been included in the second reaction channel in Table 5.1. Usually the existing parameters are for similar reactions with energies different than energies used in our experiments. The parameters W and r_w should be adjusted via Eqs. (5-24) and (5-25), while other parameters can be kept unchanged.

The optical model potential parameters for ^{12}C(^{8}Li,^{7}Li)^{13}C have been taken from those for the inverse reaction ^{13}C(^{7}Li,^{8}Li)^{12}C (Schumacher, 1973). For the reaction ^{13}C(^{8}Li,^{7}Li)^{14}C, the parameters for ^{12}C + ^{7}Li and ^{13}C + ^{7}Li (Schumacher, 1973) have been used for the entrance and exit channel, respectively. This adoption assumes that the potential parameters for ^{14}C + ^{7}Li and ^{13}C + ^{7}Li, for example, are the same. The potentials are still different because R_v and R_w depend on $A^{1/3}$.

The reactions ^{9}Be(^{8}Li,^{7}Li)^{10}Be and ^{9}Be(^{8}Li,^{7}Li)^{10}Be* share the same optical model parameters, which have been taken from the parameters for ^{9}Be(^{7}Li,^{6}Li)^{10}Be at $KE_{lab}(^{7}\text{Li}) = 34$ MeV (Kemper, 1977) with W and r_w modified according to Eqs. (5-24) and (5-25). It has been assumed that the ^{9}Be + ^{8}Li interaction and the ^{9}Be + ^{7}Li interaction, etc. are not much different. However, the cross sections for ^{9}Be(^{8}Li,^{7}Li)^{10}Be and ^{9}Be(^{7}Li,^{6}Li)^{10}Be can still be very different because the former has much greater Q-value and there is greater ground state angular momentum in the projectile.

The parameters for ^{1}H(^{7}Li,^{8}Li)^{2}H at $KE_{cm} = 9.3$ MeV (Schiffer, 1967) have been used for ^{2}H(^{8}Li,^{7}Li)^{3}H with the values of W and r_w have been adjusted to fit the transfer data angular distribution.

The results of the FRDWBA calculations based on the optical model potential parameters in Table 5.1 are displayed in Figs. 4-12 to 4-16 as solid curves. The gen-

eral characteristics of the observed (^{8}Li,^{7}Li) differential cross sections (shape and magnitude) are reproduced by the calculations with normalization using the spectroscopic factors S presented in Table 5.2. The latter have an estimated uncertainty of ±5%.

Table 5.2 Spectroscopic factors for the (^{8}Li,^{7}Li) reactions

Reaction	S	S_{CK}
$^{12}C \rightarrow {}^{13}C$	1.1	0.6
$^{13}C \rightarrow {}^{14}C$	0.89	1.4
$^{9}Be \rightarrow {}^{10}Be$	0.83	1.2
$^{9}Be \rightarrow {}^{10}Be^*$	1	1.3
$^{2}H \rightarrow {}^{3}H$	1	–

The curves fit the data points fairly well for ^{12}C(^{8}Li,^{7}Li)^{13}C and ^{13}C(^{8}Li,^{7}Li)^{14}C. While for ^{9}Be(^{8}Li,^{7}Li)^{10}Be and ^{9}Be(^{8}Li,^{7}Li)^{10}Be* (3.368 MeV) the fits are tolerable but the data points have large uncertainties. Only three data points have been obtained for ^{2}H(^{8}Li, ^{7}Li)^{3}H because of the kinematic constraint on the maximum angle and the experimental limit on the minimum angle. These few data points nonetheless serve to normalize the calculated distribution since the shape of the curve is fairly fixed and not sensitive to variations around reasonably chosen optical model parameters.

The spectroscopic factor is defined as the ratio of the measured differential cross section to the cross section calculated by FRDWBA:

$$S \equiv (d\sigma/d\Omega)_{exp}/(d\sigma/d\Omega)_{FRDWBA}.$$

The factors S in Table 5.2 have been chosen in such a way that $S*(d\sigma/d\Omega)_{FRDWBA}$ best fits $(d\sigma/d\Omega)_{exp}$. S_{CK} factors in the last column of the table are the spectroscopic factors from nuclear shell model calculations (Cohen, 1967). S and S_{CK} are seen to be comparable to each other.

The FRDWBA calculations are based on the assumption that the transferred neutron goes into a single particle state, i.e. a shell model state, and that the projectile is converted into the ejectile immediately after being stripped of its neutron. In other words, FRDWBA assumes that the (^{8}Li,^{7}Li) reaction is a one-step, *direct* transfer process. That all S factors in Table 5.2 are close to unity implies that all the (^{8}Li,^{7}Li) transfers are essentially direct reactions. This is in contrast with non-direct, compound nuclear reactions, as usually assumed in most astrophysical nucleosynthesis calculations involving low KE_{cm} radioactive nuclei.

Of particular astrophysical interest is the reaction ^{2}H(^{8}Li,^{7}Li)^{3}H, since it competes with ^{4}He(^{8}Li,^{11}B)n. The latter is in the reaction chain responsible for synthesizing isotopes with $A > 12$ (see Chapter 1, Section A). Nuclear reactions usually take place at low energies in many astrophysical environments. A FRDWBA curve for the energy dependence of ^{2}H(^{8}Li,^{7}Li)^{3}H total cross section σ_{tot} has been plotted in the range of KE_{cm} = 1 MeV to 4 MeV (Fig. 5.2). Such dependence has been calculated by changing the kinetic energy of the projectile ^{8}Li and keeping other parameters unchanged. As Fig. 5.2 shows, σ_{tot} decreases monotonically with decreasing energy. In our experiments, ^{2}H(^{8}Li,^{7}Li)^{3}H was measured at KE_{lab} (^{8}Li) = 12.8 MeV, or KE_{cm} = 2.56 MeV, and the cross section was σ_{tot} = 47.0 mb. The curve thus serves to predict cross sections at lower energy. For example, at KE_{cm} = 1 MeV, the curve shows σ_{tot} = 34.2mb. The cross sections in the above energy range are of considerable magnitude. Thus, we could say that ^{2}H(^{8}Li,^{7}Li)^{3}H should effectively compete with ^{4}He(^{8}Li,^{11}B)n and affect the production rates of isotopes of $A > 12$, although the cross section for ^{4}He(^{8}Li,^{11}B)n has not been measured.

Most nuclear reactions involving radioactive ions have large and positive Q-values. To see how the reaction rates depend on Q-values, the total cross sections for ^{2}H(^{8}Li,^{7}Li)^{3}H and ^{12}C(^{8}Li,^{7}Li)^{13}C have been calculated and plotted versus various

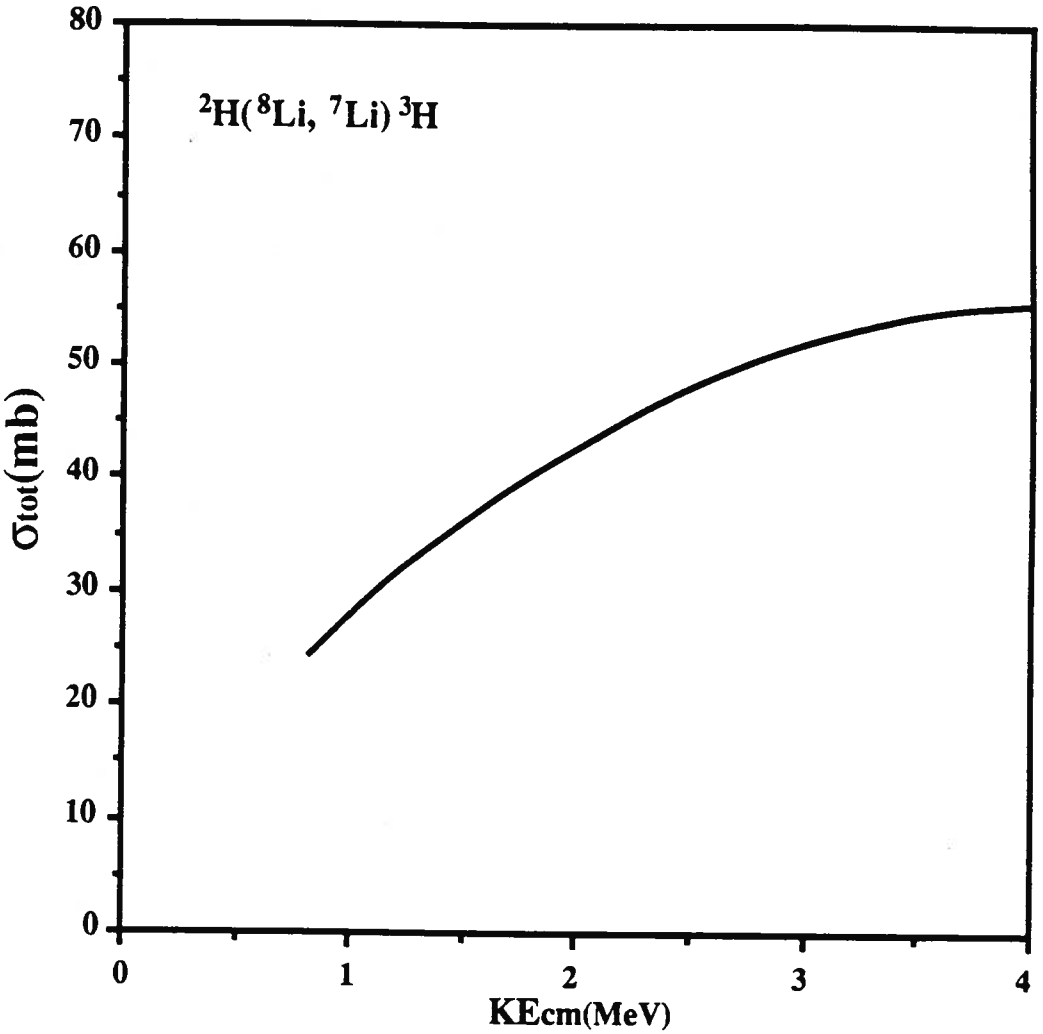

Fig. 5.2 Energy dependence of ^{2}H(^{8}Li,^{7}Li)^{3}H total cross section.

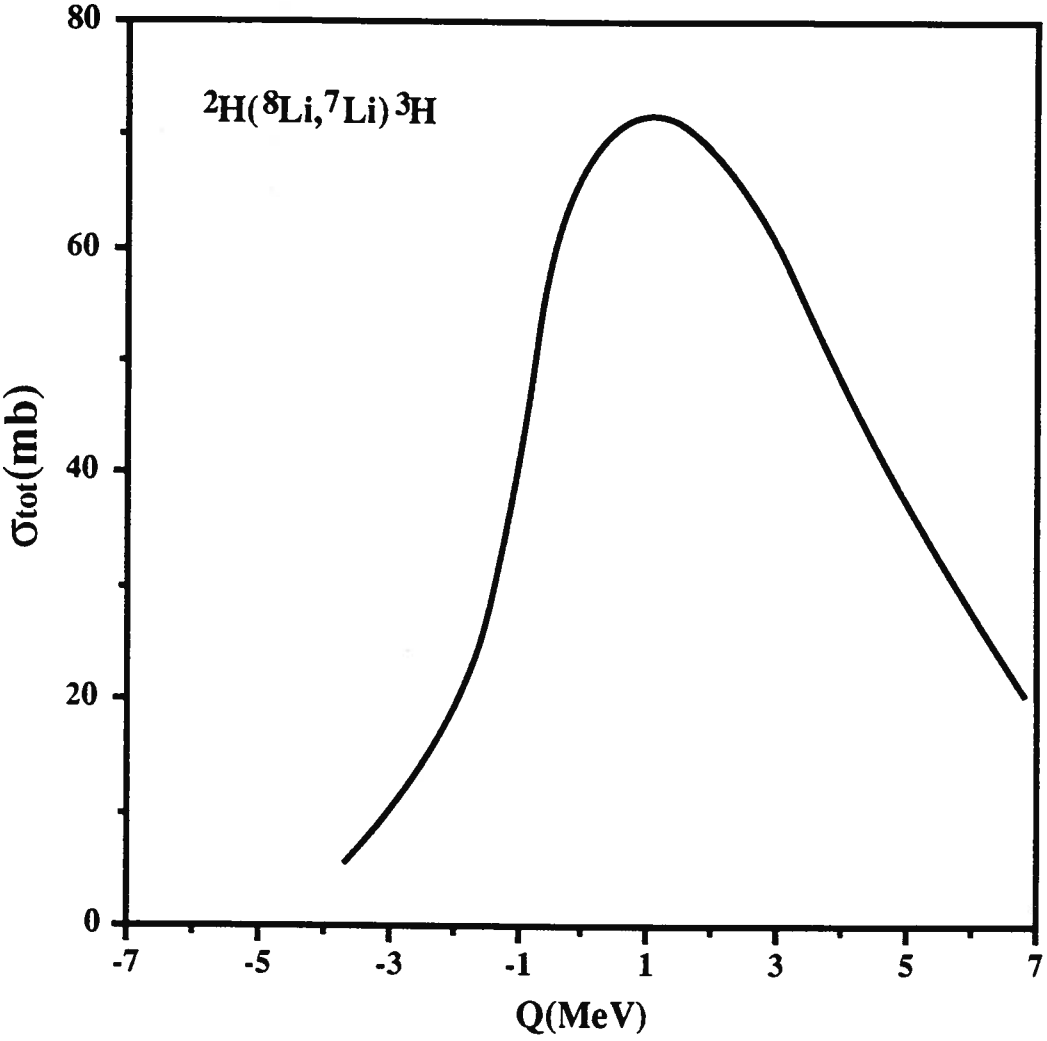

Fig. 5.3 Q-value dependence of ^{2}H(^{8}Li,^{7}Li)^{3}H total cross section at $\overline{KE}_{lab}$ (^{8}Li) = 12.8 MeV.

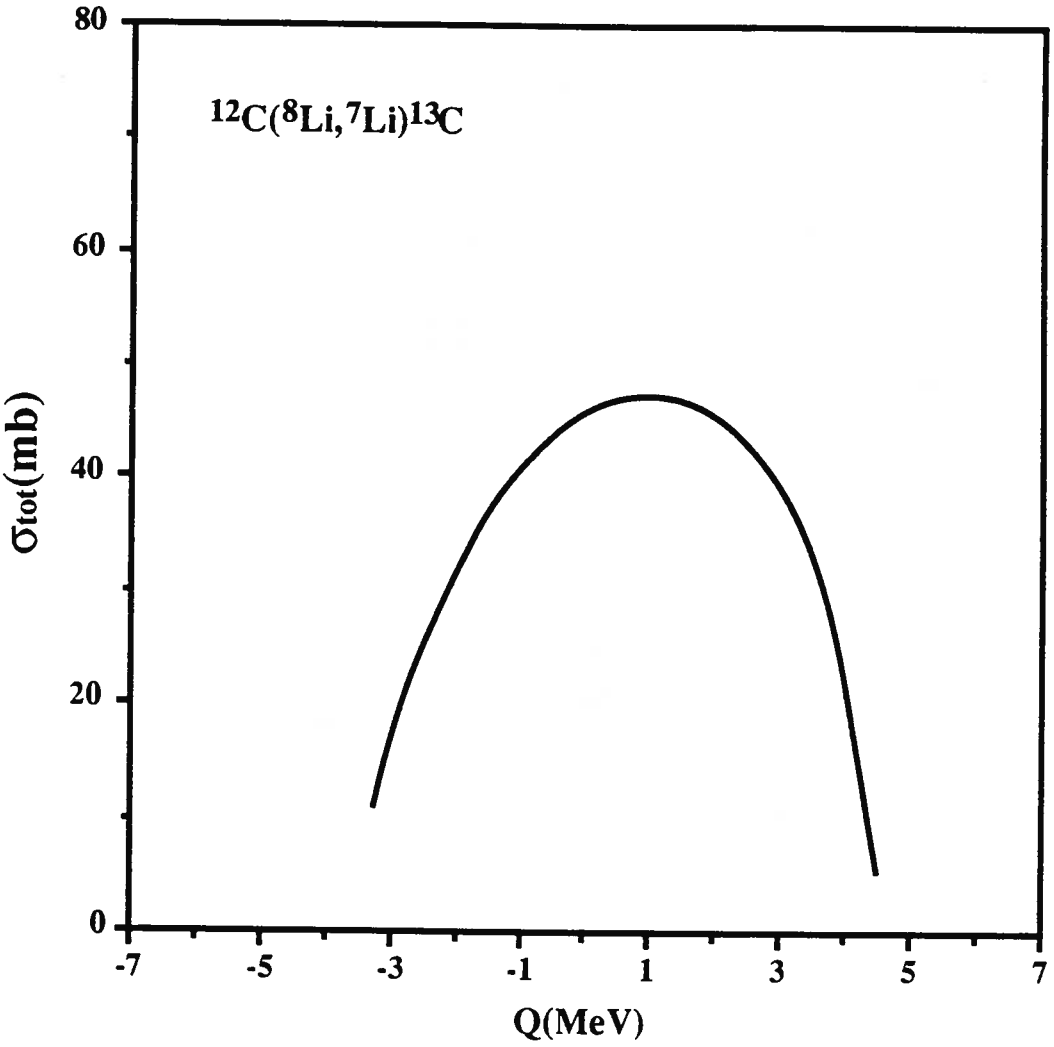

Fig. 5.4 Q-value dependence of $^{12}C(^{8}Li,^{7}Li)^{13}C$ total cross section at $\overline{KE}_{lab}$ (^{8}Li) = 12.8 MeV.

Q-values, as shown in Figs. 5.3 and 5.4. Since the sum of the Q-value and the binding energy (BE) of the last neutron in ^{8}Li is a constant, when Q changes, the BE must also change according to $\Delta BE = -\Delta Q$. As can be seen from either of the curves, σ_{tot} reaches its maximum at $Q \approx 0$ MeV, consistent with the prediction that $Q(optimal) = (Z_1Z_2/Z_3Z_4 - 1)KE_{cm}$ (Burcham, 1979). More significantly, σ_{tot} decays on the negative Q-value side much faster than on the positive side. The (^{8}Li,^{7}Li) reactions usually have Q-values on the positive side and hence have large cross sections. Positive Q-values are particularly important at $KE_{cm} \approx$ coulomb barrier. Without the positive Q-values, the cross section would be very small. For comparison of reactions with different Q-values, Table 5.3 contains the calculated total cross sections for (^{8}Li,^{7}Li) on various targets and (^{7}Li,^{6}Li) on the same targets at the same center-of-mass energies. The quantity σ_{tot} for (^{8}Li,^{7}Li) is usually greater than σ_{tot} for (^{7}Li,^{6}Li), with the exception that (^{7}Li,^{6}Li) reactions have greater σ_{tot} when they have near zero Q-values. This exception can be qualitatively explained by the curves in Figs. 5.3 and 5.4. The same optical model parameters for (^{8}Li,^{7}Li) in Table 5.1 have been used for the corresponding (^{7}Li,^{6}Li) reaction.

Table 5.3 Comparison of calculated cross sections for (^{8}Li,^{7}Li) and (^{7}Li,^{6}Li)

Reaction	Q (MeV)	KE_{cm} (MeV)	σ_{tot} (mb)
^{12}C(^{8}Li,^{7}Li)^{13}C	2.913	7.7	39.7
^{12}C(^{7}Li,^{6}Li)^{13}C	-2.304	7.7	24.6
^{13}C(^{8}Li,^{7}Li)^{14}C	6.143	8.3	19.9
^{13}C(^{7}Li,^{6}Li)^{14}C	0.926	8.3	15.0
^{9}Be(^{8}Li,^{7}Li)^{10}Be	4.779	6.9	25.7
^{9}Be(^{7}Li,^{6}Li)^{10}Be	-0.438	6.9	73.6
^{9}Be(^{8}Li,^{7}Li)^{10}Be*	1.411	6.9	66.2
^{9}Be(^{7}Li^{6}Li)^{10}Be*	-3.806	6.9	17.7
^{2}H(^{8}Li,^{7}Li)^{3}H	4.224	2.6	47.0
^{2}H(^{7}Li,^{6}Li)^{3}H	-0.993	2.6	139

In nucleosynthesis, most nuclear reactions take place at low KE_{cm}, i.e. $KE_{cm} <$ 1 MeV or $T \approx 10^9 K$. However, as the excitation function (dependence of total cross

section on energy, see Fig. 5.2) indicates, unlike stable-beam reactions, the total cross sections for RIB-induced reactions usually do not vanish near zero energy. This can be largely attributed to the positive Q-values of RIB reactions.

The present experiments demonstrate that the (^{8}Li, ^{7}Li) reaction is the dominant ^{8}Li-induced transfer reaction and stronger than (^{8}Li, ^{9}Be) and other nucleon transfer reactions. Also, comparison of our experimental data with FRDWBA calculations suggests that the (^{8}Li, ^{7}Li) is essentially a direct transfer reaction, instead of compound nuclear reaction, as is normally assumed in nucleosynthesis calculations.

CHAPTER 6

CONCLUSION

The University of Michigan Superconducting Solenoid Radioactive Ion Beam Facility has been shown to be an *optimal* instrument for experimental studies of radioactive-beam induced nuclear reactions, including reactions of astrophysical interest. The solenoid's simple optical properties makes it easy to predict trajectories of particles and its relatively large solid angle facilitates effective collection of radioactive ions. This makes it possible to measure reactions with differential cross sections on the order of a millibarn/sr or less.

Improvements of the facility may include introducing proper electric lenses to suppress impurity ions and adding more complicated electromagnetic devices to reduce the angular spread of the secondary beams. Heavier mass production targets may also be desired to minimize the beam energy spreads.

Our measured cross sections and FRDWBA calculations show that direct reactions are significant in the (^{8}Li,^{7}Li) transfers, and that the cross section for ^{2}H(^{8}Li,^{7}Li)^{3}H may be large enough to reduce the synthesis rates of isotopes heavier than ^{12}C in the nonstandard Big Bang model and must therefore be considered. In contrast, the ^{2}H(^{8}Li, ^{9}Li) and ^{2}H(^{8}Li, ^{9}Be) reactions appear to be less important.

Partly based on the success of the project presented in this dissertation, a much larger superconducting solenoid of 40 cm bore, 100 cm long and 5 to 7 Tesla central

field is being constructed. This solenoid will be used to build another radioactive beam facility at the National Superconducting Cyclotron Laboratory (NSCL) at Michigan State University. The new facility will have much greater focusing power and will produce secondary beams of much higher intensities and energies. This will permit study of radioactive-beam induced reactions throughout the periodic table which should provide new insights on nuclear reactions and nuclear models which have not been previously possible using stable nuclear beams.

APPENDICES

APPENDIX A

TWO-BODY COLLISION

A.1 Kinematics Shift

In a two-body collision process, a particle of mass m_2, at rest in the laboratory frame, is struck by a particle of mass m_1, momentum $\vec{p}_1$ and kinetic energy k_1. The two initial particles are then transformed into two others of mass m_3 and m_4 (Fig. A.1).

According to energy and momentum conservation laws, one obtains

$$\sqrt{(p_1c)^2+(m_1c^2)^2}+m_2c^2=\sqrt{(p_3c)^2+(m_3c^2)^2}+\sqrt{(p_4c)^2+(m_4c^2)^2}, \quad (A-1)$$

$$p_1 = p_3cos\theta_3 + p_4cos\theta_4, \quad (A-2)$$

$$p_3sin\theta_3 = p_4sin\theta_4. \quad (A-3)$$

The last two equations amount to a vector equation,

$$\vec{p}_1=\vec{p}_3+\vec{p}_4 \quad (A-4)$$

After some manipulations, one gets a quadratic equation for the unknown (p_3c):

$$A\cdot(p_3c)^2+B\cdot(p_3c)+c=0, \quad (A-5)$$

where

$$A = 1-(p_1c)\ cos\theta_3/E_t,$$

$$B = -[E_t^2+(m_3c^2)^2-(m_4c^2)^2-(p_1c)^2](p_1c)\ cos\theta_3/E_t^2,$$

$$C = (m_3C^2)^2-[E_t^2+(m_3c^2)^2-(m_4c^2)^2-(p_1c)^2]/4E_t^2.$$

and $E_t = k_1+(m_1+m_2)c^2$ is the total energy of the two-body system. The solution

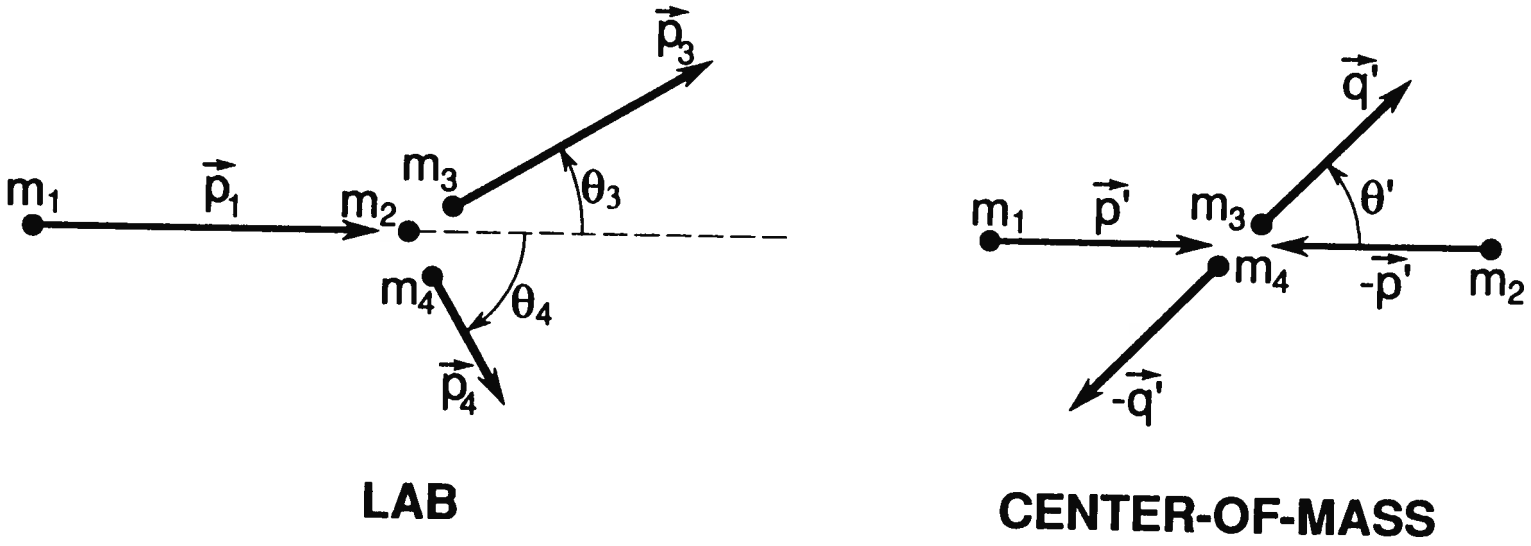

Fig. A.1 Schematic diagrams of the nuclear reaction $m_1 + m_2 \rightarrow m_3 + m_4$ in LAB and cm systems.

of Eq. (A-5) is

$$(p_3c) = \frac{-B \pm (B^2 - 4AC)^{1/2}}{2A}. \qquad (A-6)$$

So (p_3c) is double-valued. The physical significance of (p_3c) requires that it be real and positive. If $[-B - (B^2 - 4AC)^{1/2}] < 0$, then only the plus sign is allowed. However, if $[-B - (B^2 - 4AC)^{1/2}] > 0$, then both plus and minus signs must be considered. Each of them results in a physically significant value of (p_3c).

Once (p_3c) is known, derivations of other related quantities are straightforward, as follows:

$$(p_4c) = [(p_1c)^2 + (p_3c)^2 - 2(p_1c)(p_3c)cos\theta_3], \qquad (A-7)$$

$$sin\theta_4 = (p_3c)sin\theta_3/(p_4c), \qquad (A-8)$$

$$k_4 = [(p_4c)^2 + (m_4c^2)^2]^{1/2} - m_4c^2, \qquad (A-9)$$

$$k_3 = [(p_3c)^2 + (m_3c^2)^2]^{1/2} - m_3c^2. \qquad (A-10)$$

The last two equations follow from the definition of kinetic energy while Eqs. (A-7) and (A-8) are direct results of (A-4).

Generally, the quantities on the left hand sides of Eqs. (A-6) through (A-10) depend on the angle θ_3. Such dependence is called the kinematic shift and is sometimes an undesired effect since it can degrade the energy resolution in a detector. The effect is small if the target is much heavier than the projectile. However, if the target mass is comparable with, or even smaller than the projectile mass, the effect can be significant.

As an example, Fig. A.2 shows the dependence of ^{8}Li energy on the emerging angle θ_3. $E(^8\mathrm{Li})$ from the reaction $^2\mathrm{H}(^7\mathrm{Li},^8\mathrm{Li})^1\mathrm{H}$ decreases with angle drastically, since the projectile is heavier than the target (inverse kinematics). $E(^8\mathrm{Li})$ from

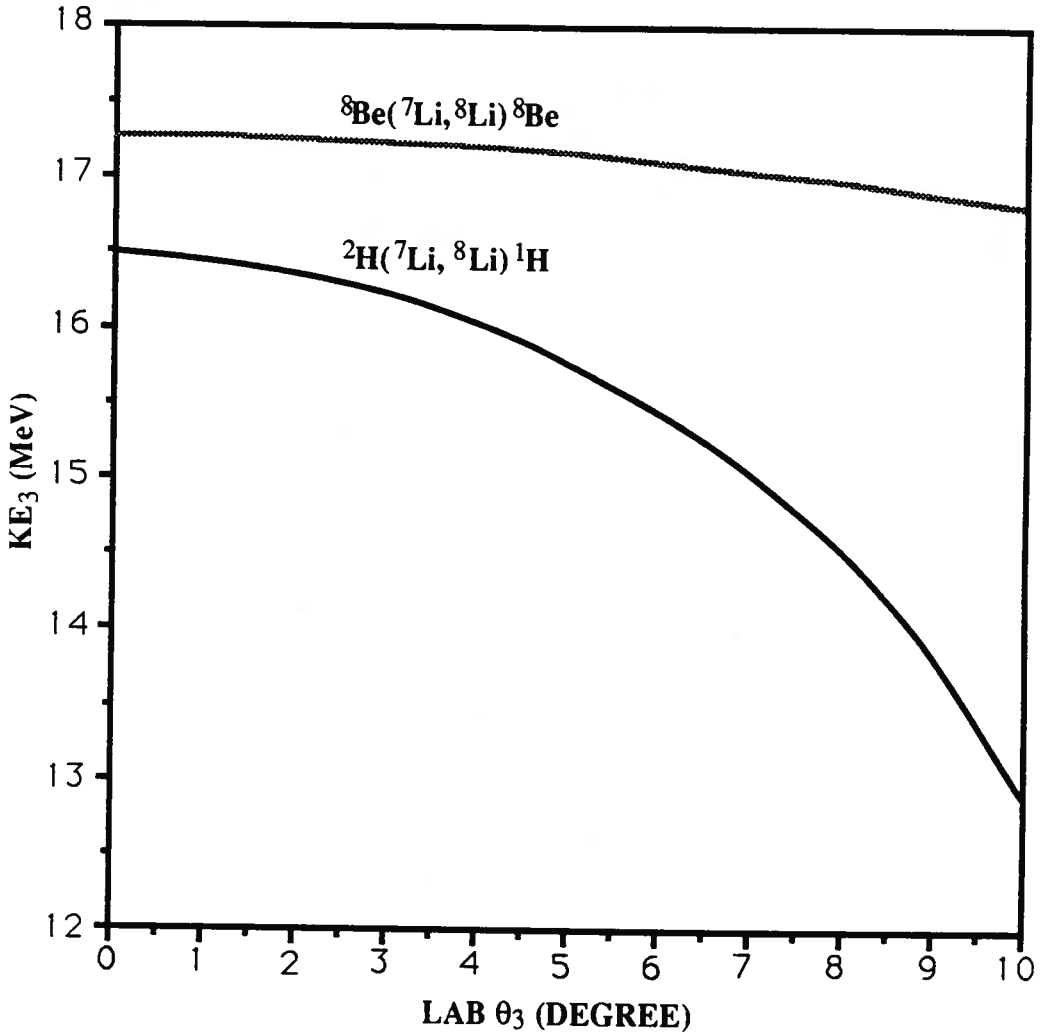

Fig. A.2 Dependence of ejectile energy KE_3 on the angle θ_3 for ^{9}Be(^{7}Li,^{8}Li)^{8}Be and ^{2}H(^{7}Li,^{8}Li)^{1}H at KE_{lab} (^{7}Li) = 17 MeV.

^{9}Be(^{7}Li,^{8}Li)^{8}Be does not vary quickly with θ_3. Therefore, as long as kinematics is concerned, ^{9}Be(^{7}Li,^{8}Li)^{8}Be is a better reaction to produce an ^{8}Li beam since such beam will have smaller energy spread and hence better energy resolution.

A.2 Conversion of Scattering Angles and Solid Angles

In the nuclear reaction, shown in Fig. A.1, the emerging angle $\theta \equiv \theta_3$ of the ejectile as seen in the laboratory frame is different than the angle $\theta' \equiv \theta'_3$ as seen in the center-of-mass frame. They can be converted to each other through the equations (Jackson, 1975).

$$tan\theta' = \frac{sin\theta}{\gamma_{cm}(cos\theta - \beta_{cm}/\beta_3)}, \qquad (A-11)$$

where

$$\beta_{cm} = \frac{p_1 c}{k_1 + (m_1 + m_2)c^2} = \frac{p_1 c}{E_t}, \qquad (A-12)$$

$$\beta_3 = \frac{p_3 c}{[(p_3 c)^2 + (m_3 c^2)^2]^{1/2}} = \frac{p_3 c}{E_3}, \qquad (A-13)$$

$$\gamma_{cm} = \frac{E_t}{[(m_1^2 + m_2^2)c^4 + 2m_2 c^2(k_1 + m_1 c^2)]^{1/2}}. \qquad (A-14)$$

For a finite mass target, $\theta' > \theta$ except at $\theta = 0$ and 180°, where $\theta' = \theta$ (Fig. A.3).

Eq. (A-11) is general in that it is relativistically valid and it applies to both elastic and inelastic reactions. It has been used in our data analyses. For non-relativistic elastic scatterings (i.e. $Q = 0$) a much simpler conversion formula exists (Goldstein, 1980):

$$tan\theta = \frac{sin\theta'}{cos\theta' + \frac{m1}{m2}}. \qquad (A-15)$$

Conversion of solid angles is also necessary for the calculation of differential cross sections in the cm frame. A solid angle defined by $\phi_1 \leq \phi \leq \phi_2$ and $\theta_1 \leq \theta \leq \theta_2$

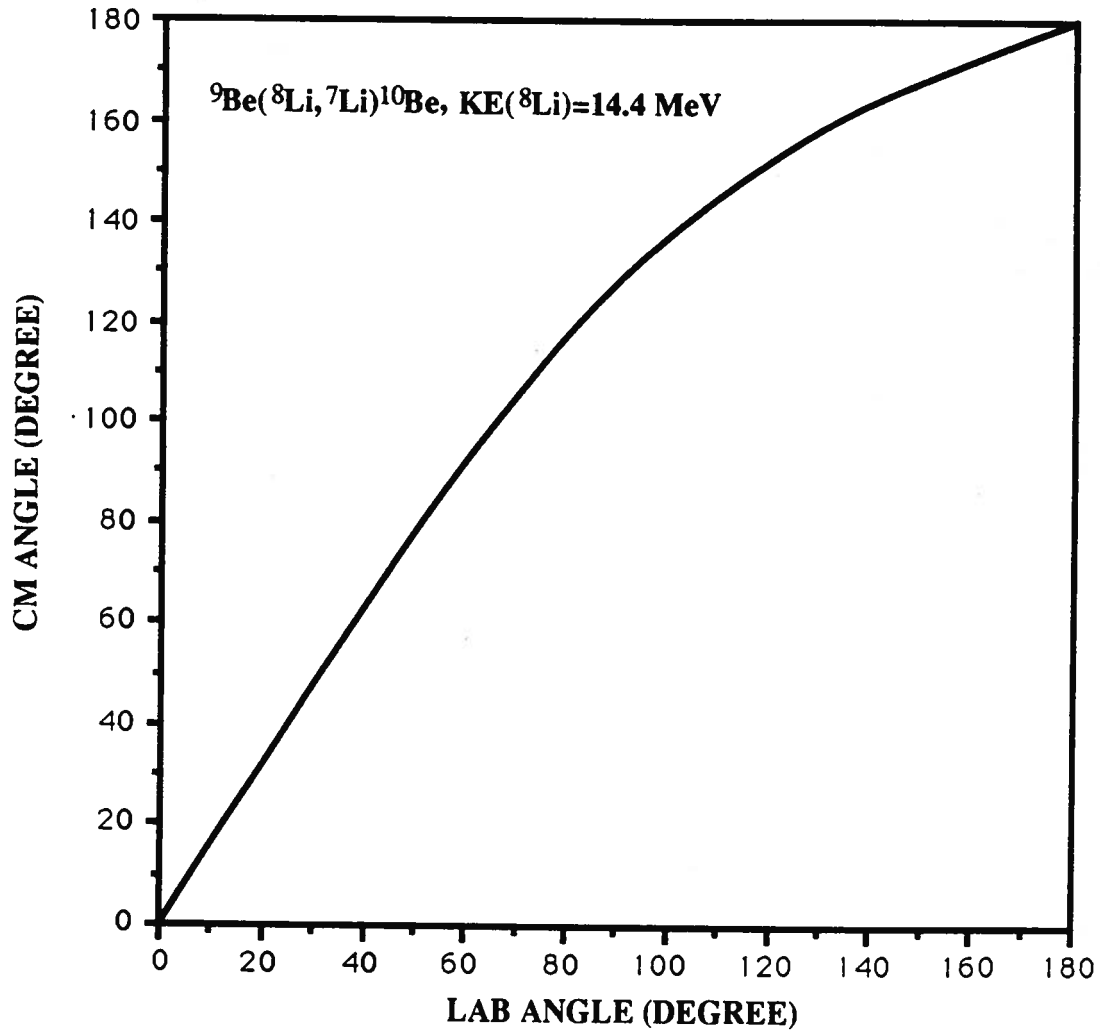

Fig. A.3 Curve of lab to cm angle conversion for ^{9}Be(^{8}Li,^{7}Li)^{10}Be at KE_{lab} (^{8}Li) = 14.4 MeV.

can be written as

$$\Delta\Omega = \int_{\phi_1}^{\phi_2} d\phi \int_{\theta_1}^{\theta_2} sin\theta d\theta$$
$$= (\phi_2 - \phi_1)(cos\theta_1 - cos\theta_2). \qquad (A-16)$$

The angle ϕ does not change from the laboratory frame to the cm frame. So the ratio of solid angles in two different frames is

$$\frac{\Delta\Omega_{cm}}{\Delta\Omega_{lab}} = \frac{cos\ \theta_1' - cos\ \theta_2'}{cos\theta_1 - cos\theta_2}, \qquad (A-17)$$

where $\Delta\Omega_{cm}$ is the solid angle in the cm frame and $\Delta\Omega_{lab}$ is the solid angle in the laboratory frame.

The conversion between infinitesimal solid angles in the two coordinate frames can be written explicitly via Eq. (A-11) and the definitions $d\Omega_{lab} = sin\theta d\theta d\phi$ and $d\Omega_{cm} = sin\theta' d\theta' d\phi'$. We therefore have

$$sin\theta' d\theta' = \frac{\gamma_{cm}(1 - cos\theta\beta_{cm}/\beta_3)}{[\gamma_{cm}^2(cos\theta - \beta_{cm}/\beta_3)^2 + sin^2\theta]^{3/2}} \cdot sin\theta d\theta. \qquad (A-18)$$

Since $d\phi' = d\phi$, it follows that

$$d\Omega_{cm} = \frac{\gamma_{cm}(1 - cos\theta\beta_{cm}/\beta_3)}{[\gamma_{cm}^2(cos\theta - \beta_{cm}/\beta_3)^2 + sin^2\theta]^{3/2}} \cdot d\Omega_{lab}. \qquad (A-19)$$

APPENDIX B

COMPUTER RAY TRACING

Since the solenoid, and hence its magnetic field, are cylindrically symmetric, it is most convenient to use the cylindrical coordinate system (r, ϕ, z), where $r = (x^2 + y^2)^{1/2}$, $\phi = arctan(x/y)$ and the z-axis corresponds to the solenoid axis of symmetry. If the origin of the system is chosen to be the center of the solenoid, then the z-component of the magnetic field on the axis is given by

$$B_{z0}(z) = k_1 \cdot I \left\{ \frac{z + l_m/2}{[r_m^2 + (z + l_m/2)^2]^{1/2}} - \frac{z - l_m/2}{[r_m^2 + (z - l_m/2)^2]^{1/2}} \right\}. \qquad (B-1)$$

The off-axis fields given in their series forms are (Cosslet, 1950)

$$B_z(r, z) = \sum_{n=0}^{\infty} \frac{(-1)^n}{n!} \left(\frac{r}{2}\right)^{2n} B_{zo}^{(2n)}(z), \qquad (B-2)$$

$$B_r(r, z) = \sum_{n=0}^{\infty} \frac{(-1)^{n+1}}{n!(n+1)!} \left(\frac{r}{2}\right)^{2n+1} B_{zo}^{(2n+1)}(z), \qquad (B-3)$$

where $B_{zo}^{(n)}(z)$ is the nth derivative of the axial field given by (B-1).

The general equation of motion for a non-relativistic particle in the magnetic field is

$$\frac{d\vec{v}}{dt} = \vec{a} = \frac{q}{m} \vec{v} \times \vec{B}, \qquad (B-4)$$

where q, m, $\vec{v}$ and $\vec{a}$ are the particle's charge, mass, velocity and acceleration, respectively.

In the Gaussian approximation, only the $n = 0$ terms of the fields are considered.

$$B_z(r, z) = B_{z0}(z), \qquad (B-5)$$

$$B_r(r,z) = -\frac{r}{2}\frac{dB_{z0}(z)}{dz}. \qquad (B-6)$$

And the equations of motion are simple:

$$\frac{d^2r}{dz^2} = \frac{r}{4}\frac{B_{zo}^2}{(B\rho)^2}, \qquad (B-7)$$

$$\frac{d\phi}{dz} = -\frac{1}{2}\frac{B_{zo}}{B\rho}. \qquad (B-8)$$

Eqs. (B-7) and (B-8) result in the Gaussian focal length

$$f = \frac{4(B\rho)^2}{\int_{-\infty}^{\infty} B_{zo}^2 dz} = \frac{4(B\rho)^2}{\overline{B^2}L}. \qquad (B-9)$$

The Gaussian approximation is good only for paraxial rays. For non-paraxial rays, high order terms of the fields must also be taken into account. The equation of motion (B-4) then becomes very complicated and seeking analytical solutions is impractical. In this case, we can resort to numerical methods with the aid of computers. One of the numerical approaches is computer ray tracing (Gould, 1988; Merill, 1976). In this approach, many terms of the magnetic fields can be included and calculation precision up to computer round-off error can be achieved. Trajectories can be plotted readily and numerical values of momentum dispersion and spherical aberration can be obtained.

To illustrate the ray tracing method, we assume that the position $\vec{x}_o$ and velocity $\vec{v}_o$ are known at the initial time t_o. The acceleration $\vec{a}_o$ at this instance is

$$\vec{a}_o = \frac{q}{m}\,\vec{v}_o \times \vec{B}\,(r_o, z_o)$$

After a short time interval Δt, we have

$$\vec{x}_1 = \vec{x}_o + \vec{v}_o\,\Delta t + \frac{1}{2}\,\vec{a}_o\,\Delta t^2,$$

$$\vec{v}_1 = \vec{v}_o + \vec{a}_o\,\Delta t.$$

From these new values of variables, we can calculate the new acceleration $\vec{a}_1$:

$$\vec{a}_1 = \frac{q}{m} v_1 \times \vec{B}\,(r_1,\ z_1).$$

By repetition of this procedure n times, we can calculate $\vec{x}$ and $\vec{v}$ at time $t_n = t_o + n\Delta t$.

$$\vec{x}_n = \vec{x}_{n-1} + \vec{v}_{n-1}\,\Delta t + \frac{1}{2}\,\vec{a}_{n-1}\,\Delta t^2,$$
$$\vec{v}_n = \vec{v}_{n-1} + \vec{a}_{n-1}\,\Delta t.$$

We thereby obtain a complete numerical solution to the equation of motion.

In our ray tracing calculations, the first five terms in each series of (B-2) and (B-3) were taken. Some sample results are shown here. Fig. B.1 shows the trajectory of a 14.4 MeV $^8Li^{+3}$ ion. All $^8Li^{+3}$ emitted at $\theta = 7.5°$ with this energy are focused to a point 209.5 cm from the point object source. The solenoid's focusing current has been assumed to be 113 Amps. Fig. B.2 shows the solenoid's momentum dispersion. Particles are $^8Li^{+3}$ of 14 MeV, 14.5 MeV and 15 MeV at $\theta = 7.5°$. In the configuration shown in this figure, the axial and vertical dispersions are $\Delta z/(\Delta p/p) = 2.71$ cm/% and $\Delta r/(\Delta p/p) = 0.12$ cm/%, respectively. Fig. B.3 shows the solenoid's spherical aberration for 14.4 MeV $^8Li^{+3}$ ions at 5° to 11°. The radius of the circle of least confusion is $r_{clc} = 0.85$ cm. Fig. B.4 shows that the primary elastically scattered $^7Li^{+3}$ beam is separated from the secondary 14.4 MeV $^8Li^{+3}$ beam.

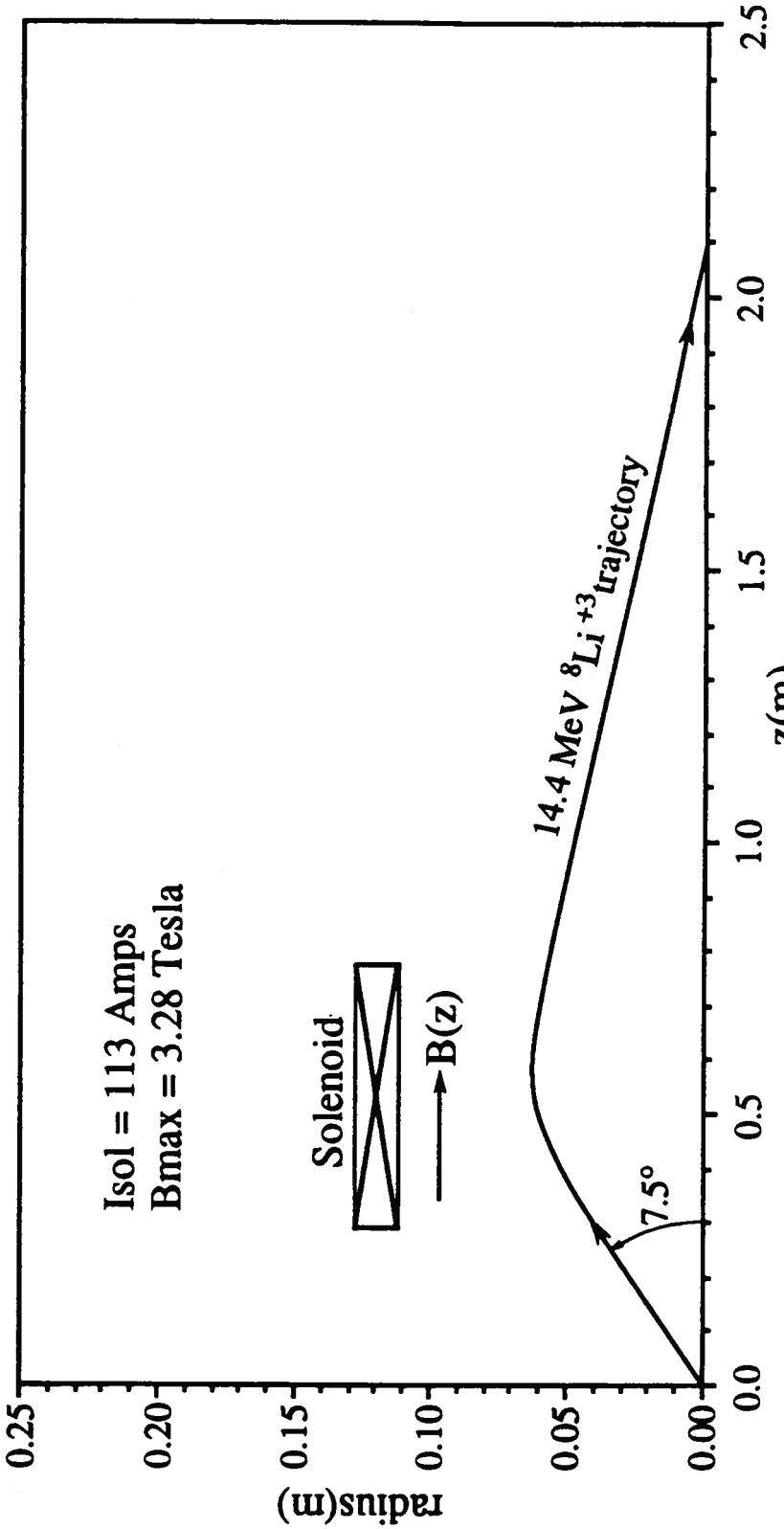

Fig. B.1 Trajectory of 14.4 MeV $^{8}Li^{+3}$ ions emitted at $\theta = 7.5°$.

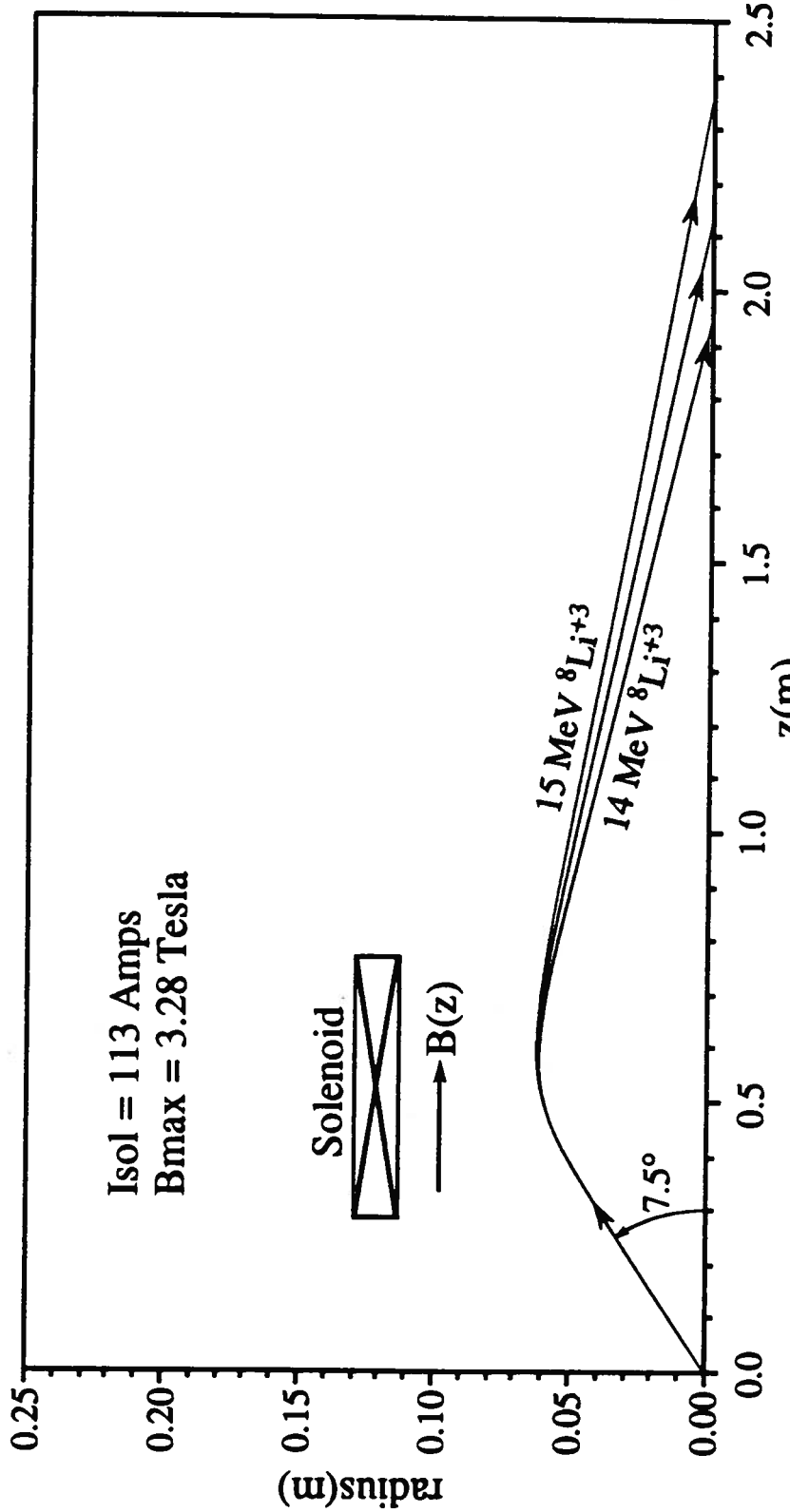

Fig. B.2 Momentum dispersion of the solenoid for $^8Li^{+3}$ emitted at $\theta = 7.5°$ with energies 14 MeV, 14.5 MeV and 15 MeV.

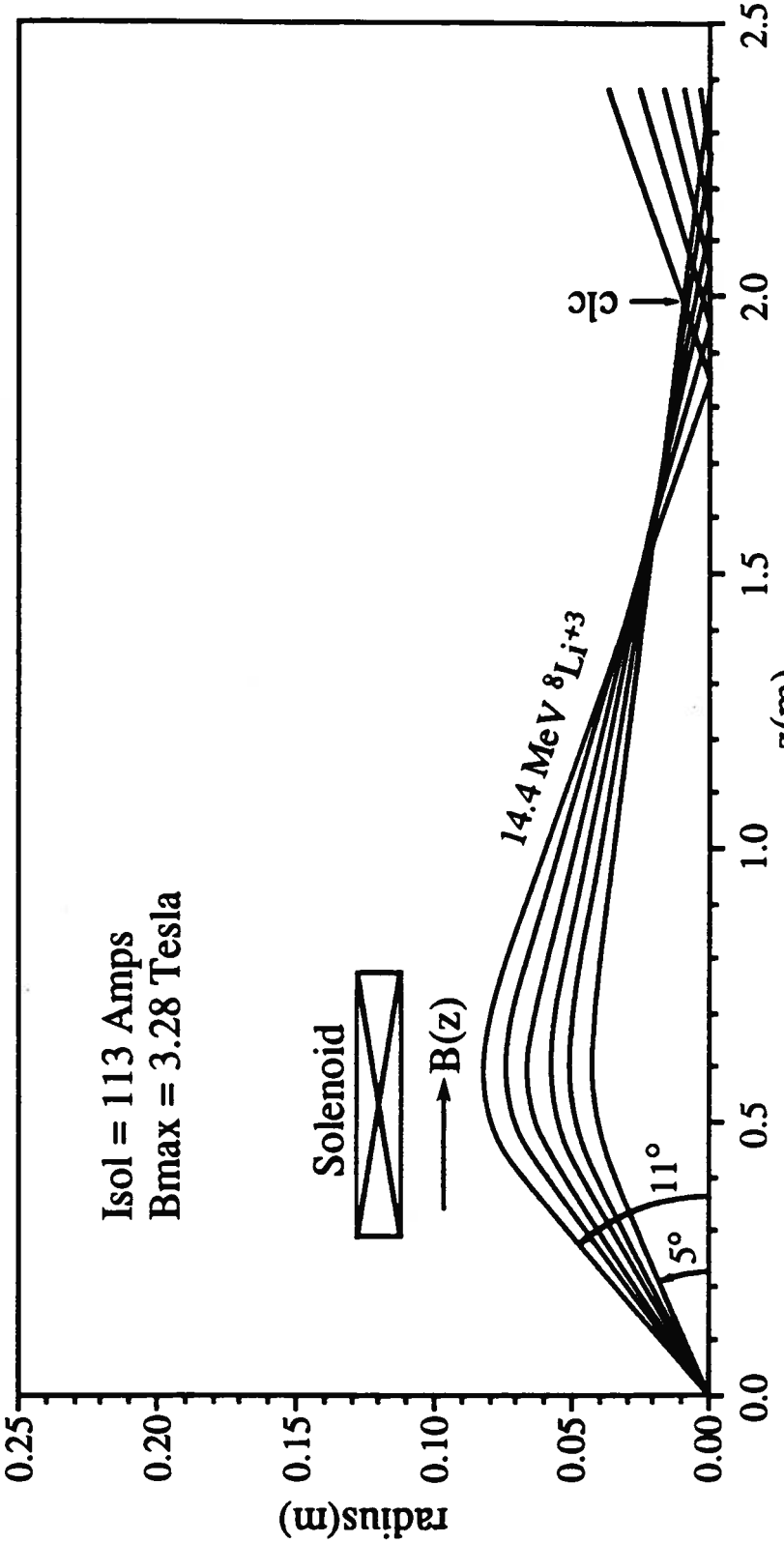

Fig. B.3 Spherical aberration of the solenoid for $^8Li^{+3}$ emitted at 5° to 11°.

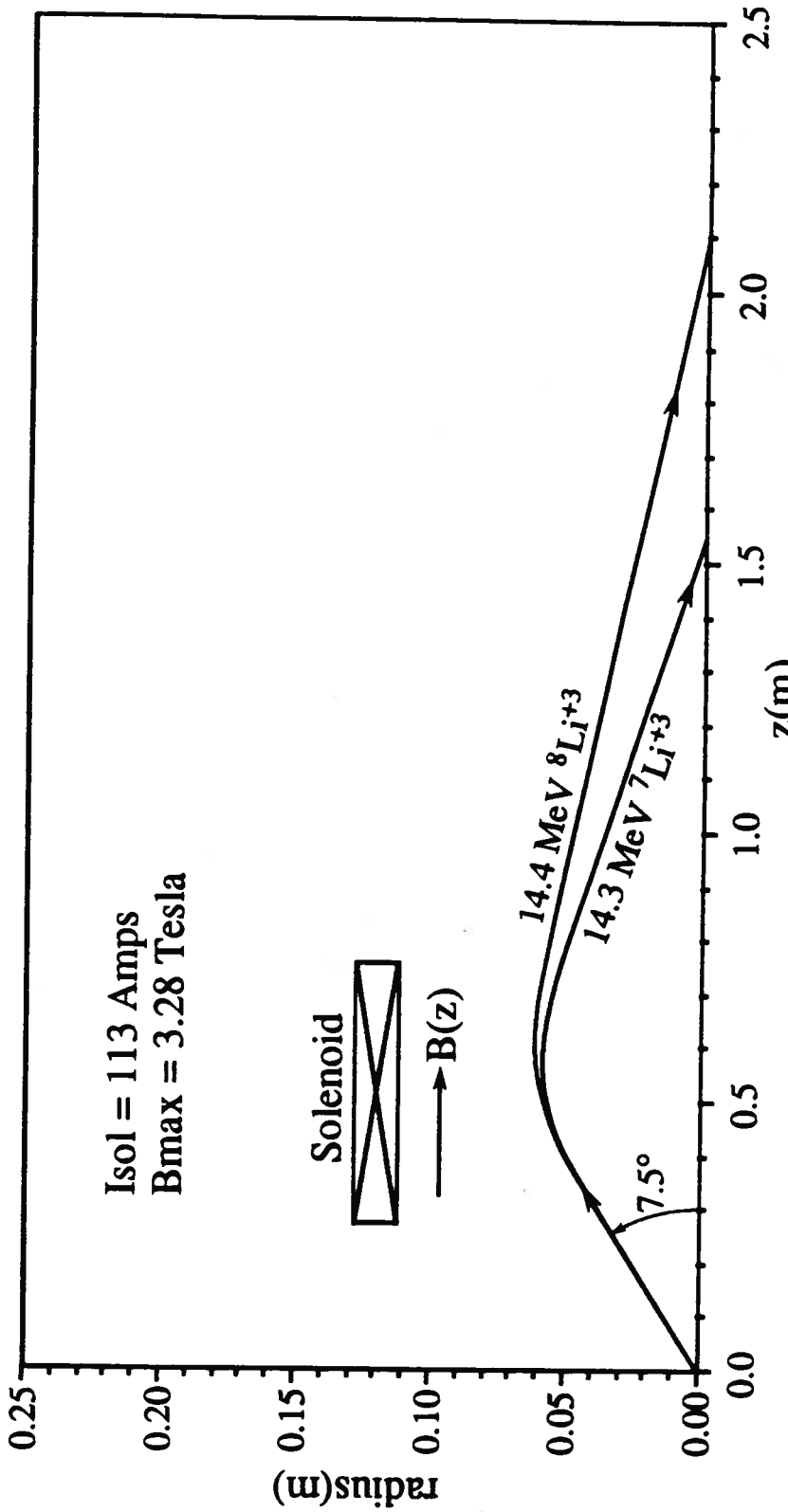

Fig. B.4 Separation of 14.4 MeV $^{8}Li^{+3}$ from 14.3 MeV $^{7}Li^{+3}$.

APPENDIX C

PREPARATION OF THIN TARGET FOILS

Our studies of radioactive-ion-induced nuclear reactions required the use of special deutrium and ^{13}C targets. For this purpose we have made thin foils of deuterated polyethylene, polyethylene-^{13}C and titanium deuteride.

Various methods for preparing $(CD_2)_n$ foils have been described in the literature (Arnison, 1966; Olivo, 1967; Bartle, 1973; Bartle, 1977). In these methods, solid backing to support the foils or a releasing agent for stripping off the foils is needed. Thus the composition of the foils is not simple. The recipe we used allows us to make self-supporting $(CD_2)_n$ foils without any coating or releasing materials. The following describes how we prepared the foils.

A heater (Corning PC-351 Hot Plate-Stirrer) was placed on an adjustable table. A plate of glass was put on the top of the heater. The plate is a piece of optical glass (10 cm diameter and 2 cm thick) of round shape and its end surfaces are parallel and smooth. The table was then adjusted until the surface of the plate was very level. An aluminum ring-shape confiner was seated on the top of the plate to hold the $(CD_2)_n$ solution. The aluminum confiner has a polished bottom surface to ensure close contact with the glass plate . The heater current was then raised until the temperature of the glass reached 140°C (heater dial = 2.5).

A known amount of deuterated polyethylene powder[1] was put into a beaker that contained about 20 ml of xylene. The ring confiner has a diameter of 6.3 cm and hence defines an area of 31.2 cm^2. To make a 1 mg/cm^2 $(CD_2)_n$ foil, for example, 31.2 mg of $(CD_2)_n$ powder is needed, assuming no waste during transfer.

The beaker was then covered and heated to the boiling point of xylene ($\sim$ 145°C). The boiling was kept on for a few minutes for the powder to be completely dissolved. After this, the beaker was removed from the heat source and gently shook to get rid of the bubbles. Once all bubbles disappeared, the solution was poured onto the glass plate which had been kept at constant temperature 140°C. The solution then diffused over the surface of the plate within the ring and formed a uniform plastic-like layer. At this point the heater was turned off and the setup allowed to cool down. The xylene solution evaporated and the layer became thinner. About one hour and a half after turning off the heater, the plate was still warm and a smoothly polymerized foil appeared. The confining ring was removed at this point and the foil was carefully stripped off the plate. The foil was then weighed to measure the surface density (mg/cm^2).

Polyethylene-^{13}C foils were made in the same way except that $(^{13}CH_2)_n$ powder[2] was used instead of $(CD_2)_n$ powder.

In this process of making foils, it is important to keep the temperature of the plate at $\sim$140°C, i.e., slightly below the boiling point of the xylene solution. If the temperature is too high, the solution blisters and the foil is formed with bubbles. Conversely, if the temperature is too low, the solution cannot diffuse to cover the plate homogeneously. It is also important to release the foil before the setup is cooled down to room temperature since it is much easier to strip the foil off the plate surface while it is still warm. It should also be noted that no releasing agent needs to be coated onto the glass plate in our recipe.

Titanium deuteride targets were made by heating titanium foils in the atmosphere of deuterium gas. The foils we used have the dimensions of 5cm $\times$ 5cm $\times$ 5μm. Each foil contains 1.78 $\times$ 10^{20} Ti atoms, which can combine with 2 $\times$ 1.78 $\times$ 10^{20} deuterium atoms since each Ti atom can take on two deuterium atoms. This

ratio means a minimum pressure of 0.1 torr of deuterium gas if the vacuum chamber has a volume of 5×10^4 cm^3.

To make a TiD_2 foil, the titanium foil was first weighed and then mounted between two special electrodes. The vacuum chamber was pumped down to good vacuum (1×10^{-5} torr) and then filled with deuterium gas up to a pressure of 5 torr. The foil was heated to about 900°C (it appeared red at this temperature) for 20 minutes. After this the chamber was opened to air and the exposed foil dismounted and weighed again to calculate the amount of deuterium put on the original foil. The chamber was over pressurized to suppress the ratio of the residual air to the deuterium gas and to minimize the effect of possible air leaks by shortening the exposure time.

The uniformity of the foils were checked by measuring the energy losses of α-particles in the foils. A Th^{228} α-source was collimated with a small tube 2 cm long and 2 mm diameter, and was directed to a solid state detector connected to proper electronics circuits. An α-energy spectrum of the source was then recorded. After that, the foil to be measured was positioned between the source and the detector, with the point of interest lined up with the axis of the collimation tube. Another α-energy spectrum was taken. All peaks of the spectrum shifted to lower energies. The α-energy loss and hence the thickness at this point was determined by comparing these two spectra. The process was repeated for as many points as necessary to reasonably represent the foil. If all energy losses at different points are the same the foil is uniform. Otherwise it is nonuniform.

As determined by the method described above, the nonuniformities of thicknesses of good $(CD_2)n$ and $(^{13}CH_2)n$ are typically 10%. These can be reduced if the glass plate can be mounted more horizontally. The TiD_2 foils are only 1% nonuniform. The ratio of deuterium to titanium atoms, as derived from the energy losses

in Ti and TiD_2 foils, is 1.99, indicating each titanium atom has combined with, as expected, approximately two deuterium atoms.

Footnotes to Appendix C

[1]3858 Benner Road, Miamisburg, Ohio 45342

[2]Icon Services, Inc., 19 Ox Bow Lane, Summil, New Jersey 07901

APPENDIX D

PRODUCTION SPECTRA OF THE ^{7}Li + ^{9}Be REACTION

When a 20 MeV ^{7}Li beam bombards a 4 μm ^{9}Be target, ^{4}He, ^{6}He, ^{6}Li, ^{8}Li and other types of particles are produced. Fig. D.1 shows a spectrum of all products from this ^{7}Li + ^{9}Be reaction, collected through a small aperture ($\Delta\Omega$ = 2.73 $\times$ 10^{-4} radians) at $\theta_{lab} = 15°$. Energy spectra, generated by gating the corresponding product groups in Fig. D.1, are shown in Figs. D.2 through D.6. Major peaks of the spectra are marked with their event counts, which give the relative intensities of the peaks. ^{6}He ($T_{\frac{1}{2}}$ = 807 ms) and ^{8}Li ($T_{\frac{1}{2}}$ = 836 ms) are both short-lived and can be collected and focused by the magnetic solenoid to form radioactive ion beams. Usually the ^{4}He particles degrade the purities of the radioactive beams, since they are produced over a large energy range (Fig. D.2) and some of them can have the same magnetic rigidities as those of the radioactive ions.

An angular distribution at KE(^{7}Li) = 20 MeV for ^{9}Be(^{7}Li,^{8}Li)^{8}Be is shown in Fig. D.7. The smooth curve in the figure is a result of Born approximation (FRDWBA) using the optical model parameters for ^{10}Be(^{7}Li,^{8}Li)^{9}Be (see Table 5.1). The data points are measured differential cross sections and have been used to normalize the curve, which then serves to roughly extrapolate differential cross sections beyond the data points. Cross sections for other peaks in Figs. D.2 through D.6 can be estimated through their intensities relative to ^{8}Li, at the same laboratory angle.

For production of ^{6}He and ^{8}Li beams, the energy spectra (Fig. D.2 - D.6) can be used to calculate the proper solenoid focusing currents and predict the corresponding beam purities. The angular distribution can then be used to estimate the secondary

beam intensities.

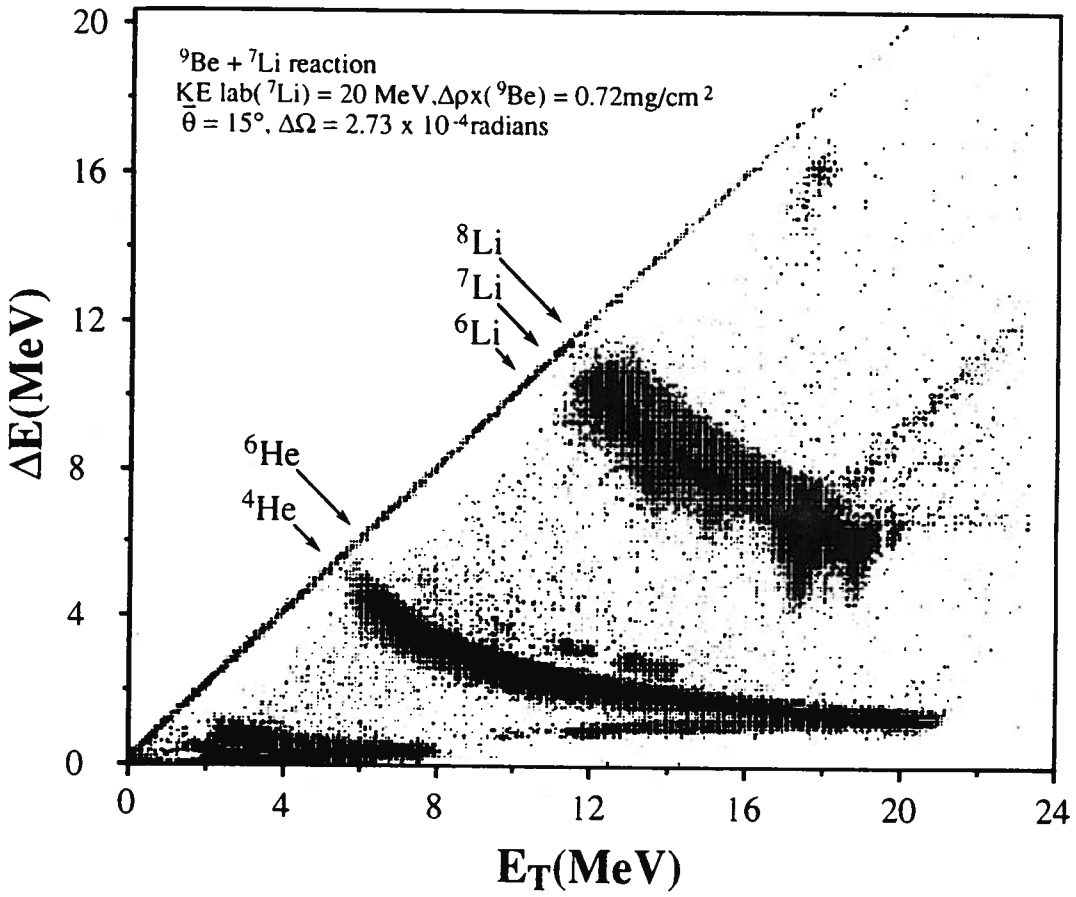

Fig. D.1 $\Delta E - E_T$ spectrum of products from ^{7}Li + ^{9}Be reaction at $\bar{\theta}_{lab} = 15°$. The thickness of the ^{9}Be target is 4 μm and the energy of the ^{7}Li beam is 20 MeV.

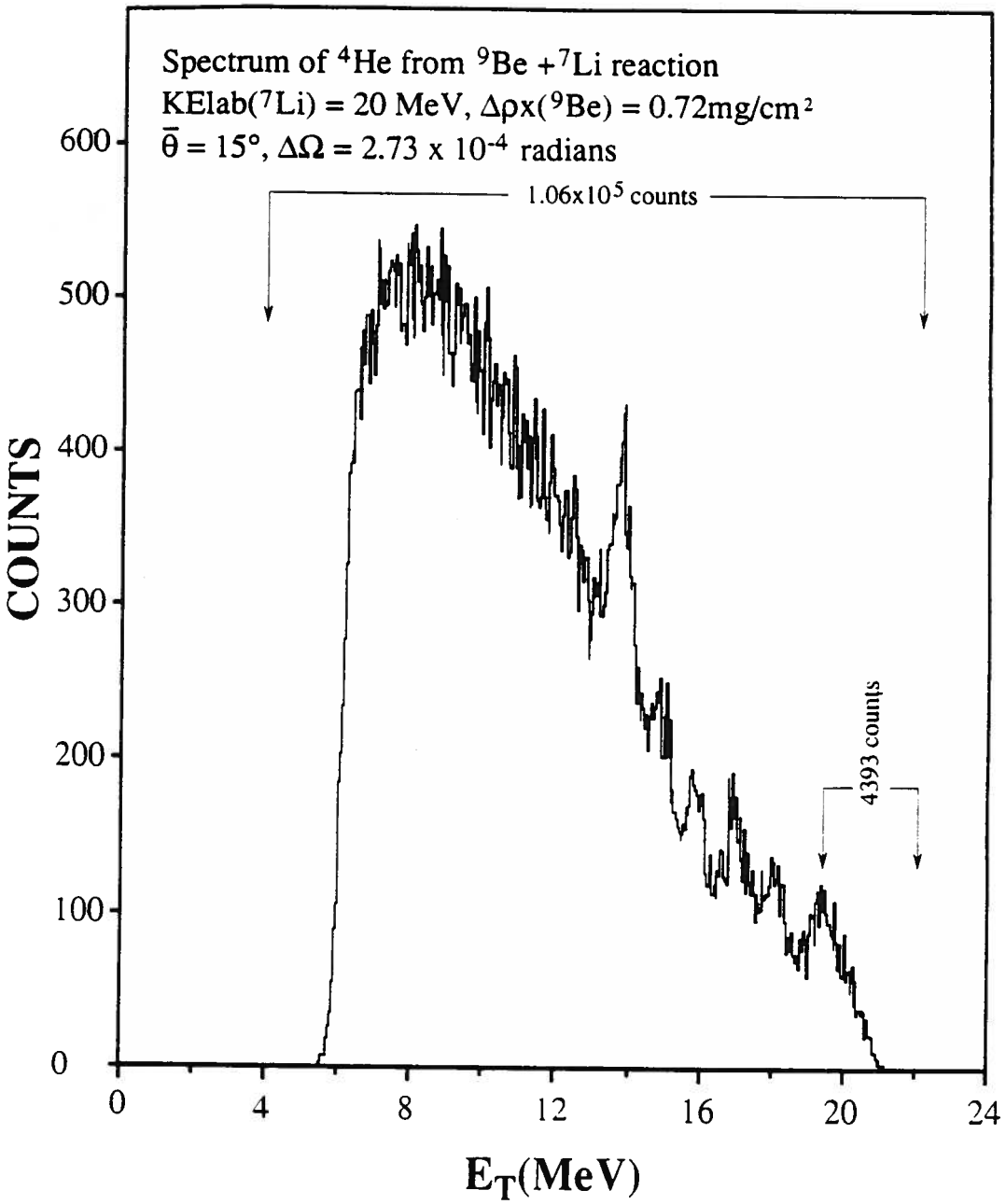

Fig. D.2 E_T spectrum of ^{4}He from ^{7}Li + ^{9}Be reaction at $\bar{\theta}_{lab} = 15°$. The thickness of the ^{9}Be target is 4 μm and the energy of the ^{7}Li beam is 20 MeV.

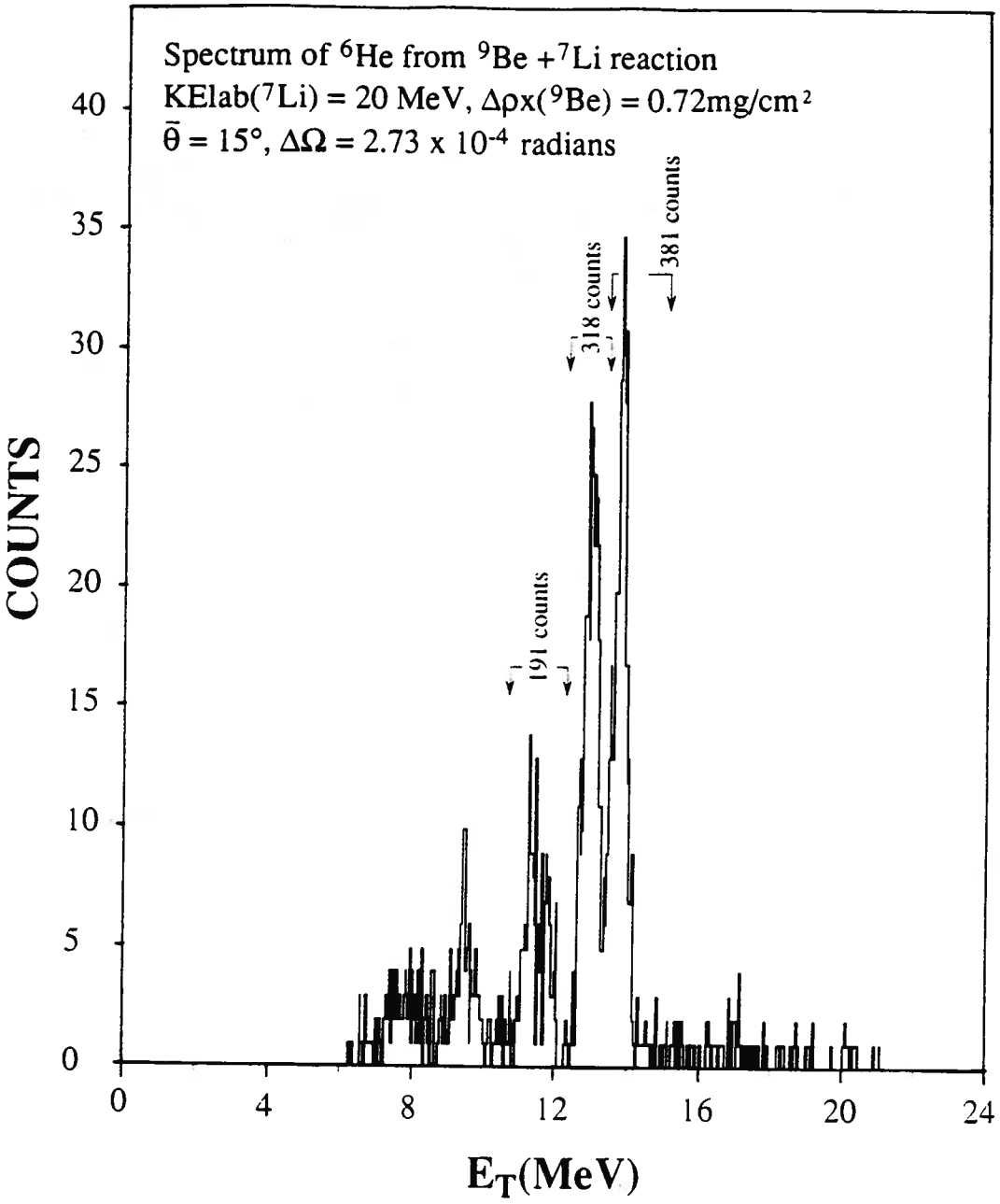

Fig. D.3 E_T spectrum of ^{6}He from ^{7}Li + ^{9}Be reaction at $\bar{\theta}_{lab} = 15°$. The thickness of the ^{9}Be target is 4 μm and the energy of the ^{7}Li beam is 20 MeV.

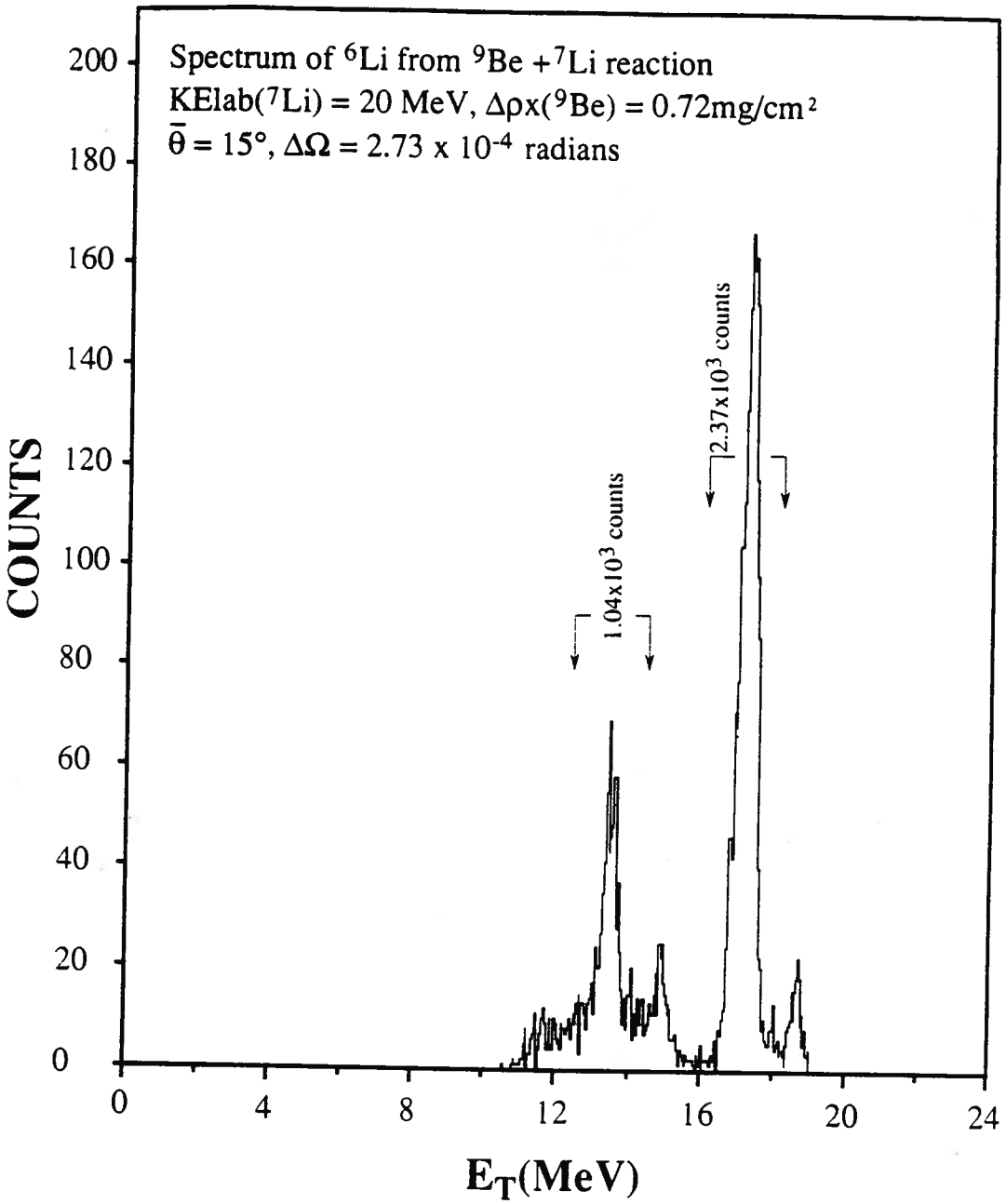

Fig. D.4 E_T spectrum of ^{6}Li from ^{7}Li + ^{9}Be reaction at $\bar{\theta}_{lab} = 15°$. The thickness of the ^{9}Be target is 4 μm and the energy of the ^{7}Li beam is 20 MeV.

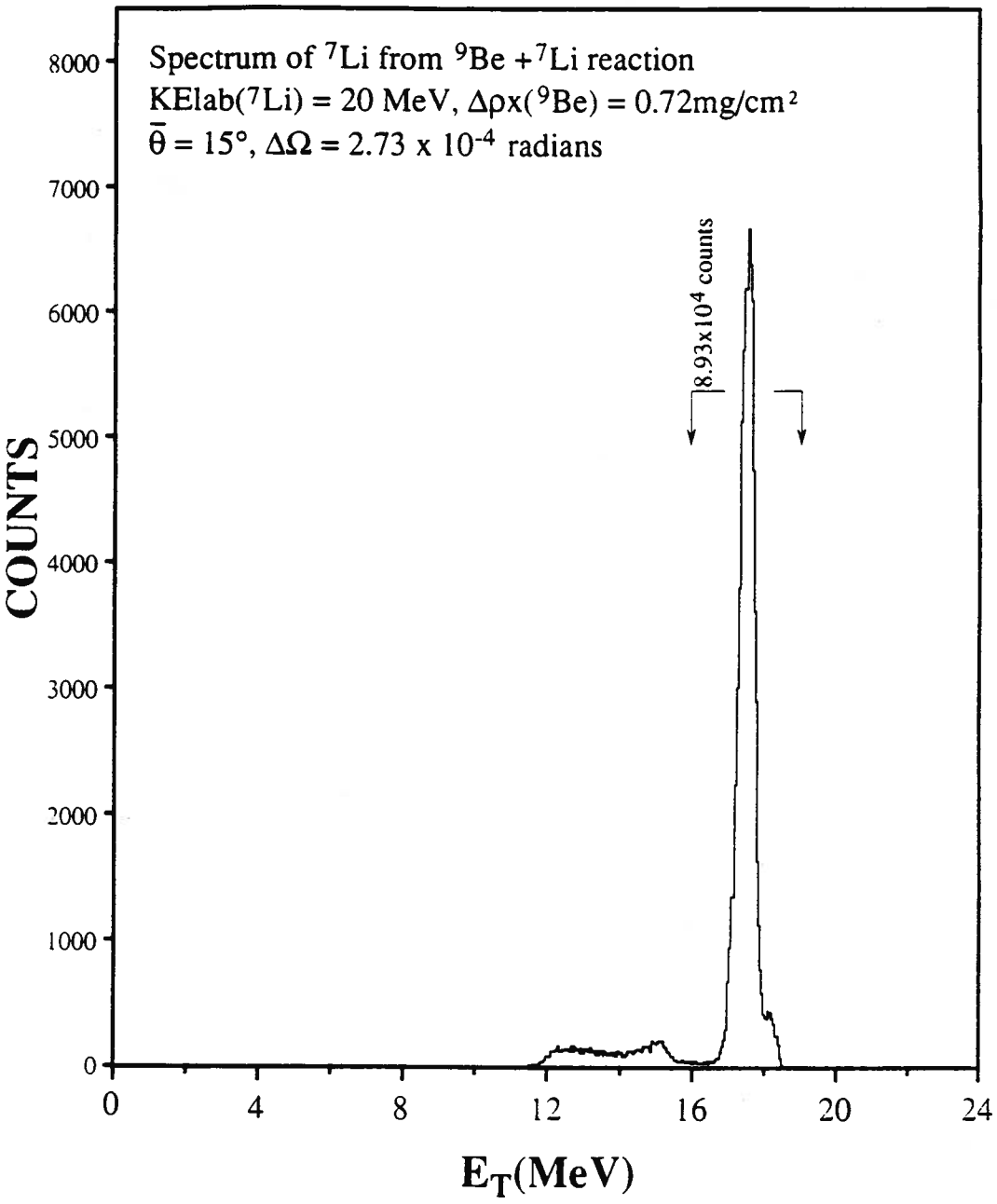

Fig. D.5 E_T spectrum of ^{7}Li from ^{7}Li + ^{9}Be reaction at $\bar{\theta}_{lab} = 15°$. The thickness of the ^{9}Be target is 4 μm and the energy of the ^{7}Li beam is 20 MeV.

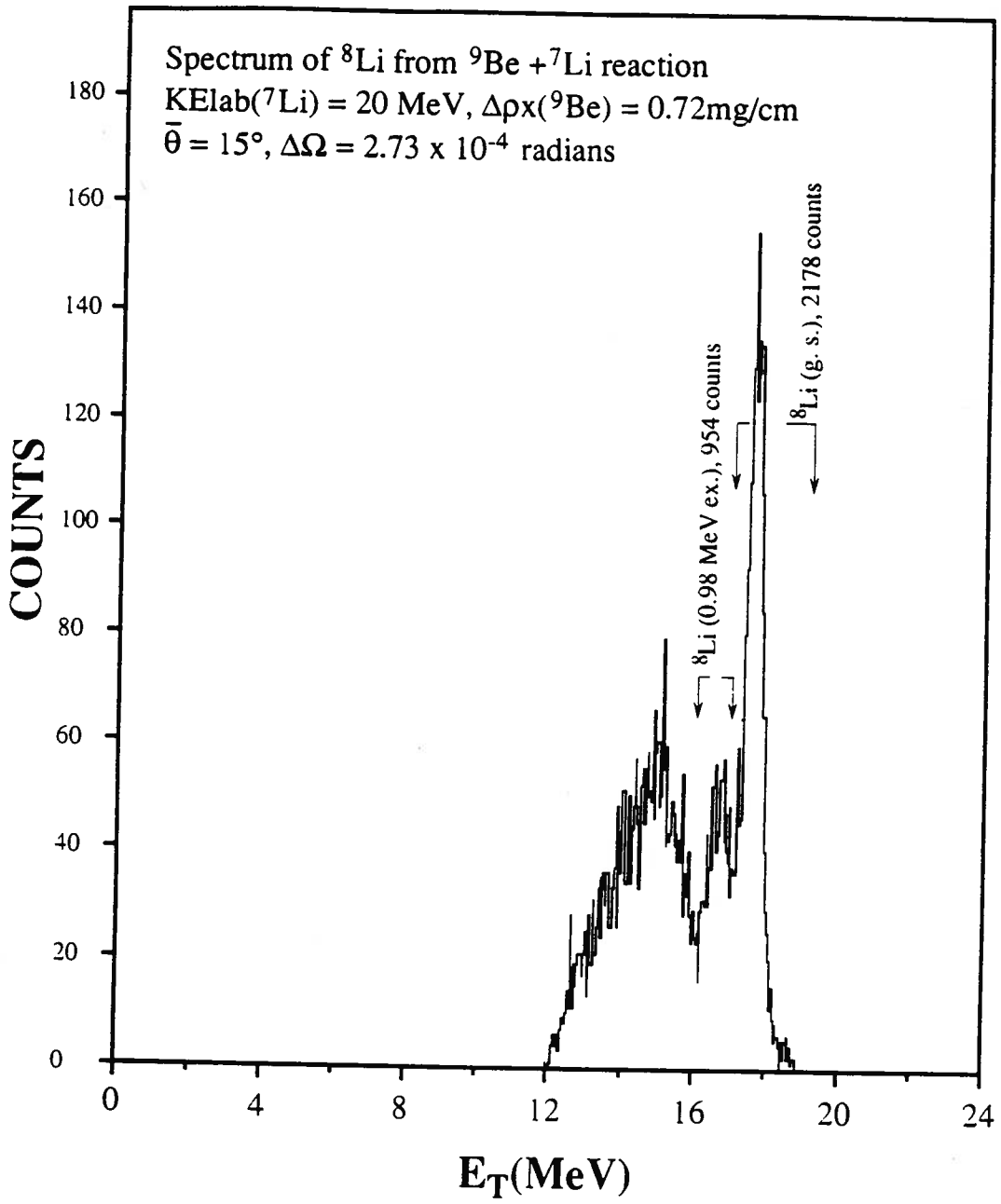

Fig. D.6 E_T spectrum of ^{8}Li from ^{7}Li + ^{9}Be reaction at $\bar{\theta}_{lab} = 15°$. The thickness of the ^{9}Be target is 4 μm and the energy of the ^{7}Li beam is 20 MeV.

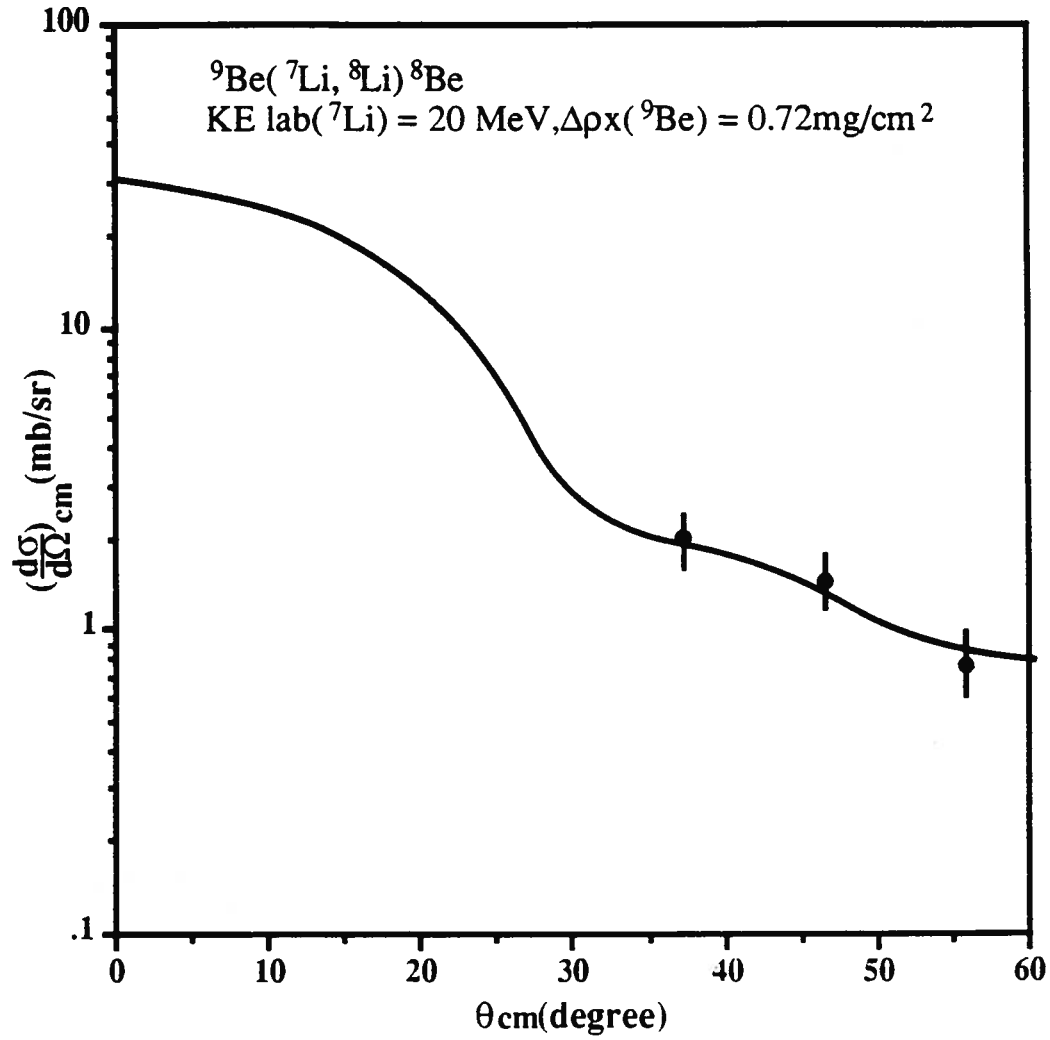

Fig. D.7 Angular distribution of differential cross sections for ^{9}Be(^{7}Li, ^{8}Li)^{8}Be. The energy of the ^{7}Li beam is 20 MeV.

BIBLIOGRAPHY

BIBLIOGRAPHY

Applegate, J.H. et al., Astrophys. J. **329** (1988) 572.

Applegate, J.H. and Hogan, C.J., Phys. Rev. **D31** (1985) 3037.

Arnison, G.T.J., Nucl. Instr. Methods **40** (1966) 359.

Arnould, M., *Proc. Int. Symposium on Heavy Ion Physics and Nuclear Astrophysical Problems*, ed. S. Kubona, M. Ishihara, and T. Nomura (World Scientific, Singapore, 1988a) p. 287.

Arnould, M. et al., the "Radioactive Ion Beam" Project at Louvain-La-Neuve, ed. Th. Delbar, M. Huyse, and J. Vanhorenbeeck, RIB-1988-01 (Belgium, 1988b).

Austin, S.M., *Proc. Fifth Int. Conf. on Clustering Aspects in Nuclear and Subnuclear Systems*, ed. K. Ikeda, K. Katori, and Y. Suzuki (Physical Society of Japan, Japan, 1989) p. 185.

Bartle, C.M. and Meyer, H.O., Nucl. Instr. Methods **112** (1973) 615.

Bartle, C.M., Nucl. Instr. Methods **144** (1977) 599.

Becchetti, F.D. et al., *Proc. Int. Symposium on Heavy Ion Physics and Nuclear Astrophysical Problems*, ed. S. Kubona, M. Ishihara, and T. Nomura (World Scientific, Singapore, 1988) p. 277.

Becchetti, F.D. et al., Phys. Rev. **C40** (1989) R1104.

Bimbot, R. et al., Z. Phys. A – Atoms and Nuclei **322** (1985) 443.

Boyd, R.N. et al., *Proc. Int. Symposium on Heavy Ion Physics and Nuclear Astrophysical Problems*, ed. S. Kubona, M. Ishihara, and T. Nomura (World Scientific, Singapore, 1988) p. 39.

Buchmann, L., Nucl. Instr. Methods. Phys. Res., **B26** (1987) 151.

Burbridge, E.M. et al., Rev. Mod. Phys. **29** (1957) 547.

Burcham, W.E., Elements of Nuclear Physics, (Longman, New York, 1979).

Chatterjee, A., *Proc. Workshop on Prospects for Research with Radioactive Beams from Heavy Ion Accelerator*, ed. M. J. Nitschke, LBL-18187 (Washington, DC., 1984) p. 179.

Cohen, S. and Kurath, D., Nucl. Phys. **A101** (1967) 1.

Cosslett, V.E., Introduction to Electron Optics, (Clarendon Press, Oxford, 1950).

Enge, H.A., Introduction to Nuclear Physics (Addison-Wesley Publishing Company, Inc., Reading, Massachusetts, 1966).

Fowler, W.A., Rev. Mod. Phys. **56** (1984) 149.

Fowler, W.A., *Proc. Accelerated Radioactive Beams Workshop*, ed. L. Buchmann and J.M. D'Auria, TRI-85-1 (TRIUMF, 1985) p.1.

Goldstein, H., Classical Mechanics (Addison-Wesley Publishing Company, Reading, Massachusetts, 1980).

Gould, H. et al., An Introduction to Computer Simulation Methods, Part 1 (Addison-Wesley Publishing Company, Reading, Massachusetts, 1988).

Hagberg, E., *Proc. Accelerated Radioactive Beams Workshop*, ed. L. Buchmann and J.M. D'Auria, TRI-85-1 (TRIUMF, 1985) p. 323.

Haight, R.C. et al., Nucl. Instr. Methods **212** (1983) 245.

Hawks, P.W., Magnetic Electron Lenses (Spring-Verlag, New York, 1982).

Hodgson, P.E., Nuclear Reactions and Nuclear Structure, (Clarendon Press, Oxford, 1971).

Jackson, J.D., Classical Electrodynamics, (John Wiley & Son, New York, 1975).

Jiye, X., Aberration Theory in Electron and Ion Optics (Academic Press, Inc., New York, 1986).

Kemper, K.W. et al., Phys. Rev. **C15** (1977) 1726.

Kolata, J.J. et al., Nucl. Instr. Methods. Phys. Res. **B40/41** (1989a) 503.

Kolata, J.J. et al., (private communication, 1989b).

Kuhn, W, "LISA: A General Purpose Data Analysis Program," unpublished (Argonne National Laboratory Physics Division, 1982).

Kunz, P.D., Program DWUCK5, unpublished (University of Colorado, 1983).

Liu, W.Z. et al., Rev. Sci. Instr. **58** (1987) 220.

Liu, W.Z. and Becchetti, F.D., Rev. Sci. Instr. **60** (1989) 1228.

Malaney, R.A. and Fowler, W.A., Origin and Distribution of Elements, ed. G.J. Mathews (World Scientific, Singapore, 1987).

Marion, J.B. and Young, F.C., Nuclear Reaction Analysis Graphs and Tables, (American Elsevier Publishing Company, Inc., New York, 1968).

McClenahan, C.R. et al., Phys. Rev. **C11** (1975) 370.

Merill, J.R., Using Computers in Physics, (University Press of American, New York, 1976).

Norbeck, E. et al., Phys. Rev. **116** (1959) 1560.

Parker, P., *Proc. Fifth Int. Conf. on Clustering Aspects in Nuclear and Subnuclear Systems*, Kyoto, 1988, ed. K. Ikeda, K. Katori, and Y. Suzuki, (Physical Society of Japan, Japan, 1989) p. 185.

Rolfs, C.E. and Rodney, W.S., Caludrons in the Cosmos, (The University of Chicago Press, Chicago, 1988).

Sawicki, J.A., *Proc. Accelerated Radioactive Beams Workshop*, ed. L. Buchmann and J.M. D'Auria, TRI-85-1 (TRIUMF, 1985) p. 307.

Segre, E., Nuclei and Particles, (W.A. Benjamin, Inc., Massachusetts, 1977).

Schiffer, J.P. et al., Phys. Rev. **164** (1967) 1274.

Schramm, D.N. and Wagoner, R.V., Ann. Rev. Nucl. Part. Sci. **27** (1977) 37.

Schumacher, P. et al., Nucl. Phys. **A212** (1973) 573.

Spite, F. and Spite, M., Astron. Astrophys. **115** (1982) 357.

Stern, R.L., Ph.D. thesis (University of Michigan, 1987).

Tanihata, I., Nucl. Phys. **A478** (1988) 795c.

Truran, J.W., *Fifth Int. Conf. on Nuclei Far From Stability*, Ontario, 1987, ed. I.S. Towner (American Institute of Physics, New York, 1988) p. 543.

Vineyard, M.F. et al., Phys. Rev. **C30** (1984) 916.

Wagoner, R.V. et al., Astrophys. J. **148** (1967) 3.

Wallace, R.K. and Wooseley, S.E., Astrophys. J. Supple. Ser. **45** (1981) 389.

Witten, E., Phys. Rev. **D30** (1984) 272.